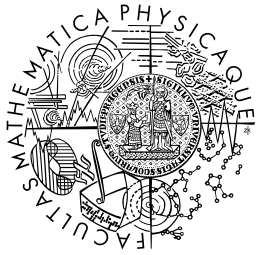

FACULTY
OF MATHEMATICS
AND PHYSICS
Charles University

MASTER THESIS

Bc. Andrej Kancko

The search for new spin-liquid materials - synthesis of kagome and pyrochlore fluoride magnets

Department of Condensed Matter Physics

Supervisor of the master thesis: Dr. Ross Harvey Colman

Study programme: Physics

Study branch: Physics of Condensed Matter and Materials

Prague 2022

I declare that I carried out this master thesis independently, and only with the cited sources, literature and other professional sources. It has not been used to obtain another or the same degree.

I understand that my work relates to the rights and obligations under the Act No. 121/2000 Sb., the Copyright Act, as amended, in particular the fact that the Charles University has the right to conclude a license agreement on the use of this work as a school work pursuant to Section 60 subsection 1 of the Copyright Act.

In ..... date ....

Author's signature

I would like to express my deepest gratitude to every person that helped me and supported me throughout my Master's studies, making this research and thesis possible.

First and foremost, my biggest thanks go to my supervisor, Dr. Ross Harvey Colman, for his tremendeous dedication of time and effort into his supervision, patient guidance with sample preparation and measurements, insightful discussions, English corrections and ideas for improvements of the thesis.

I would like to thank our collaborator, Gerald Giester, Ao. Univ.-Prof. Mag. Dr., from the Department of Mineralogy and Crystallography at the University of Vienna, for performing single crystal X-ray diffraction measurements on $NaCdCo_2F_7$.

Special acknowledgements go to my dear colleagues, Mgr. Kristina Vlášková, Mgr. Jíří Volný and RNDr. Petr Doležal, Ph.D., for their help, support as well as for creating such a friendly and entertaining work environment.

Most importantly, nothing would have been possible without my family and friends, and their endless love, care and support throughout my academic life as well as my personal life.

Experiments were performed in MGML (www.mgml.eu), which is supported within the program of Czech Research Infrastructures (project no. LM2018096).

Title: The search for new spin-liquid materials - synthesis of kagome and pyrochlore fluoride magnets

Author: Bc. Andrej Kancko

Department: Department of Condensed Matter Physics

Supervisor: Dr. Ross Harvey Colman, Department of Condensed Matter Physics

Abstract: This thesis focuses on the synthesis and characterization of a new $AA'B_2F_7$-type pyrochlore fluoride family, $NaCdB_2F_7$ (B = Mn, Fe, Co, Ni, Cu, Zn) predicted by a calculated pyrochlore structural tolerance factor, as well as the synthesis of new kagome fluorides $Na_3CdCo_3AlF_{14}$, $Rb_2SnCo_3F_{12}$ and $Cs_2ZrCo_3F_{12}$, aiming to expand the knowledge about the frustrated pyrochlore and kagome antiferromagnets. The synthesis techniques included solid-state reactions, laser floating zone melting and melt crystallization. All pyrochlore fluorides were successfully synthesized, although only B = Zn, Co, Mn and Ni as phase-pure single crystals. PXRD refinements confirmed the $Fd\bar{3}m$ structure in all synthesized pyrochlores, while SCXRD showed full Na/Cd disorder on the A-site and no A/B intersite mixing in the Co pyrochlore. Magnetization measurements revealed dominant antiferromagnetic interactions evidenced by large negative Curie-Weiss temperatures (from -38 K in Mn to -108 K in Co), with a spin-freezing transition below 4 K in B = Co, Mn and Ni, evidenced by further AC susceptibility and heat capacity measurements in Co and Mn. Cu showed no spin freezing down to the lowest-measured temperature, 1.8 K, implying a very large magnetic frustration. Fe has not been measured due to the large impurity content. The attempted synthesis of the aforementioned kagome fluorides was unsuccessful, therefore no further measurements could be performed.

Keywords: quantum spin liquid, frustrated magnetism, pyrochlore, kagome, antiferromagnet

Contents

Introduction

In many magnetic materials, it is common to see a magnetic ordering transition upon cooling that results in a static arrangement of the localized ionic magnetic moments (or spins), typically in a collinear fashion – parallel with their neighbours in a ferromagnetic material, and anti-parallel in antiferromagnets. This ordering transition typically occurs at a temperature commensurate with the energy scale of the interactions between the magnetic ions.

Frustrated magnets, conversely, are materials where simple collinear arrangements of spins cannot arise due to a competition between a large number of possible arrangements, either owing to the geometrical constraints given by the crystal lattice, or due to the presence of multiple competing types of magnetic interactions, extending to further-neighbour exchange between the magnetic ions. [1] As a result, the spins fluctuate between the possible ground states in a highly-correlated manner and push the magnetic ordering to much lower temperatures than the interaction strength.

The spin fluctuations can be classical (dominant for large spins), which are driven by thermal energy, or quantum (S close to $\frac{1}{2}$), which are characterized by the quantum-mechanical zero-point motions owing to the Heisenberg uncertainty principle. If these fluctuations persist down to the temperature of absolute zero, preventing any ordering or freezing of the spins, this correlated but dynamic state of matter is known as *the quantum spin liquid* (QSL). It was first proposed by Anderson in 1973 [2] as the *resonating valence bond* (RVB) ground state of an antiferromagnet. In 1987, Anderson used the RVB theory in an attempt to explain the newly-discovered high-temperature superconductivity in La_2CuO_4 cuprates. It is theorized that QSLs are hosts to many exotic phenomena, such as exotic excitations with fractional quantum numbers and artificial gauge fields. [3] The list of candidate QSL materials has grown steadily within the last 10 years, and many candidates are focused on just a few geometrically frustrated lattice types – particularly the *pyrochlore* and *kagome lattices*.

Pyrochlore structure materials – one of the the focuses of this project – typically have the formula $A_2B_2X_7$, with A and B sites occupied by cations and X sites occupied by anions. Both A and B sites make up separate interconnected pyrochlore lattices, with each being a 3D network composed of cations residing on the vertices of corner-sharing tetrahedra. Oxide compounds (where $X = O$) make up most of the studied pyrochlore materials [4], and particularly in the rare-earth pyrochlores the observed exotic properties range from spin liquids [5], to spin ices [6, 7], to unconventional spin glasses [8]. However, due to the contracted nature of the rare-earth $4f$ orbitals, the low orbital overlap causes weak magnetic exchange interactions - requiring extremely low temperatures to probe the exotic emergent phenomena.

The transition metal fluorides, conversely, tend to have strong magnetic interactions mediated by super-exchange through fluoride ligands between the transition metal ions. Pyrochlore structure transition metal fluorides have been known for a long time, with some of the earliest works dating back to the 1960s [9]. Recently there has been a revival of research into this family of materials, with a particular focus on the $AA'B_2F_7$-type materials ($A = Na^+$; $A' = Ca^{2+}$, Sr^{2+}; $B =$

Mn^{2+}, Fe^{2+}, Co^{2+}, Ni^{2+}) [10, 11, 12, 13]. These materials show strong antiferromagnetic interactions evidenced by Curie-Weiss temperatures ranging from -73 K ($NaCaFe_2F_7$) to -140 K ($NaCaCo_2F_7$), but no magnetic order is seen down to temperatures as low as 4 K, where a spin-freezing transition is observed. Bifurcation of the zero-field-cooled (ZFC) and field-cooled (FC) data is seen, confirming the glassy nature of these materials. A study of the short range magnetic correlations in the $J_{\text{eff}} = 1/2$ Co^{2+}-based $NaA'Co_2F_7$ (A‘ = Sr, Ca) pyrochlores shows frozen XY-like magnetism at low temperature, but with magnetic correlations persisting up to 200 K [14]. A continuum of scattering with low energy pinch points was found in a recent investigation of the inelastic neutron excitation spectra of $NaCaNi_2F_7$, indicating a correlated spin-liquid character [15]. In our search for new quantum spin-liquid materials, we utilized a calculated pyrochlore structure tolerance factor [16] to predict a new stable family of compounds, $NaCdB_2F_7$ (B = Zn, Mn, Fe, Co, Ni and Cu), aiming to expand the current knowledge about frustrated pyrochlore fluorides.

The kagome lattice is known as one of the most geometrically frustrated systems due to its complex 2D network of vertex-sharing triangles. Recently, a number of kagome-lattice copper fluoride $A_2Cu_3M‘F_{12}$ (A = Rb, Cs; M‘ = Sn, Zr, Hf, Ti) materials have been investigated, aiming to destabilize magnetic order at low temperatures by means of the large quantum fluctuations of the low-spin ($S = 1/2$) Cu^{2+} ion. [17, 18, 19] Unfortunately, a symmetry-lowering transition as well as magnetic ordering was seen in these materials, leading to a quenching of the frustration. Using a similar assumption, we proposed a synthesis of two new kagome compounds, $Rb_2SnCo_3F_{12}$ and $Cs_2ZrCo_3F_{12}$ with the hope of pushing magnetic order down to very low temperatures with the low-spin $J_{\text{eff}} = 1/2$ Co^{2+} ion.

One can also isolate the 2D kagome planes from the 3D pyrochlore structure by means of an ordered dilution of the pyrochlore lattice with non-magnetic ions. This can be seen in the naturally occuring mineral Coulsellite, $Na_3CaMg_3AlF_{14}$ [20], which shows an ordered dilution of the $NaCaMg_2F_7$ pyrochlore lattice with Al^{3+} ions, producing a layered kagome structure that hosts the Mg^{2+} ions. However, there have not been any reports of this ordered dilution in any synthetic fluorides. As a result, we decided to synthesize a new Co^{2+}-based compound, $Na_3CdCo_3AlF_{14}$, as an ordered dilution of the $NaCdCo_2F_7$ pyrochlore fluoride.

Finding and investigating new model materials is an important task, as theoretical modelling and ground-state prediction of frustrated lattices is well known to lead to conflicting predictions dependent on the methods used. The exact properties of the $S = 1/2$ Heisenberg pyrochlore and kagome antiferromagnets are still hotly debated [21, 22, 23, 24], with very few ideal model materials. Further investigation of new pyrochlore and kagome fluorides (especially based on the low-spin $S = 1/2$ Cu^{2+}, $J_{\text{eff}} = 1/2$ Co^{2+} and $S = 1$ Ni^{2+} ions) may lead to either confirmation of one of the predicted ground-states, or potentially additional unexpected exotic properties.

1. Theoretical background

1.1 Introduction to magnetism

Magnetism, an intriguing physical phenomenon stemming from one of the four fundamental interactions - the electromagnetic force, has become a part of our daily lives. Magnets can be found in refrigerator doors, cellphones, data storage devices, high-speed trains (Maglevs) or magnetic resonance imagers (MRI). Ever since its discovery, it has attracted people's attention for more than a few thousands of years.

Ancient civilisations discovered that lodestone, a naturally magnetised iron ore with the chemical formula $Fe^{2+}Fe_2^{3+}O_4$ (also known as magnetite) attracted small pieces of iron. [25] Ancient Greeks termed it as "$\mu\alpha\gamma\nu\tilde{\eta}\tau\iota\zeta\ \lambda\iota\theta o\zeta$" (*magnētis lithos*, the Magnesian stone), giving rise to the name "magnet". [26]

This mysterious behaviour was quickly utilised in magnetic compasses (Han Dynasty, China, 2nd century BC - 1st century AD), in which the needle made of lodestone would align with the Earth's magnetic field, hence point towards its magnetic poles. This phenomenon was initially used for building houses and growing crops, but it was in the 11th century AD when it was first used for navigational purposes (Song Dynasty, China). For many years onwards, however, the fundamental nature of magnetism would still be a mystery.

This would change in the 19th century, when H. C. Ørsted (1819) discovered a reorientation of the compass needle near a wire with a passing current, hinting a relationship between electricity and magnetism. This observation would later be confirmed by experiments done by A.-M. Ampère, who noticed that the circulation of the magnetic field around a closed loop is proportional to the electric current passing through this loop (Ampère's circuital law, 1820). Further theoretical description was performed by J-B. Biot and F. Savart (Biot-Savart law, 1820), C.F. Gauss (Gauss's law, 1813) and M. Faraday (Faraday's law of induction, 1831). The unification of the laws for electricity and magnetism was done by J. C. Maxwell (Maxwell's equations, 1865). A. Einstein showed in his work on the special theory of relativity (1915) that Maxwell's equations hold true in all inertial reference frames. Finally, more fundamental theories would be developed in the 21st century where electromagnetism is involved, such as quantum electrodynamics, the electroweak theory and the standard model.

In the following chapters, we are going to look at the microscopic origin of magnetism and provide the theoretical minimum which is necessary to understand in the field of condensed matter physics.

1.2 Magnetic moment

1.2.1 The classical approach

The fundamental microscopic constituent of magnetism, the magnetic moment $\boldsymbol{\mu}$, can be thought of in the sense of classical electromagnetism as an oriented infinitesimal loop of current I enclosing an area $d\mathbf{S} = dS\mathbf{n}$ [27]:

$$d\boldsymbol{\mu} = I d\mathbf{S} \tag{1.1}$$

and is oriented along the unit vector $\mathbf{n}$ normal to the loop. The orientation of $\mathbf{n}$ is determined by the direction and charge of the current in the loop.

Given a finitely sized loop composed of infinitesimal current loops, the net magnetic moment is given by the sum of individual current loops. Only the current around the perimeter survives as the neighbouring current loops cancel out, giving

$$\boldsymbol{\mu} = \int d\boldsymbol{\mu} = I \int d\mathbf{S} = I\mathbf{S} \tag{1.2}$$

Interestingly, this object behaves as a magnetic dipole (in analogy to the electric dipole - a pair of closely separated opposite charges), even though no magnetic monopoles exist, in accordance with the Maxwell's equation $\nabla \cdot \mathbf{B} = 0$.

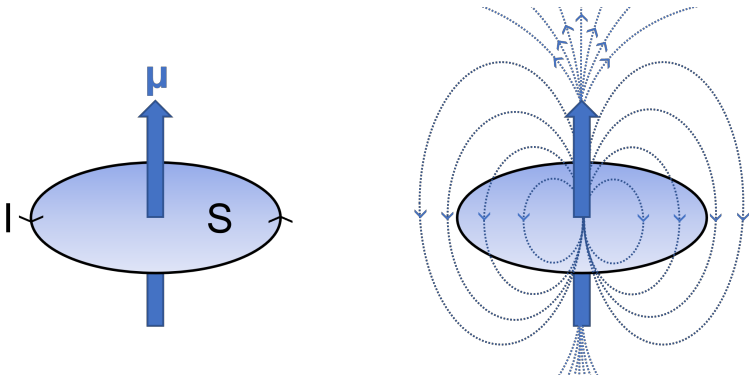

Figure 1.1: Magnetic dipole moment

From a classical standpoint, the magnetic dipole moment inside an atom is generated by the orbiting electrons of charge $-e$ and mass m_e, which produce current loops characterised by the angular momentum $\boldsymbol{L} = \boldsymbol{r} \times \boldsymbol{p}$, where $\boldsymbol{r}$ is the position vector and $\boldsymbol{p} = m_e\boldsymbol{v}$ is the momentum of the electron. There is a linear relationship between the magnetic moment and the angular momentum:

$$\boldsymbol{\mu} = \gamma \boldsymbol{L} \tag{1.3}$$

where γ is the gyromagnetic ratio of the electron.

Considering a hydrogen atom with one electron, we can estimate the size of the atomic magnetic moments: the electron orbiting at the speed v in a circular orbit of radius r (and area πr^2) produces a current $I = -e/T$, where T is the orbital period $T = 2\pi r/v$. Assuming Bohr's quantization of angular momentum $L = n\hbar$, where n is the energy level, the electron's angular momentum $L = m_e v r$ must be equal to $\hbar$ in the ground state ($n = 1$). Combining these ideas, we get

$$\mu = I\ \pi r^2 = -\frac{e\hbar}{2m_e} = -\mu_B \tag{1.4}$$

where we define the Bohr magneton $\mu_B = e\hbar/2m_e$ as a suitable unit of the atomic magnetic moment (SI: $\mu_B = 9.274 \times 10^{-24}$ Am^2). We also deduce that

$$\boldsymbol{\mu} = \frac{-e}{2m_e}\boldsymbol{L} \tag{1.5}$$

giving the gyromagnetic ratio of the electron $\gamma = -e/2m_e$. The magnetic moment is therefore antiparallel to the angular momentum vector due to the electron's negative charge.

When a magnetic moment is inserted into an external magnetic field $\boldsymbol{B}$, a torque $\boldsymbol{\tau}$ will tend to align the moment with the field [27]:

$$\boldsymbol{\tau} = \boldsymbol{\mu} \times \boldsymbol{B} \tag{1.6}$$

Since the orbiting electron has a mass and therefore an angular momentum $\boldsymbol{L}$, instead of a simple alignment with the field, the moment will start precessing around $\boldsymbol{B}$ with a characteristic frequency $\omega_L = \gamma B$ called the Larmor frequency.

The energy cost needed to rotate the moment away from the field to an angle θ is equal to $\Delta E = \int_0^\theta \tau d\theta' = \int_0^\theta \mu B \sin\theta' d\theta' = \mu B(1-\cos\theta)$. Ignoring the constant term, we define the potential energy U of a magnetic dipole in a magnetic field:

$$U = -\boldsymbol{\mu} \cdot \boldsymbol{B} = -\mu B \cos\theta \tag{1.7}$$

The potential energy of the magnetic dipole is minimal when the moment is parallel to the field ($\theta = 0°$ or $\cos\theta = 1$) and maximal when antiparallel to the field ($\theta = 180°$ or $\cos\theta = -1$).

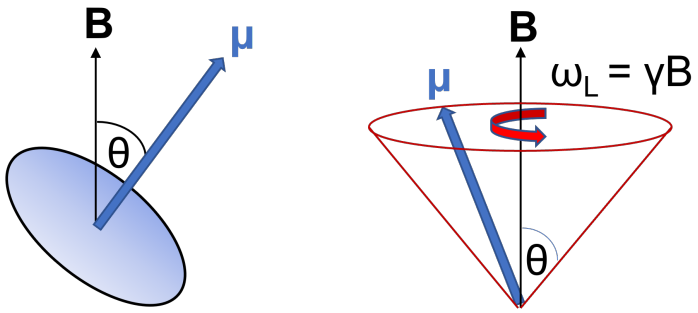

Figure 1.2: Precession of the magnetic moment in an external field.

1.2.2 The quantum-mechanical approach

In the previous section, we described the classical picture of the angular momentum arising from the orbital motion of an electron around the nucleus, giving rise to the magnetic moment.

In real atoms, however, the classical treatment is insufficient and quantum mechanics has to be utilised. There are two distinct types of angular momentum:

(a) **The orbital angular momentum $\hat{\boldsymbol{L}}$**, which originates from the orbital motion of the particle. It is a Hermitian vector operator $\hat{\boldsymbol{L}} = (\hat{L}_x, \hat{L}_y, \hat{L}_z)$ defined in the position representation as [28]

$$\hat{\boldsymbol{L}} = \hat{\boldsymbol{r}} \times \hat{\boldsymbol{p}} = -i\hbar(\hat{\boldsymbol{r}} \times \nabla) \tag{1.8}$$

where $\hat{\boldsymbol{r}} = (\hat{x}, \hat{y}, \hat{z})$ is the position operator and $\hat{\boldsymbol{p}} = -i\hbar\nabla$ is the momentum operator. We also define the square of $\hat{\boldsymbol{L}}$ as $\hat{\boldsymbol{L}}^{\boldsymbol{2}} \equiv \hat{L}_x^2 + \hat{L}_y^2 + \hat{L}_z^2$.

(b) **The spin angular momentum $\hat{\boldsymbol{S}}$**, which arises from the particle's characteristic intrinsic property - the spin s. It is a Hermitian vector operator $\hat{\boldsymbol{S}} = (\hat{S}_x, \hat{S}_y, \hat{S}_z)$ and is defined as

$$\hat{\boldsymbol{S}} = \frac{\hbar}{2}\hat{\boldsymbol{\sigma}} = \frac{\hbar}{2}(\hat{\sigma}_x, \hat{\sigma}_y, \hat{\sigma}_z) \tag{1.9}$$

where $\hat{\boldsymbol{\sigma}} = (\hat{\sigma}_x, \hat{\sigma}_y, \hat{\sigma}_z)$ is a vector of Pauli matrices, which for a spin-$\frac{1}{2}$ particle (such as the electron) take the form

$$\hat{\sigma}_x = \begin{pmatrix} 0 & 1 \\ 1 & 0 \end{pmatrix}, \quad \hat{\sigma}_y = \begin{pmatrix} 0 & -i \\ i & 0 \end{pmatrix}, \quad \hat{\sigma}_z = \begin{pmatrix} 1 & 0 \\ 0 & -1 \end{pmatrix} \tag{1.10}$$

We also define the square of $\hat{\boldsymbol{S}}$ as $\hat{\boldsymbol{S}}^{\boldsymbol{2}} \equiv \hat{S}_x^2 + \hat{S}_y^2 + \hat{S}_z^2$.

The main difference compared to classical mechanics is that the quantum-mechanical angular momenta are quantized - only certain discrete values are allowed, as opposed to the classical continuum of possible states. The possible values are expressed in terms of quantum numbers.

Quantum numbers, a set of conserved quantities for a particular dynamic quantum system, correspond to the eigenvalues of operators that commute with the Hamiltonian $\hat{\mathscr{H}}$ of the system. This follows from the time dependence of the expected operator value, which is (if the operator $\hat{A}$ itself is time independent) given by [27]

$$\frac{d}{dt}\langle\hat{A}\rangle = \frac{1}{i\hbar}\langle[\hat{A}, \hat{\mathscr{H}}]\rangle \tag{1.11}$$

implying that if $[\hat{A}, \hat{\mathscr{H}}] = 0$, then the observable is a conserved quantity - a good quantum number.

Solving Schrödinger's equation on atoms lead to the theory of *atomic orbitals*, describing the electronic states by means of four quantum numbers [26]:

1. **The principal quantum number** n defines the size and energy of the electron's orbit and takes the integral values $n = 1, 2, 3, ...$ The orbits n = 1, 2, 3... are usually termed as "K, L, M,..." shells in the spectroscopic notation.

2. **The orbital momentum (azimuthal) quantum number** l characterizes the electron's angular momentum arising from its orbital motion. It emerges from the eigenvalues of the $\hat{\boldsymbol{L}}^{\boldsymbol{2}}$ operator: $\hat{\boldsymbol{L}}^{\boldsymbol{2}}|l, m_l\rangle = l(l+1)\hbar^2|l, m_l\rangle$ (where $|l, m_l\rangle$ are the eigenfunctions of $\hat{\boldsymbol{L}}^{\boldsymbol{2}}$ and $\hat{L}_z$ - spherical harmonics). The value of l defines the subshells of the energy level n and can take integral values of $0, 1, 2, ..., n-1$. The size of the electron's orbital momentum in the l-subshell is then equal to $L = \sqrt{l(l+1)}\hbar$. The $l = 0, 1, 2, 3, 4, 5, ...$ subshells are usually called "s, p, d, f, g, h, ..." orbitals.

3. **The magnetic quantum number** m_l tells us the size of the quantized projection of orbital momentum along a specific direction, which is usually the direction of an applied field (the z-axis by definition). It arises from the eigenvalues of the $\hat{L}_z$ operator: $\hat{L}_z|l, m_l\rangle = m_l\hbar|l, m_l\rangle$ and can take integral values, which for a given l lie in the range $m_l = -l, -l+1, ..., l-1,\ l$, measured in units of $\hbar$. This gives a total of $2l+1$ possible projections of orbital momentum along the z axis for a specific l.

4. **The spin quantum number** m_s describes the quantized projection of the electron spin along a specific direction, which is usually the direction of an applied field (the z-axis by definition). It originates from the eigenvalues of the $\hat{S}_z$ operator ($\hat{S}_z = \frac{\hbar}{2}\hat{\sigma}_z$) and takes the values $m_s = \pm\frac{1}{2}$, measured in the units of $\hbar$. The spin components are then $+\hbar/2$ (spin-up) or $-\hbar/2$ (spin-down). For a particle with the spin s, the allowed projections are $m_s = -s, -s+1, ..., s-1, s$ (a total $2s+1$ projections) and the size of the spin angular momentum is $S = \sqrt{s(s+1)}\hbar$, specifically $\frac{\sqrt{3}}{2}\hbar$ for the electron.

The orbital magnetic moment $\hat{\boldsymbol{\mu}}_{\boldsymbol{L}}$ associated with the orbital angular momentum $\hbar\hat{\boldsymbol{L}}$ is defined as

$$\hat{\boldsymbol{\mu}}_{\boldsymbol{L}} = -\frac{e}{2m_e}\hbar\hat{\boldsymbol{L}} = -\mu_B\hat{\boldsymbol{L}} \tag{1.12}$$

with the magnitude

$$|\hat{\boldsymbol{\mu}}_{\boldsymbol{L}}| = \frac{e}{2m_e}\sqrt{l(l+1)}\hbar = \mu_B\sqrt{l(l+1)} \tag{1.13}$$

and the projection along the z-axis:

$$\mu_{L,z} = -m_l\mu_B \tag{1.14}$$

The spin magnetic moment $\hat{\boldsymbol{\mu}}_{\boldsymbol{S}}$ associated with the electron's spin angular momentum $\hbar\hat{\boldsymbol{S}}$ is defined as

$$\hat{\boldsymbol{\mu}}_{\boldsymbol{S}} = -g_S\mu_B\hat{\boldsymbol{S}} \tag{1.15}$$

where $g_S = 2.0023 \approx 2$ is the electron's g-factor. The magnitude of $\hat{\boldsymbol{\mu}}_{\boldsymbol{S}}$:

$$|\hat{\boldsymbol{\mu}}_{\boldsymbol{S}}| = g_S\mu_B\sqrt{s(s+1)} = \frac{\sqrt{3}}{2}g_S\mu_B \tag{1.16}$$

and the projection along the z-axis:

$$\mu_{S,z} = -g_S m_S\mu_B \tag{1.17}$$

1.3 Magnetization, magnetic susceptibility

We have shown that the atomic magnetic moment arises from two distinc sources - the former coming from the electron's orbital motion, the latter coming from the electron's spin contribution.

A real magnetic solid, however, consists of a great number of atoms carrying magnetic moments. It is therefore convenient to define a new quantity - *magnetization* $\boldsymbol{M}$, as the net magnetic moment $\boldsymbol{m}$ per unit volume V [29]:

$$\boldsymbol{M} = \frac{\boldsymbol{m}}{V} \tag{1.18}$$

The magnetic field inside a magnetic material can be expressed in terms of vector fields $\boldsymbol{B}$ (*the magnetic induction*), $\boldsymbol{H}$ (*the magnetic field strength*) and magnetisation $\boldsymbol{M}$, related by the following relation [27]:

$$\boldsymbol{B} = \mu_0(\boldsymbol{H} + \boldsymbol{M}) \tag{1.19}$$

where $\mu_0 = 4\pi\times10^{-7}$ Hm^{-1} is the permeability of vacuum. The magnetic field $\boldsymbol{H}$ is generated by electrical currents outside the magnetic material (a solenoid, electromagnet or a permanent magnet), so it is often also called "the external/applied field". In free space (where $\boldsymbol{M} = \boldsymbol{0}$), $\boldsymbol{B}$ and $\boldsymbol{H}$ are almost identical, differing only by a scaling factor μ_0 and the units of measurement ($\boldsymbol{B}$ is measured in Tesla, $\boldsymbol{H}$ in Am^{-1}).

We can classify magnetic materials on the basis of their response to a magnetic field. Materials with a linear relationship between the magnetisation and the field

$$\boldsymbol{M} = \chi\boldsymbol{H} \tag{1.20}$$

are called linear materials. We have defined a new dimensionless quantity, *the magnetic susceptibility* χ, as a measure of the type and strength of the material's reaction to the magnetic field. Substituting Equation (1.20) to (1.18), we get

$$\boldsymbol{B} = \mu_0(1+\chi)\boldsymbol{H} = \mu_0\mu_r\boldsymbol{H} \tag{1.21}$$

where we define *the relative magnetic permeability* $\mu_r = 1 + \chi$ of the material.

For non-linear materials, we define *the differential susceptibility*

$$\chi = \frac{\partial \boldsymbol{M}}{\partial \boldsymbol{H}} \tag{1.22}$$

which is usually a tensor in anisotropic magnetic materials ($M_i = \chi_{ij}H_j$).

Due to the definition of $\boldsymbol{M}$, the susceptibility χ defined in Equation (1.19) refers to the magnetic moment induced by the field $\boldsymbol{H}$ per unit volume of the material. There is also a possibility of expressing the induced moment per mole, *the molar magnetic susceptibility* $\chi_m = \chi V_m$ (in m^3 mol^{-1}), where $V_m = M_m/\rho$ is the molar volume - the molar mass M_m divided by the density ρ. *The mass susceptibility* $\chi_g = \chi/\rho$ (in m^3 kg^{-1}) can also be used. [27]

We are able to classify magnetic materials based on their bulk magnetic susceptibility into two major groups - *diamagnetic materials* ($\chi < 0$. typically $\chi \approx -10^{-5}$) with a negative response to the external field, and *paramagnetic materials* ($\chi > 0$, typically $\chi \approx 10^{-3}$ to 10^{-5}) with induced moment parallel to the field. [29] Their origin will be discussed in the following sections.

1.4 Isolated magnetic moments

Let us now focus on the magnetic properties of isolated atoms (or ions), where we take the approximation of neglecting the interactions between these atoms/ions or with their close environment.

Consider an atom (ion) with Z electrons inside a magnetic field $\boldsymbol{B}$. We can write the Hamiltonian of this system [27] as a sum of the electrons' kinetic energy, potential energy and the magnetic potential energy of the spin magnetic moment ($U = -\hat{\boldsymbol{\mu}}_{\boldsymbol{S}} \cdot \boldsymbol{B}$, see (1.7) and (1.15)) coming from the total spin $\hat{\boldsymbol{S}} = \sum_{i=1}^{Z} \frac{\hbar}{2} \hat{\boldsymbol{\sigma}}_{\boldsymbol{i}}$:

$$\hat{\mathscr{H}} = \sum_{i=1}^{Z} \left(\frac{\left(\hat{\boldsymbol{p}}_{\boldsymbol{i}} + e\hat{\boldsymbol{A}}(\boldsymbol{r}_{\boldsymbol{i}}) \right)^2}{2m_e} + V_i \right) + g_S \mu_B \hat{\boldsymbol{S}} \cdot \boldsymbol{B} \tag{1.23}$$

where $\hat{\boldsymbol{A}}(\boldsymbol{r})$ is the magnetic vector potential generating the field ($\boldsymbol{B} = \nabla \times \hat{\boldsymbol{A}}$) as well as altering the electron's momentum, and V_i is the electrostatic potential energy felt by the i-th electron at the position $\boldsymbol{r}_{\boldsymbol{i}}$.

If $\boldsymbol{B}$ is uniform and constant, we can choose the symmetric gauge for the vector potential $\hat{\boldsymbol{A}}(\boldsymbol{r}) = \frac{1}{2} \boldsymbol{B} \times \hat{\boldsymbol{r}}$. Substituting in (1.21), expanding the squared term and identifying the total angular momentum $\hbar \hat{\boldsymbol{L}} = \sum_{i=1}^{Z} \hat{\boldsymbol{r}}_{\boldsymbol{i}} \times \hat{\boldsymbol{p}}_{\boldsymbol{i}}$, we get

$$\begin{aligned} \hat{\mathscr{H}} &= \underbrace{\sum_{i=1}^{Z} \left(\frac{\hat{\boldsymbol{p}}_{\boldsymbol{i}}^{\,2}}{2m_e} + V_i \right)}_{\hat{\mathscr{H}}_0} + \underbrace{\mu_B \left(\hat{\boldsymbol{L}} + g_S \hat{\boldsymbol{S}} \right) \cdot \boldsymbol{B} + \frac{e^2}{8m_e} \sum_{i=1}^{Z} \left(\boldsymbol{B} \times \boldsymbol{r}_{\boldsymbol{i}} \right)^2}_{\Delta \hat{\mathscr{H}}} \\ &= \qquad \hat{\mathscr{H}}_0 \qquad + \qquad \Delta \hat{\mathscr{H}} \end{aligned} \tag{1.24}$$

where $\hat{\mathscr{H}}_0$ is the unperturbed Hamiltonian (the kinetic energy from the moving electrons plus the Coulombic energy from the nucleus and electron-electron interactions) and $\Delta \hat{\mathscr{H}}$ is the perturbation causing the atomic magnetic properties.

Since $\Delta \hat{\mathscr{H}}$ is a small perturbation on the scale of atomic excitation energies even for very high fields, we can utilize the second-order perturbation theory [30]:

$$\Delta E_n = \langle n | \Delta \hat{\mathscr{H}} | n \rangle + \sum_{n' \neq n} \frac{\left| \langle n | \Delta \hat{\mathscr{H}} | n' \rangle \right|^2}{E_n - E_{n'}} \tag{1.25}$$

which tells us the change in the energy level $|n\rangle$ induced by the magnetic field.

Assuming $\boldsymbol{B} = (0, 0, B)$ oriented along the z-axis, then $\boldsymbol{B} \times \boldsymbol{r}_{\boldsymbol{i}} = B(-y_i, x_i, 0)$ and we get the fundamental equation for the calculation of atomic susceptibilities (we are retaining the terms linear and quadratic in $\boldsymbol{B}$):

$$\begin{aligned} \Delta E_n = \mu_B \boldsymbol{B} \cdot \langle n | \hat{\boldsymbol{L}} + g_S \hat{\boldsymbol{S}} | n \rangle + \sum_{n' \neq n} \frac{\left| \langle n | \mu_B \boldsymbol{B} \cdot (\hat{\boldsymbol{L}} + g_S \hat{\boldsymbol{S}}) | n' \rangle \right|^2}{E_n - E_{n'}} \\ + \frac{e^2}{8m_e} B^2 \langle n | \sum_{i=1}^{Z} (x_i^2 + y_i^2) | n \rangle \end{aligned} \tag{1.26}$$

As we will later see, the first two terms are responsible for a positive field-induced magnetic moment – *paramagnetism*, while the third term causes a negative field-induced moment (antiparallel to $\boldsymbol{B}$) – *diamagnetism*.

Using the first law of thermodynamics $dU = TdS - pdV + \boldsymbol{B} \cdot d\boldsymbol{M}$ for the magnetic system, we can express the Helmholtz free energy $F = U - TS - \boldsymbol{B} \cdot \boldsymbol{M}$ in the differential form as follows

$$dF = -SdT - pdV - \boldsymbol{M} \cdot d\boldsymbol{B} \tag{1.27}$$

Now we see that the magnetization induced by the external field $\boldsymbol{B} = \mu_0 \boldsymbol{H}$ (and the magnetic susceptibility χ) is given by the thermodynamic relation

$$M = -\left(\frac{\partial F}{\partial B}\right)_{T,V} \qquad \text{and} \qquad \chi = \left(\frac{\partial M}{\partial H}\right) = -\mu_0 \left(\frac{\partial^2 F}{\partial B^2}\right)_{T,V} \tag{1.28}$$

1.4.1 Diamagnetism

Diamagnetism, a weak effect present in all materials, is characterised by a negative magnetic moment induced by the external magnetic field, resulting in a negative magnetic susceptibility $\chi < 0$.

It is often explained in the classical sense by means of Lenz's law, where the external magnetic field acts on the current loops produced by the orbiting electrons, inducing a back electromotive force opposing the external field. [27]

However, the origin of diamagnetism is purely quantum-mechanical. Let us suppose the simplest case - a solid composed of atoms (ions) with fully occupied electronic shells. In the ground state $|0\rangle$, the total orbital and spin angular momentum will be zero

$$\hat{\boldsymbol{L}}|0\rangle = \hat{\boldsymbol{S}}|0\rangle = 0 \tag{1.29}$$

so only the third term in Equation (1.26) is non-zero and causes a shift in the ground-state energy induced by the applied field. For a spherically symmetric atom, $\langle x_i^2 \rangle = \langle y_i^2 \rangle = \langle z_i^2 \rangle = \frac{1}{3}\langle r_i^2 \rangle$ (r_i is the radius of the i-th electron's orbit), so

$$\Delta E_0 = \frac{e^2 B^2}{12 m_e} \sum_{i=1}^{Z} \langle 0 | r_i^2 | 0 \rangle \tag{1.30}$$

Applying (1.28) on a solid with N atoms (ions) in a volume V at $T = 0$, the so-called *Larmor diamagnetic susceptibility* will then be [30]

$$\chi = -\frac{N}{V}\mu_0 \left(\frac{\partial^2 \Delta E_0}{\partial B^2}\right) = -\frac{N}{V}\frac{e^2 \mu_0}{6 m_e} \sum_{i=1}^{Z} \langle 0 | r_i^2 | 0 \rangle \tag{1.31}$$

Diamagnetism is therefore dominant in noble gases (He, Ne, Ar, ...) and simple ionic salts (Na^+Cl^-, Na^+F^-, K^+Br^-, ...), where the ions possess a closed-shell electronic structure. If we ignore the ion's inner-shell electrons, Z_{eff} outer-shell electrons will have approximately the same radius, so $\sum_{i=1}^{Z_{\text{eff}}} \langle 0 | r_i^2 | 0 \rangle \approx Z_{\text{eff}} \langle r^2 \rangle$. Larmor susceptibility is thus proportional to the mean square ionic radius $\langle r^2 \rangle$.

As we increase the temperature above absolute zero, the excited states will get progressively more populated, influencing the resultant diamagnetic susceptibility. The effect is, however, very small and can be ignored.

For a solid containing atoms (ions) with partially filled electronic shells ($\hat{\boldsymbol{L}} \neq 0$ and/or $\hat{\boldsymbol{S}} \neq 0$), the result is very different as all three terms in (1.26) contribute to the field-induced energy change and influence the magnetic susceptibility (1.28).

1.4.2 Paramagnetism

As mentioned before, paramagnetism is characterised by a positive induced magnetic moment upon the application of an external magnetic field, therefore showing a positive magnetic susceptibility $\chi > 0$.

As opposed to the previous section where we assumed atoms (ions) with fully occupied electronic shells (thus carrying no magnetic moment), paramagnetism arises from unpaired electrons which produce a non-zero magnetic moment.

In a solid, these moments point randomly in all directions as they are dynamically fluctuating from the thermal energy of phonons, and the net moment averages to zero. As we apply the field, the moments start to partially line up with the field, causing a non-zero net magnetization. However, if we increase the temperature, the thermal vibration of atoms will tend to destabilize the spins aligned with the field. The resultant magnetization thus depends on the ratio B/T - the strength of the applied field versus the temperature of the paramagnetic solid.

Let us suppose a free (non-interacting) atom with all electronic shells filled except for one, characterized by the orbital angular momentum l and with n electrons occupying this shell. With regards to Pauli's exclusion principle, there is a total of $2(2l+1)$ possible electronic states (2 possible directions of spin for each of the $2l+1$ projections of L_z). If the electrons were non-interacting, the groundstate would be $\binom{2(2l+1)}{n}$-times degenerate. However, this degeneracy is lifted by the Coulombic interaction between the electrons, and also by the spin-orbit interaction, which arises due to the interaction of the electron's spin with the magnetic field produced by the electron's orbital motion.

In the approximation of weak spin-orbit coupling, the atomic (ionic) Hamiltonian commutes not only with the total electronic spin and orbital angular momenta, $\boldsymbol{S} = \sum_{i=1}^{n} \boldsymbol{S_i}$ and $\boldsymbol{L} = \sum_{i=1}^{n} \boldsymbol{L_i}$, but also with *the total angular momentum*

$$\boldsymbol{J} = \boldsymbol{L} + \boldsymbol{S} \tag{1.32}$$

This coupling of the total spin and orbital angular momentum is called *the Russel-Saunders coupling* or the LS coupling. [30] We can therefore describe the electronic states by means of quantum numbers L, L_z, S, S_z, J and J_z, since they are the eigenstates of operators $\hat{\boldsymbol{L}}^{\boldsymbol{2}}$, $\hat{L}_z$, $\hat{\boldsymbol{S}}^{\boldsymbol{2}}$, $\hat{S}_z$, $\hat{\boldsymbol{J}}^{\boldsymbol{2}}$ and $\hat{J}_z$ with their respective eigenvalues $L(L+1)$, L_z, $S(S+1)$, S_z, $J(J+1)$ and J_z. The possible projections of J_z (for a given J) are $-J, -J+1, ..., J-1, J$, giving a total of $2J+1$ projections, measured in the units of $\hbar$.

If we treated $\boldsymbol{L}$ and $\boldsymbol{S}$ total angular momenta as independent (non-interacting), they could combine into $(2L+1)(2S+1)$ possible states ($2L+1$ possible $\hat{L}_z$ projections for each of the $2S+1$ possible $\hat{S}_z$ projections). However, a weak LS coupling occurs in the presence of a weak spin-orbit interaction (considered as a small perturbation), where the LS states are split into a number of states with differing J, also known as *the fine structure*. J can take values between $|L-S|$ and $L+S$ in integral steps, each J having a total number of $2J+1$ projections of J_z. This can be shown as

$$\sum_{J=|L-S|}^{L+S} 2J+1 = (2L+1)(2S+1) \tag{1.33}$$

There are two cases in which paramagnetism arises depending on J [30]:

(a) $\boldsymbol{J = 0}$: The shell is one electron short of being half-filled ($n = 2l$). In contrast to the fully occupied shell case (1.29), the total angular momenta $\boldsymbol{L}$ and $\boldsymbol{S}$ are non-zero, so the second and third term in (1.26) prevail. According to (1.28), the paramagnetic susceptibility is then [27]

$$\chi = \frac{N}{V}\left(2\mu_B^2\mu_0 \sum_{n'\neq 0} \frac{\left|\langle 0|\hat{L}_z + g_S\hat{S}_z)|n'\rangle\right|^2}{E_n - E_0} - \frac{e^2\mu_0}{6m_e}\sum_{i=1}^{Z}\langle 0|r_i^2|0\rangle\right) \tag{1.34}$$

The first term is positive and causes *the Van Vleck paramagnetism*. It arises from the excited states n' with $J \neq 0$, which cause a field-induced change of the ground-state energy. The second term is diamagnetic as discussed in the previous section. Both terms are temperature independent and small.

(b) $\boldsymbol{J \neq 0}$: This covers all cases except for fully occupied shells and the case above. The first term in (1.26) does not vanish and becomes dominant to the extent that the remaining two terms can be neglected. In zero field, the groundstate is $(2J+1)$-times degenerate and we can utilize *Wigner-Eckart's theorem* to evaluate the $(2J+1)$-dimensional square matrix in the $|JLSJ_z\rangle$ basis [30]

$$\langle JLSJ_z|\hat{\boldsymbol{L}} + g_S\hat{\boldsymbol{S}}|JLSJ'_z\rangle = g_J\langle JLSJ_z|\hat{\boldsymbol{J}}|JLSJ'_z\rangle \tag{1.35}$$

where g_J is *the Landé g-factor*, which in the $g_S \approx 2$ approximation takes the form

$$g_J = 1 + \frac{J(J+1) - L(L+1) + S(S+1)}{2J(J+1)} \tag{1.36}$$

The magnetic moment from the total angular momentum $\boldsymbol{J}$ is then given by

$$\hat{\boldsymbol{\mu}}_{\boldsymbol{J}} = -g_J\mu_B\hat{\boldsymbol{J}}, \qquad |\hat{\boldsymbol{\mu}}_{\boldsymbol{J}}| = g_J\mu_B\sqrt{J(J+1)} \tag{1.37}$$

Since the zero-field ground state is degenerate, we cannot calculate the susceptibility by setting the free energy equal to the ground-state energy shift. Instead, we have to employ statistical mechanics. The external field splits the degeneracy into $2J+1$ equidistant energy levels - this effect is also known as *the Zeeman splitting*:

$$E = -\hat{\boldsymbol{\mu}}_{\boldsymbol{J}} \cdot \boldsymbol{B} = g_J\mu_B J_z B, \qquad J_z \in \{-J, -J+1, ..., J-1, J\} \tag{1.38}$$

The free energy of the lowest-energy $2J+1$ multiplet (assuming it is the only reasonably thermally populated multiplet) is given by [30]

$$F = -k_B T\ \mathrm{ln}Z, \qquad Z = \sum_{J_z=-J}^{J} \exp\left(-\frac{g_J\mu_B J_z B}{k_B T}\right) \tag{1.39}$$

where k_B is the Boltzmann constant and Z is the partition function.

Finally, the magnetization of the paramagnetic solid is then calculated as

$$M = -\frac{N}{V}\frac{\partial F}{\partial B} = \frac{N}{V}g_J\mu_B J B_J(x) \tag{1.40}$$

where $B_J(x)$ is *the Brillouin function* defined as

$$B_J(x) = \frac{2J+1}{2J}\coth\left(\frac{2J+1}{2J}x\right) - \frac{1}{2J}\coth\left(\frac{1}{2J}x\right), \quad x = \frac{g_J\mu_B J_z B}{k_B T} \tag{1.41}$$

In the limit of low temperatures or high fields, $B_J(x) \xrightarrow{x\to\infty} 1$, resulting in *the saturation magnetization* M_s as all moments align with the field:

$$M_s = \frac{N}{V} g_J \mu_B J \quad \text{or} \quad \mu_s = g_J \mu_B J \tag{1.42}$$

In the limit of high temperatures or low fields, $\coth x \approx \frac{1}{x} + \frac{x}{3} + O(x^3)$ for small x, giving $B_J(x) \approx \frac{J+1}{3J}x + O(x^3)$. This leads to the famous temperature dependence of paramagnetic susceptibility, *the Curie law*:

$$\chi = \frac{N}{V}\frac{\mu_0(g_J\mu_B)^2}{3}\frac{J(J+1)}{k_B T} = \frac{C}{T} \tag{1.43}$$

or in the molar form ($N_A = 6.022 \times 10^{23}$ mol^{-1} is the Avogadro constant)

$$\chi^{\text{mol}} = N_A\frac{\mu_0(g_J\mu_B)^2}{3}\frac{J(J+1)}{k_B T} = \frac{C^{\text{mol}}}{T} \tag{1.44}$$

We see that the susceptibility is inversely proportional to the temperature. The Curie constant C^{mol} is proportional to the square of *the effective magnetic moment* μ_{eff}:

$$C^{\text{mol}} = \frac{N_A\mu_0\mu_{\text{eff}}^2}{3k_B}, \quad \mu_{\text{eff}} = g_J\mu_B\sqrt{J(J+1)} \tag{1.45}$$

By performing a linear fit on $1/\chi^{\text{mol}}$ vs. T, we are able to extract the effective magnetic moment per one mole of the magnetic ion in the solid. Using $C^{\text{mol}} = \chi^{\text{mol}}T$ and rearranging (1.45) as $\mu_{\text{eff}} = (3k_B/N_A\mu_0\mu_B^2)^{1/2}\sqrt{\chi^{\text{mol}}T}$, we can plot the temperature dependence of the effective moment [27]

$$\mu_{\text{eff}}(T) = 797.8\sqrt{\chi_{SI}^{\text{mol}}T} \approx 800\sqrt{\chi_{SI}^{\text{mol}}T} \qquad \text{(SI)} \tag{1.46}$$

$$\mu_{\text{eff}}(T) = 2.827\sqrt{\chi_{cgs}^{\text{mol}}T} \approx \sqrt{8\chi_{cgs}^{\text{mol}}T} \qquad \text{(cgs)} \tag{1.47}$$

where we evaluated the constant according to the units of measurement. Here, μ_{eff} is measured in $\mu_B/f.u.$ (Bohr magnetons per formula unit) , χ_{SI}^{mol} is measured in m^3 mol^{-1} and χ_{cgs}^{mol} is measured in emu mol^{-1}.

1.4.3 Hund's rules

In the previous section, we talked about the LS coupling in the case of a weak spin-orbit interacion. In that case, the total orbital and spin momenta L and S can couple into a total angular momentum J, which can take the values $J \in \{|L-S|, |L-S|+1, ..., L+S-1, L+S\}$. The size of L and S and their combination into J, which minimize the energy of the atom (ion) and define its groundstate, can be approximated by means of three *Hund's rules* [30]:

1. *Hund's first rule:* The lowest-energy electronic configuration of a partially filled shell corresponds to the maximal total spin S, or equivalently, the largest magnitude of the projection $S_z = \sum_{i=1}^{n} m_{s,i}$. This configuration results in the lowest Coulombic repulsion between electrons, pushing them further apart and preventing two parallel spins in the same place, in consistency with Pauli's exclusion principle.

2. *Hund's second rule:* To find the lowest-energy electronic configuration, one has to maximize the total orbital momentum L in consistency with the first Hund's rule and the exclusion principle. This is equivalent to finding the largest possible projection $L_z = \sum_{i=1}^{n} m_{l,i}$. We can imagine this as electrons orbiting in the same direction, helping them avoid each other, thus reduce the Coulombic repulsion and minimize the energy.

3. *Hund's third rule:* The value of J corresponding to the lowest-energy electronic configuration (in agreement with the first and second Hund's rule) is found as

   (a) $J = |L - S|$, if the shell is less than half full ($n < 2l + 1$)

   (b) $J = L + S$, if the shell is more than half full ($n > 2l + 1$)

   (c) $J = S$, if the shell is exactly half full, since $L = 0$ ($n = 2l + 1$).

   This defines the lowest-lying J-multiplet, usually described by *the spectroscopic term symbol* ${}^{2S+1}X_J$, where the letter $X = S, P, D, F, G, H, I, ...$ corresponds to the total orbital angular momentum $L = 0, 1, 2, 3, 4, 5, 6, ...$

So far, we have only assumed free isolated atoms (ions) for which Curie's law and Hund's rules were derived. However, experiments show that insulating crystals containing rare-earth ions with partially-filled electronic f-shells obey Curie's law fairly well and the measured effective moment matches extremely well with the predicted value from (1.45) (see Attachment A.1). The only discrepancy is found in Sm and Eu, where the effective moment is affected by the thermal population of the second-lowest J-multiplet, which lies very close in energy to the ground state. The good agreement between the theoretical prediction and the experiment comes from the contracted nature of $4f$ orbitals in rare-earth ions, which interact very weakly with the crystal environment or other rare-earth ions and can therefore be considered as isolated ions.

The situation is different for transition metal ions in insulating solids. Although Curie's law is obeyed for the iron group $3d$ metals, the effective moment appears to better match the predicted value corresponding to $J = S$ with zero orbital moment $L = 0$ (see Attachment A.2). The orbital angular momentum is said to be *quenched* due to the interaction of the far-extending $3d$ orbitals with the electric field produced by the crystal environment around the magnetic ion. The origin and consequences of the *crystal electric field* will be discussed in the following section.

1.5 Crystal electric field

The electrostatic field produced by negative ions surrounding a positively charged magnetic ion inside the crystal is known as *the crystal electric field* (CEF). The defining factor of the size and nature of the crystal field is the symmetry of the local environment given by the crystallographic site of the magnetic ion.

The crystal field theory is used to model the splitting of degenerate electronic levels, usually d and f orbitals. For rare earth ions with partially filled $4f$ shells, the CEF splitting is not very significant, as the $4f$ orbitals are located deep inside the ion, shielded by the filled $5s$ and $5p$ shells. On the contrary, the extended nature of the d orbitals results in a much larger overlap with the orbitals of the neighbouring ions - *ligands*.

The d orbitals are classified into two groups - the t_{2g} orbitals (d_{xy}, d_{xz}, d_{yz}), the lobes of which point between the cartesian coordinate axes, and the e_g orbitals ($d_{x^2-y^2}$, d_{z^2}), the lobes of which point along these axes. The CEF splitting of the t_{2g} and e_g levels depends on the symmetry of the magnetic ion's local environment.

In the case of octahedral coordination, there will be a higher overlap of the e_g orbitals with the ligands' p orbitals, resulting in a larger electrostatic energy and consequently, t_{2g} orbitals will be lower in energy. In the case of tetrahedral symmetry, the overlap of t_{2g} and p orbitals is higher, placing the triply-degenerate t_{2g} orbitals higher in energy than the doubly-degenerate e_g orbitals. [27]

The order of the electron filling of $3d$ orbitals in transition metal ions depends on the size of the crystal field energy in comparison with the Coulombic energy arising from the repulsion of two electrons in the same orbital (*the pairing energy*). In *the weak-field case*, the electrons first singly occupy each orbital before pairing up. In *the strong-field case*, where the CEF energy is larger than the pairing energy, the electrons first doubly occupy the lowest energy levels before occupying the higher-energy orbitals.

The CEF affects the magnetic ground state of $3d$ metal ions, making it different from the one predicted by Hund's rules using the J, L and S values. Experiments show that the effective moment is closer to the value calculated for $L = 0$ ($J = S$, $g_J = 2$) - this effect is called *quenching of orbital moment*:

$$\mu_{\text{eff}} = 2\sqrt{S(S+1)}\mu_B \tag{1.48}$$

The discrepancy arises from the fact that in $3d$ ions, the CEF interaction is much stronger that the weak spin-orbit coupling, making Hund's third rule invalid. In the semiclassical picture, we can imagine the orbital quenching as a precession of $\boldsymbol{L}$ in the crystal field, so the magnitude is unchanged but the components average to zero.

The orbital moment is never exactly zero due to the spin-orbit interaction, which mixes in $L > 0$ states and influences the g-factor value, possibly even causing an anisotropic g-tensor. In the heavier-ion $4d$ and $5d$ transition metals, the situation is much more complex due to the large spin-orbit interaction, which is comparable to or greater than the CEF interaction.

In general, there are two important principles to follow [30]:

1. *The Kramers theorem*: An ion containing an odd number of electrons (hence a half-integer total spin) always has a ground state at least doubly degenerate, even if crystal fields and spin-orbit interactions are present.

2. *The Jahn-Teller effect*: If a magnetic ion sits in a crystallographic site of such high symmetry that its ground state is not the Kramers minimum, the crystal geometrically distorts to a more energetically favorable configuration with a lower symmetry, breaking the ground-state degeneracy.

1.6 Magnetic interactions

Thus far, we were able to predict some basic magnetic properties of solids by regarding the magnetic ions as non-interacting, or interacting only with their local environment. As we start decreasing the temperature of the system (i.e. the thermal energy $E = k_B T$), however, magnetic interactions between ions become progressively more important and can no longer be neglected. These interactions can cause a variety of magnetic ground states, whether it be a conventional long-range ordered state or a ground state with short-range correlations. In this section, we will review the most common types of magnetic interactions.

1.6.1 Dipolar interaction

The most basic interaction between two magnetic dipoles $\boldsymbol{\mu_1}$ and $\boldsymbol{\mu_2}$ separated by $\boldsymbol{r}$ has the interaction energy equal to [27]

$$E = \frac{\mu_0}{4\pi r^3}\left[\boldsymbol{\mu_1}\cdot\boldsymbol{\mu_2} - \frac{3}{r^2}(\boldsymbol{\mu_1}\cdot\boldsymbol{r})(\boldsymbol{\mu_2}\cdot\boldsymbol{r})\right] \tag{1.49}$$

which depends on the mutual distance and orientation of the dipoles. To provide a rough estimate of the size of this interaction, let us consider two equal magnetic moments of size $\mu = 1\ \mu_B$ separated by $r = 1$ Å. Then, $E = \mu_0\mu^2/4\pi r^3 \sim 10^{-23}$ J, or 1 K on the temperature scale. This interaction is therefore insufficient to cause long range ordering, as some materials order at temperatures as high as 1000 K. The interaction may, however, become important at milliKelvin temperatures.

1.6.2 Exchange interaction

Exchange interaction is a quantum-mechanical phenomenon occuring between identical particles (*fermions* or *bosons*) based on the symmetry of the many-particle wavefunction upon the exchange of particles (*the exchange symmetry*).

The origin of exchange can be illustrated on a simple model. Consider two electrons (a and b) with spatial coordinates $\boldsymbol{r_1}$ and $\boldsymbol{r_2}$. The two-particle wavefunction can be expressed in terms of a product of the spatial single electron states ψ_a and ψ_b and the spin wavefunction χ. The resultant wavefunction must be antisymmetric, as we are dealing with fermions. This gives two options - a product of a symmetric spatial state and an antisymmetric singlet ($S = 0$) spin state χ_S, or a product of an antisymmetric spatial state and a symmetric triplet ($S = 1$) spin state χ_T [27]:

$$\psi_S = \frac{1}{\sqrt{2}}\left(\psi_a(\boldsymbol{r_1})\psi_b(\boldsymbol{r_2}) + \psi_a(\boldsymbol{r_2})\psi_b(\boldsymbol{r_1})\right)\chi_S \tag{1.50}$$

$$\psi_T = \frac{1}{\sqrt{2}}\left(\psi_a(\boldsymbol{r_1})\psi_b(\boldsymbol{r_2}) - \psi_a(\boldsymbol{r_2})\psi_b(\boldsymbol{r_1})\right)\chi_T \tag{1.51}$$

The energies of the singlet state and the triplet state are

$$E_S = \int \psi_S^* \hat{\mathscr{H}} \psi_S \; d\boldsymbol{r_1} d\boldsymbol{r_2} \quad \text{and} \quad E_T = \int \psi_T^* \hat{\mathscr{H}} \psi_T \; d\boldsymbol{r_1} d\boldsymbol{r_2} \tag{1.52}$$

It can be shown that the effective spin-dependent Hamiltonian can be written as

$$\hat{\mathscr{H}}^{\text{spin}} = -2J \hat{\boldsymbol{S}}_\mathbf{1} \cdot \hat{\boldsymbol{S}}_\mathbf{2} \tag{1.53}$$

where J is *the exchange integral* defined as

$$J = \frac{E_S - E_T}{2} = \int \psi_a^*(\boldsymbol{r_1}) \psi_b^*(\boldsymbol{r_2}) \hat{\mathscr{H}} \psi_a(\boldsymbol{r_2}) \psi_b(\boldsymbol{r_1}) \; d\boldsymbol{r_1} d\boldsymbol{r_2} \tag{1.54}$$

We see that if $J > 0$, then $E_S > E_T$ and the triplet state ($S = 1$) is preferred. If $J < 0$, then $E_S < E_T$ and the singlet state ($S = 0$) is preferred.

To evaluate the dot product, we expand $\hat{\boldsymbol{S}}^2 = (\hat{\boldsymbol{S}}_\mathbf{1} + \hat{\boldsymbol{S}}_\mathbf{2})^2$ and use the respective eigenvalues $S(S+1)$ and $s(s+1) = \frac{3}{4}$ for the $s = \frac{1}{2}$ electrons:

$$\hat{\boldsymbol{S}}_\mathbf{1} \cdot \hat{\boldsymbol{S}}_\mathbf{2} = \frac{1}{2}(\hat{\boldsymbol{S}}^2 - \hat{\boldsymbol{S}}_\mathbf{1}{}^2 - \hat{\boldsymbol{S}}_\mathbf{2}{}^2) = \begin{cases} \frac{1}{4} & \text{for } S = 1 \text{ (triplet)} \\ -\frac{3}{4} & \text{for } S = 0 \text{ (singlet)} \end{cases} \tag{1.55}$$

We can generalize this result to a many-body system. By modelling the microscopic origin of magnetic interactions in the solid, we are able to predict the solid's magnetic properties. The most common models are [27]

- *The Heisenberg model*: This model is isotropic, as the localised spins (taken as 3D vectors) are allowed to point in any direction in space. The Heisenberg Hamiltonian is defined as

  $$\hat{\mathscr{H}} = -\sum_{i,j} J_{ij} \hat{\boldsymbol{S}}_\boldsymbol{i} \cdot \hat{\boldsymbol{S}}_\boldsymbol{j} \tag{1.56}$$

  where J_{ij} is the exchange integral between the i-th and j-th spin. Usually, the sum is taken over the nearest neighbours, in that case $J_{ij} = J$ is constant for nearest neighbors and zero otherwise.

- *The Ising model*: The spins are constrained to point only up or down along a specific direction (the z-axis by definition). The Ising Hamiltonian is defined as

  $$\hat{\mathscr{H}} = -\sum_{i,j} J_{ij} \hat{S}_i^z \hat{S}_j^z \tag{1.57}$$

  where the sum is also usually calculated over the nearest-neighbour spins, for which $J_{ij} = J$, otherwise $J = 0$.

1.6.2.1 Direct exchange

One form of exchange interaction, *the direct exchange*, arises due to the direct overlap of magnetic orbitals of neighbouring ions. Despite its simple character, it is hardly seen as the dominant interaction in many materials. Materials containing rare earth ions posess contracted $4f$ orbitals, which are very well localised as they lie close to the nucleus, hence the direct overlap of $4f$ orbitals of neighbouring ions is very small. Although $3d$ orbitals in transition metals (e.g. Fe, Co, Ni) extend much further, there is a conflict between the localised and itinerant magnetism as conduction electrons come into play. As a result, some type of indirect exchange is often present.

1.6.2.2 Superexchange (indirect exchange)

An indirect exchange mechanism between two next-to-nearest neighbouring magnetic ions, which is mediated by a non-magnetic ion sitting between them is called *the superexchange*. Unlike in the direct exchange, there is no direct overlap of orbitals between the magnetic ions, however, a third non-magnetic ion serves as a mediator of the electronic-wavefunction overlap, correlating the spin states on the magnetic ions. This type of exchange interaction is typical for ionic solids containing $3d$-transition-metal cations ($M = Mn^{2+}$, Fe^{2+}, $Co^{2+}, ...$) and the mediator anions such as oxygen and fluorine ($X = O^{2-}$, F^{-}). The interaction is then realized via the $M(3d) - X(2p) - M(3d)$ exchange pathway and is strongly dependent on the distance of the ions and the $M - X - M$ bond angle. Usually, the exchange interaction is antiferromagnetic for a 180° bond and ferromagnetic for a 90° bond.

1.6.2.3 Antisymmetric (Dzyaloshinsky-Moriya) exchange

An exchange interaction between the excited state of a magnetic ion, where the excitation is induced by spin-orbit coupling, and the ground state of another magnetic ion is known as the *antisymmetric* or *Dzyaloshinsky-Moriya interaction*. It is described by a term contributing to the ordering Hamiltonian [27]

$$\hat{\mathscr{H}}_{ij}^{\mathrm{DM}} = \boldsymbol{D} \cdot \hat{\boldsymbol{S}}_{\boldsymbol{i}} \times \hat{\boldsymbol{S}}_{\boldsymbol{j}} \tag{1.58}$$

where $\boldsymbol{D}$ is a vector dependent on the crystal symmetry, and vanishes if the crystal field has an inversion symmetry with respect to the center between the two magnetic ions. This type of interaction forces the spins $\hat{\boldsymbol{S}}_{\boldsymbol{i}}$ and $\hat{\boldsymbol{S}}_{\boldsymbol{j}}$ to be perpendicular to one another, while the $\boldsymbol{D}$ vector want to be oriented perpendicular to the plane formed by the spins in such a direction that minimizes the energy. This leads to a canting of the spins (a tilting by a small angle), resulting in a small perpendicular ferromagnetic component (*a weak ferromagnetism*) in antiferromagnetic materials such as α-Fe_2O_3, $MnCO_3$ or $CoCO_3$.

1.6.2.4 RKKY interaction (indirect exchange)

Another type of indirect exchange is the RKKY (Ruderman–Kittel–Kasuya–Yosida) interaction. It can only be realized in metals, as the mediators of this exchange interaction are conduction electrons. A magnetic ion with a localized magnetic moment induces a spin polarization on the conduction electrons, which then transfer the polarization to a neighbouring localized magnetic moment at a distance r. The exchange integral (assuming large r) is proportional to [27]

$$J_{RKKY}(r) \propto \frac{\cos(2k_F r)}{r^3} \tag{1.59}$$

where k_F is the Fermi sphere radius, assuming the free-electron model. The interaction has an oscillatory character with a period of π/k_F, hence changes between antiferromagnetic ($J_{RKKY}(r) < 0$) and ferromagnetic ($J_{RKKY}(r) > 0$), depending on the separation of localised moments r.

1.7 Magnetic order

In this section, we will discuss the possible magnetic ground states that can arise from the interactions discussed in Section 1.6. These ground states are usually reached when the temperature of the magnetic solid is low enough, so that the energy of magnetic interactions overcomes the energy of thermal fluctuations, allowing for a creation of a magnetically ordered state.

1.7.1 Ferromagnetism

Ferromagnetism is one of the most important realizations of magnetic order, as it is characterized by having a spontaneous magnetization even when the external magnetic field is not present.

In the simplest case, the net magnetic moment arises from the collinear alignment of all spins along one direction. In most ferromagnets, however, small regions with parallel spins (*magnetic domains*) are created to minimize the magnetostatic energy.

The Hamiltonian of a $3d$-metal ferromagnet ($L = 0$, $J = S$) in a magnetic field consists of the Heisenberg exchange term and the Zeeman energy term [27]

$$\hat{\mathscr{H}} = -\sum_{i,j} J_{ij} \hat{\boldsymbol{S}}_{\boldsymbol{i}} \cdot \hat{\boldsymbol{S}}_{\boldsymbol{j}} + g_S \mu_B \sum_j \hat{\boldsymbol{S}}_{\boldsymbol{j}} \cdot \boldsymbol{B} \tag{1.60}$$

To solve this Hamiltonian, we can employ the *Weiss molecular field theory* by defining an effective molecular field $\boldsymbol{B}_{\mathrm{mf}}$ at the i-th site

$$g_S \mu_B \boldsymbol{B}_{\mathrm{mf}} = -2 \sum_j J_{ij} \boldsymbol{S}_{\boldsymbol{j}} \tag{1.61}$$

which can be understood as a mean field produced by all spins surrounding the i-th spin (the factor 2 comes from summing each pair twice). The Hamiltonian reduces to

$$\hat{\mathscr{H}} = g_S \mu_B \sum_i \hat{\boldsymbol{S}}_{\boldsymbol{i}} \cdot (\boldsymbol{B} + \boldsymbol{B}_{\mathrm{mf}}) \tag{1.62}$$

where we assume that each spin feels the same molecular field. Since the molecular field is a measure of the magnetic ordering, we can assume that

$$\boldsymbol{B}_{\mathrm{mf}} = \lambda \boldsymbol{M} \tag{1.63}$$

where λ is the *Weiss molecular field constant* ($\lambda > 0$ for a ferromagnet). We are now able to treat the Hamiltonian as that of a paramagnet in a magnetic field $\boldsymbol{B} + \boldsymbol{B}_{\mathrm{mf}}$. Therefore, we can utilise the results from (1.40), (1.41) and (1.42) and solve

$$\frac{M}{M_s} = B_J(x), \qquad x = \frac{g_J \mu_B J (B + \lambda M)}{k_B T} \tag{1.64}$$

where we still assume $L = 0$ ($J = S$). As a result, we get a non-zero magnetization from an ordered state below the transition temperature called *the Curie temperature* T_C, defined as

$$T_C = \frac{C\lambda}{\mu_0} = \frac{n\lambda\mu_{\mathrm{eff}}^2}{3k_B}, \quad \text{where} \quad \lambda = \frac{2z\tilde{\mathrm{J}}}{n g_J^2 \mu_B^2} \tag{1.65}$$

where the molecular field constant λ is related to the effective exchange interaction $\tilde{\mathrm{J}}$ with z nearest neighbours and C is the Curie constant from (1.43).

If we apply a small field in the paramagnetic state (above T_C), we can use the approximation of $B_J(x)$ for $x \ll 1$ and we get *the Curie-Weiss law* [31]

$$\chi = \frac{C}{T - \theta_{\mathrm{CW}}} \tag{1.66}$$

where C is the Curie constant from (1.45) and θ_{CW} is *the Curie-Weiss temperature*. In a ferromagnet, $\theta_{\mathrm{CW}} > 0$ and we expect $\theta_{CW} \approx T_C$. The Curie-Weiss temperature, measured in Kelvin (or equivalently $E = k_B\theta_{\mathrm{CW}}$ on the energy scale), gives an approximate mean-field strength of the exchange interaction between the neighbouring spins (see (1.65)).

1.7.2 Antiferromagnetism

Antiferromagnetic order is known for the antiparallel alignment of neighbouring spins, characterized by a negative exchange integral ($J_{ij} < 0$) and a zero net moment in the absence of an applied field. In the simplest case, this configuration can arise from two ferromagnetic sublattices with moments of equal size and an antiparallel orientation.

Just like with ferromagnets, we can employ the Weiss molecular theory, this time for two ferromagnetically ordered sublattices with equal and opposite molecular fields $B_+ = -|\lambda| M_-$ and $B_- = -|\lambda| M_+$ (in antiferromagnets, λ is negative). Since $|M_-| = |M_+| \equiv M$, the magnetization of each sublattice in zero field is

$$\frac{M}{M_s} = B_J\left(\frac{g_J\mu_B J |\lambda| M}{k_B T}\right) \tag{1.67}$$

which leads to similar results derived for a ferromagnet. Below the transition temperature, *the Néel temperature* T_N defined as

$$T_N = \frac{C|\lambda|}{\mu_0} = \frac{n|\lambda|\mu_{\mathrm{eff}}^2}{3k_B} \tag{1.68}$$

the antiferromagnetic ordering occurs. Above T_N, the material is in the paramagnetic state and in a small applied field, the Curie-Weiss law defined in (1.66) is obeyed. For antiferromagnets, $\theta_{\mathrm{CW}} < 0$ and one would expect $\theta_{\mathrm{CW}} \approx -T_N$. In real materials, however, θ_{CW} often largely differs from $-T_N$ as the assumption that the molecular field on one lattice is induced purely by the other sublattice is insufficient.

1.7.3 Ferrimagnetism

Ferrimagnets are magnetically ordered materials which, in a similar fashion as antiferromagnets, consist of two interpenetrating magnetic sublattices. The magnetization of the sublattices is oriented antiparallel, however, their magnitude is not equal. As a result, the magnetic moments do not cancel out and leave a net magnetization.

The sublattices will usually have a different temperature dependence of spontaneous magnetization. In the case of one sublattice dominating the net magnetization at high temperatures and the other at low temperatures, the moments cancel out at a point called *the compensation temperature*. Below this temperature, the net magnetization changes the sign. Ferrimagnets therefore do not follow the simple Curie-Weiss law (1.66) and a modified formula has to be used.

Ferrimagnetism is usually found in ferrites, a family of compounds with the chemical formula $MO{\cdot}Fe_2O_3$ (M = Zn^{2+}, Co^{2+}, Fe^{2+}, Ni^{2+}, Cu^{2+} or Mn^{2+}). [27]. Most ferrimagnets are electrical insulators, which makes them important for high-frequency applications (aerials, transformers), as the energy loss due to the induced eddy currents is minimal compared to metallic ferromagnets.

1.7.4 Spin density waves, non-collinear structures

Thus far, we have mentioned the basic types of magnetic order based on the parallel or antiparallel alignment of spins. However, magnetic structures can be made much more complex due to competing exchange interactions (e.g. RKKY), geometrical frustration or competition between exchange and single ion anisotropies.

Spin density wave is an amplitude-modulated ordered structure - it can be thought of as a collinear alignment of spins, where the magnitude of spins changes periodically with distance, following a sine-wave curve.

Non-collinear magnetic ground states are also possible. This includes *conical*, *cycloidal* and *spiral* magnetic structures, depending on the geometrical shape described by the spins. Although the direction of the spins changes periodically with distance, their magnitude stays constant.

1.8 Frustrated magnetism

In the previous section, various types of conventionally ordered magnetic ground states were shown. In these structures, the dominant exchange interaction (ferromagnetic or antiferromagnetic) is satisfied between all neighbouring spins, resulting in a stable long-range-ordered magnetic ground state. Ín some materials, however, it is impossible to satisfy only one type of exchange between all nearest neighbours. This phenomenon is called *magnetic frustration* and can lead to many exotic magnetic ground states such as *spin glass*, *spin ice* or *spin liquid*.

1.8.1 Magnetic frustration

Magnetic frustration arises from competing exchange interactions between localized magnetic moments (spins), where all interactions cannot be simultaneously satisfied. This results in a large degeneracy of the system ground state, since many spin configurations similar in energy are possible, instead of a single well-defined ground state. The spins then fluctuate between all possible ground states, which prevents any conventional long-range ordering and results in many exotic states of matter. [1]

Typically, magnetic frustration can be induced by the geometry of the crystal lattice. As a simple example, let us consider Ising spins (pointing up or down along a defined axis) with antiferromagnetic interactions ($J_{AF} < 0$) between the

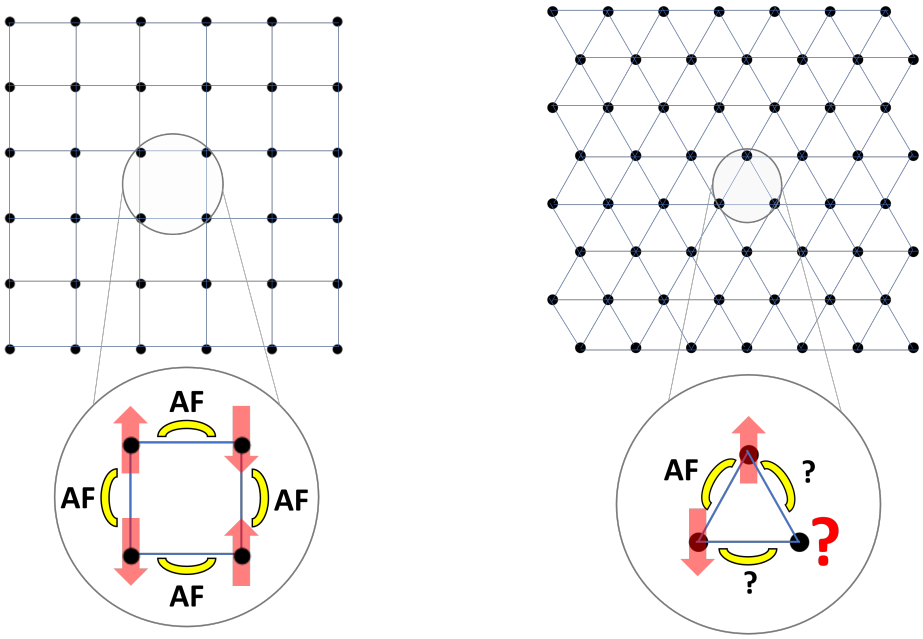

Figure 1.3: A non-frustrated case of Ising spins on the square lattice (left) vs. a frustrated triangular lattice with Ising spins (right).

nearest neighbours. On a 2D square lattice, we are able to find a configuration which satisfies the antiferromagnetic alignment of neighbouring spins. This is not the case in a 2D triangular lattice - if two spins sitting on the vertices of a triangle are antiparallel, it is impossible to place the third spin antiparallel to both neighbouring spins and minimize the system energy (see Figure 1.3). In both possible alignments of the third spin, there will be a competition between ferromagnetic ($J_F > 0$) and antiferromagnetic ($J_{AF} < 0$) interactions with its nearest neighbours, creating a six-fold degeneracy of one triangle. The lattice consists of a large number of these triangles, resulting in a macroscopic multiplicity of metastable states with thermal hysteresis effects.

This is a case of *geometrical frustration*, which usually arises in lattices containing repeating triangular motifs. Besides the aforementioned triangular lattice, the most important types of the so-called *frustrated lattices* are *the kagomé lattice* (a 2D-layered network of vertex-sharing triangles) and *the pyrochlore lattice* (a 3D network of corner-sharing tetrahedra).

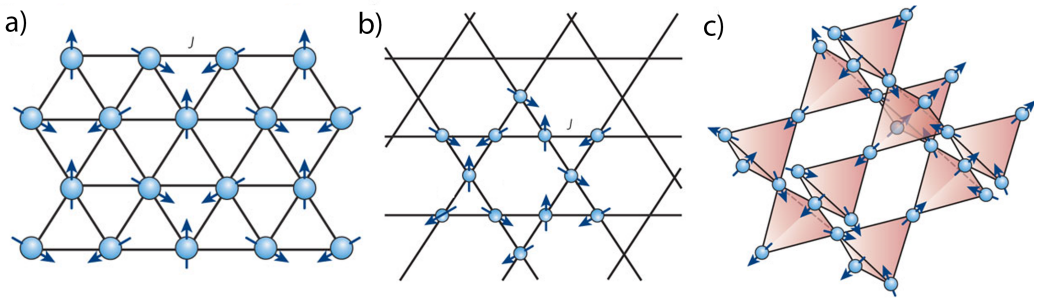

Figure 1.4: a) The triangular lattice. b) The kagome lattice. c) The pyrochlore lattice. Taken from [1] and edited.

1.8.2 Spin glass

The spin-glass phase is defined as a random, disordered magnetic system with mixed interactions, and is characterized by a random but cooperative freezing of spins at a temperature T_f (*the freezing temperature*). Below T_f, there is a highly irreversible, metastable frozen state without any long-range magnetic order. [27]

One source of the spin-glass randomness is *site disorder*, which can be induced by substituting a small amount of magnetic ions into the matrix of a non-magnetic metal (e.g. the spin-glass alloy $Cu_{1-x}Mn_x$, where $x \ll 1$). The magnetic ions are randomly distributed over the lattice, resulting in competing RKKY interactions, the signs of which depend on the mutual (random) distance of spins. Another possibility is *bond disorder*, where the interactions between the nearest neighbours vary between $+J$ and $-J$. This leads to frustration and a multidegenerate ground state.

At high temperatures, the spins in a spin glass can be considered independend as they are dominated by thermal fluctuations. Upon cooling, the spins slow down and start building locally correlated units - *spin clusters*, which can interact with each other through the remaining free spins. As we approach T_f, the interaction of clusters becomes stronger and correlates their local environment. At T_f, the system cooperatively freezes in one of the many possible ground states. Below T_f, the system is in a metastable glassy state, which can be evidenced by the splitting of zero-field-cooled (ZFC) and field-cooled (FC) magnetic susceptibility below T_f.

We can probe the spin dynamics of the freezing process by means of AC susceptibility $\chi^{AC}(\omega) = \chi'(\omega) + i\chi''(\omega)$, which shows a peak in the real part $\chi'(\omega)$ near T_f. The peak is frequency-dependent and shifts slightly with increasing frequency of the alternating field. This shift can be parametrized via *the Vogel-Fulcher law*, which has its origin in describing the temperature dependence of viscosity of supercooled liquids near the glass transition, but is also used to parametrize the spin-freezing process in spin-glass materials [32]:

$$\omega = \omega_0 \exp\left(-\frac{E_a}{k_B(T_f - T_0)}\right) \tag{1.69}$$

where T_0 is "*the ideal glass temperature*", E_a is the activation energy of the transition and ω_0 is the intrinsic relaxation frequency.

1.8.3 Spin liquid

A fluid-like phase of matter induced by magnetic frustration, characterized by long-range correlations of spins which strongly fluctuate down to a temperature of absolute zero and prevent any long-range ordering, is called a *spin liquid*. [1]

Depending on the type of spin fluctuations, there exist *classical spin liquids* driven by thermal fluctuations of spins, which are dominant for large spins ($S \gg \frac{1}{2}$); and *quantum spin liquids* (QSL) driven by large quantum fluctuations down to $T = 0$ K, typical for small spins (S comparable to $\frac{1}{2}$), which produce zero-point motions as a result of the Heisenberg uncertainty principle.

The theoretical possibility of QSLs was first proposed by Anderson in 1973 [2], [33], who studied the ground state properties of a triangular $S = \frac{1}{2}$ Heisenberg

antiferromagnet. Due to the large number of possible ground states, the spins fluctuate between these states in a correlated manner, so the spin-liquid materials are also called *cooperative paramagnets*. The high-temperature magnetic susceptibility usually obeys the Curie-Weiss law (1.66), showing $\theta_{\mathrm{CW}} < 0$ for dominant antiferromagnetic interactions. We also define a quantitative measure of the frustration strength, *the frustration index* [1]

$$f = \frac{|\theta_{CW}|}{T_f} \tag{1.70}$$

as a comparation of the mean-field interaction strength $|\theta_{\mathrm{CW}}|$ with the temperature where the system freezes, T_f. The values of $f > 5 - 10$ indicate a strong suppression of magnetic order due to the frustration. In that case, the spin-liquid phase can be found between $T_f < T < |\theta_{\mathrm{CW}}|$. For an ideal QSL, $f \to \infty$ as the spins remain liquid down to $T = 0$ K.

2. Experimental methods

2.1 Sample preparation

In solid state physics, it is an absolute necessity to prepare high-quality, phase-pure crystalline samples to be able to accurately study their physical properties. There is a plethora of methods for the synthesis of inorganic solids (either in polycrystalline or single-crystalline form), the use of which depends on the thermodynamical stability, chemical reactivity and other intrinsic properties of the precursor materials. In this section, we will briefly introduce the techniques used in the synthesis of fluoride-based pyrochlore and kagome compounds, suitable with regards to the hygroscopic and highly-reactive nature of binary fluorides. Whenever possible, single crystals were grown to measure the directional physical properties of these highly frustrated magnetic materials.

2.1.1 Polycrystalline synthesis

2.1.1.1 Solid-state reaction

A simple yet very effective way of preparing polycrystalline solids of desired composition and structure is *the solid-state synthesis*. It can be done by mixing together powdered reactants, thoroughly grinding the powders to homogenize the mix at the scale of individual particles ($\sim$ 1 μm), preferably pressing the mix into pellets to maximize particle contact and heating it in the furnace for an extended period of time to allow for a slow diffusion of ions. [34]

The reaction begins by nucleation of small crystals with the desired stoichiometry and structure in the place of contact of reactant grains. In order to guarantee a stability of the nucleated crystals, there must be a balance between the negative free energy of formation of the desired product and the positive surface energy of the nuclei. This happens if the crystals are appreciably larger than a single unit cell. Oriented nucleation on top of a reactant grain (*the substrate*) is made easier if the substrate and the nucleus share a similar crystal structure. We refer to this as *epitaxy* if the structural similarity is restricted to a planar interface, and *topotaxy* if the similarity extends to three dimensions.

Following the nucleation, the reactant grains are no longer in direct contact and a counter-diffusion of ions begins through the product interface. This solid-state diffusion of ions is very slow and therefore needs heating for long periods of time at elevated temperatures (but below the melting point of the reactants). To further homogenize the product, multiple regrinds are essential to break up the reactant/product interfaces and create new ones. One can also speed up the reaction by adding a small amount of transporting agent to help bring the reactant ions together.

In this work, all materials were synthesized from binary fluorides, which are known to be hygroscopic and also extremely reactive at high temperatures. For this reason, the binary fluorides were always weighed out, ground and in some cases pelletized inside the glovebox with an inert argon atmosphere. The powders/pellets were then sealed in a platinum crucible with a tiny amount of XeF_2,

which acts as a fluorinating agent as it decomposes at high temperatures into Xe and F_2 gas.

2.1.2 Single crystal growth

2.1.2.1 Laser floating zone method

One of the techniques utilized in this work for growing single crystals of pyrochlore fluorides is *the laser floating zone method*. It is a convenient, fast and crucible-free method for producing high-quality crystals with low consumption of precursor materials. This method also allows growing incongruently melting materials, in contrast to other conventional techniques (Czochralski, Bridgman-Stockbarger or Verneuil), and one can even obtain non-equilibrium phases. [35]

The laser furnace used for our growth (Crystal Systems Corp. FZ-LD-5-200W-II-VPO-PC) consists of 5 symmetrically-placed laser diode units (max. output power 5 × 200 W), which produce infra-red beams of radiation (λ = 900 - 1100 nm). The laser beams are symmetrically focused on a small zone of the sample (laser spot size 4 × 8 mm^2), creating a hot zone with a maximum temperature of 2600 °C. However, the achievable temperature strongly depends on the color of the polycrystalline precursor, hence a material-dependent *emmisivity* parameter has to be employed for the pyrometer to determine the approximate temperature. The molten zone is then moved along the sample length by pulling the upper and lower shaft in a controlled manner (0.1 - 100 mm/hr). Further homogenization of the hot zone temperature profile is reached by rotating the shafts (up to 100 RPM). The sample chamber is separated by a quartz tube, which is highly transparent to IR radiation. The growth can take place in an evacuated (down to 10^{-5} mbar) or pressurized (10 bar) environment in air, oxygen, argon (6N) or even a reducing atmosphere of Ar + 5 % H_2. The gas in the chamber can be held static throughout the growth, but a dynamic flow (up to 2 l/min) is also possible.

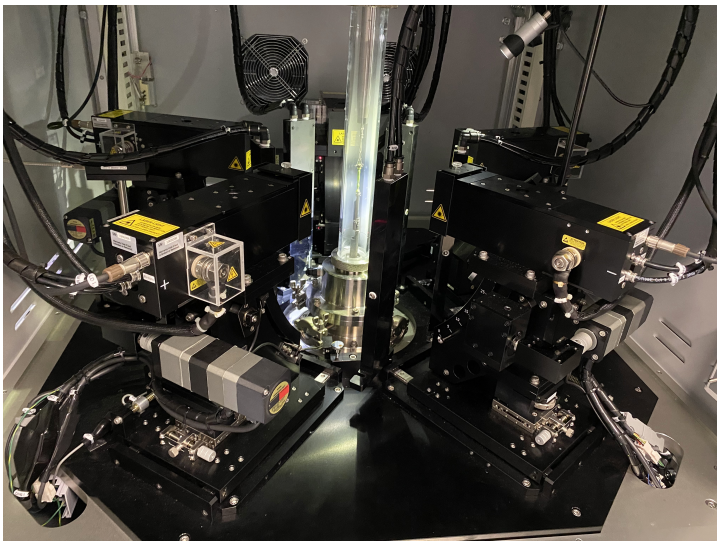

Figure 2.1: Laser floating zone furnace (Crystal Systems Corp. FZ-LD-5-200W-II-VPO-PC)

2.1.2.2 Melt crystallization

Another crystal growth method employed in this work is *melt crystallization*. [36] It is usually performed by placing a ground mix of powdered reactants into a suitable inert crucible, possibly sealing the crucible in an inert atmosphere to prevent any reaction with air and moisture, and heating the crucible inside a furnace above the melting point of the precursor compounds for some period of time to allow the melt to fully react. Crystallization can be achieved by allowing the melt to cool in a slow, controlled manner using a well-defined temperature profile programmed into the furnace.

Similarly to solid-state synthesis, a stoichiometric mix of binary fluorides is first weighed out and ground in a glovebox with an argon atmosphere, preventing any reaction with air moisture. The mix is then filled into a platinum crucible and crimp-sealed inside this protective argon atmosphere. Platinum is a suitable crucible material as it is inert with respect to highly-reactive molten fluorides up to temperatures as high as 1000 °C. [37] The platinum crucible is then inserted into two bigger alumina crucibles with a small portion of calcium oxide (CaO) inside, serving as a precaution against a possible leakage of fluorine or HF gas. The crucibles are then inserted into a programmable resistance furnace with "Kanthal Super" ($MoSi_2$) heating elements capable of temperatures up to 1850 °C. The furnace is situated inside a box with an extraction hood to further minimize any possible leaks of toxic gases. A suitable temperature profile is then programmed and run.

In all our growth attempts or solid-state reactions, the melting temperatures of mixes of binary fluorides are unknown and had to be found by trial and error. We were unable to precisely determine the melting temperatures using the Differential Scanning Calorimetry (DSC) because of the extremely high reactivity of molten fluorides at high temperatures, which attacked the standard alumina crucibles. Suitable DSC platinum crucibles would be needed for a precise determination of the melting temperatures, which unfortunately were not in our possession.

2.2 X-ray diffraction

2.2.1 Laue diffraction

Laue diffraction is a fundamental X-ray diffraction technique, extensively used for orienting and mounting single crystals in a precisely known crystallographic direction. The purpose lies in performing directionally-dependent physical property measurements and/or polishing oriented surfaces. Using this method, it is possible to examine reciprocal space maps of the crystal, also providing evidence of twins, dislocations or defects by analyzing the diffraction pattern. [38]

The Laue diffractometer uses an X-ray source (e.g. a rotating anode tube) to produce polychromatic X-ray radiation by emitting electrons from an electrically heated cathode and accelerating them towards the anode by applying high voltage (20 - 60 kV). Upon the impact, the electrons rapidly decelerate and convert their kinetic energy to produce continuous X-rays (*bremmstrahlung*), but discrete X-rays are also produced by the electronic transitions induced inside the anode material (*characteristic X-rays*).

The single crystal is mounted on a goniometer, using which it is possible to change the crystal's spatial orientation for reorientation between inspection of the reciprocal space maps. The polychromatic X-ray beam passes through the collimator and hits the stationary single crystal. If we assume elastic scattering of the polychromatic beam on atomic chains along three different axes with periodicities $\boldsymbol{a}$, $\boldsymbol{b}$ and $\boldsymbol{c}$, the diffraction conditions can be summed up by *the Laue equations* [39]:

$$\boldsymbol{a} \cdot (\boldsymbol{s} - \boldsymbol{s_0}) = h\lambda \tag{2.1}$$

$$\boldsymbol{b} \cdot (\boldsymbol{s} - \boldsymbol{s_0}) = k\lambda \tag{2.2}$$

$$\boldsymbol{c} \cdot (\boldsymbol{s} - \boldsymbol{s_0}) = l\lambda \tag{2.3}$$

which imply that the constructive interference of the scattered waves (with a particular wavelength λ from the continuous spectrum) happens only if the phase difference between the scattered and the incident wave (with unit vectors $\boldsymbol{s}$ and $\boldsymbol{s_0}$) is equal to an integer multiple h, k, l of the wavelength.

Each of these equations defines a conical surface of possible diffractions, the axis of which lies along the corresponding atomic chain. Since these conditions have to be met simultaneously, the diffraction only happens at the intersection of the three conical surfaces. Laue equations are met when the diffraction vector $\boldsymbol{q} = (\boldsymbol{s} - \boldsymbol{s_0})/\lambda$ (a reciprocal space vector measured in m^{-1}) is equal to a reciprocal lattice vector $\boldsymbol{G}_{\mathrm{hkl}}$ corresponding to a set of planes with Miller indices (hkl):

$$\frac{\boldsymbol{s} - \boldsymbol{s_0}}{\lambda} = \boldsymbol{G}_{\mathrm{hkl}} \tag{2.4}$$

For all λ in the continuous spectrum, many (hkl) reflections fulfill the Laue conditions and are registered on the detector as diffraction spots.

The Laue diffraction pattern is examined for showing the symmetry of the crystal, which depends on the crystal's orientation. If there is a high symmetry direction of the crystal parallel to the incident beam, a matching symmetry is seen in the diffraction pattern. For instance, if we direct the beam along the (100), (110) or (111) direction in a crystal with cubic symmetry, a four-fold, two-fold or three-fold rotational symmetry will be seen in the diffraction pattern, respectively.

In our work, orienting of the crystals was carried out using a PhotoScience Laue diffractometer.

2.2.2 Powder diffraction

Powder X-Ray Diffraction (PXRD) is an important analytical technique used for the structural characterisation of powdered crystalline compounds from their diffraction pattern. Using this method, we are able to perform a crystallographic structural analysis, phase identification and unit cell calculations to determine or refine the crystal structure and the lattice parameters of the studied single- or multi-phase material. [38]

PXRD analysis requires a coherent beam of monochromatic X-rays, which are generated by an appropriate X-ray tube. Discrete characteristic X-rays and continuous bremmstrahlung are produced upon the interaction of electrons with

the metallic anode, as described in the previous section. The full X-ray spectrum is further processed by a filter or a suitable monochromator to provide a monochromatic beam. Common X-ray tube anodes are made of Cu (K_α = 1.54 Å), Cr (K_α = 2.29 Å), Fe (K_α = 1.94 Å), Co (K_α = 1.79 Å) or Mo (K_α = 0.71 Å). Although $K_{\alpha 1}$ ($2p_{3/2} \rightarrow 1s_{1/2}$), $K_{\alpha 2}$ ($2p_{1/2} \rightarrow 1s_{1/2}$) and $K_{\beta 1}$ ($3p_{3/2} \rightarrow 1s_{1/2}$) are the highest-energy X-rays produced, only the K_α lines are generally used in the XRD analysis. If a Cu anode is used, Cu K_β is removed by a nickel-foil filter, which has an absorption edge between the K_α and K_β lines.

The sample is crushed into a fine powder, such that the crystallite size is ideally less than 10 μm, and is placed in the sample holder. In the *symmetric Bragg-Brentano geometry*, the monochromatic beam hits the sample at an angle θ and only diffracts off of grains with lattice planes oriented parallel with the surface. Since we have a fine powder consisting of many randomly oriented crystallites and a fixed wavelength λ, the Bragg's condition [39]

$$2d_{\mathrm{hkl}} \sin \theta_{\mathrm{hkl}} = \lambda \tag{2.5}$$

will be met by some interplanar distance d_{hkl} (corresponding to the Miller indices hkl) for a particular θ_{hkl}. The diffracted beam then reaches the detector at an angle 2θ and is recorded in units of *cps* (counts per second).

The intensity of diffracted light is recorded as a function of the diffraction angle 2θ, producing a diffraction pattern with intensity peaks (also called reflections), which correspond to the diffraction off the atomic planes (hkl). The X-ray tube inside a "$\omega - 2\theta$" (or θ - 2θ) automated XRD diffractometer is usually stationary and illuminates the sample on the goniometer, which rotates at a constant angular speed ω, while the detector moves at 2ω as a result of the system's geometry.

The powder diffraction pattern contains a lot of important information about the microstructure of the examined material, which can be extracted by a structural refinement. The positions of reflections 2θ give information about the symmetry of the crystal lattice (the lattice parameters, as well as information about the symmetry due to systematic absences), and also information about the present phases, each of which has a typical set of reflections corresponding to its crystal structure. The integral intensity of the reflections gives information about the electron density distribution within the unit cell, i.e. the atomic arrangement. It is also proportional to the volume of diffracting crystallites and therefore gives information about their preferential orientation and the abundance of present phases. Thermal *Debye-Waller factors* are also introduced to account for the decrease in integral intensity because of the atomic thermal motion. The width of the peaks (FWHM, integral breadth) provides information about the size of diffracting crystallites, as well as microscopic stress and defects (e.g. dislocations).

In this work, PXRD analysis was performed using a Bruker D8 Advance diffractometer with Cu K_α radiation (λ = 1.5418 Å). The diffraction patterns were analysed using *the Rietveld refinement* [40], which utilizes the least squares method to minimize the difference between the experimental and model diffraction pattern, refining the structural parameters of the input crystal structures. All refinements were performed in TOPAS Academic v6 software [41] (see Attachment A.3). Peak shapes were modelled using the Thompson-Cox-Hastings (THCZ) pseudo-Voigt profile function convoluted with axial divergence asymmetry. The background was fitted with a 6-coefficient polynomial function. Refined

parameters include zero corrections, scaling factors, peak shape parameters, cell parameters, atomic positional coordinates and isotropic thermal parameters B_{eq}.

2.3 Magnetization

2.3.1 DC susceptibility

Temperature-dependent magnetization $M(T)$ measurements in a constant field H (later converted to DC susceptibility as $\chi = M/H$, see (1.19)), as well as field-dependent magnetization curves $M(H)$ at constant T, were performed on both oriented crystals and polycrystalline samples using a SQUID (Superconducting Quantum Interference Device) magnetometer inside a Quantum Design Magnetic Property Measurement System (model MPMS-XL 7T). The sample magnetization was extracted using the Reciprocating Sample Option (RSO) mode.

SQUID magnetometry is one of the most sensitive magnetometry techniques, allowing to measure magnetic moments down to 10^{-8} emu (10^{-11} Am^2) or less. It relies on a special device called *a Josephson junction* [26] - a ring of superconducting metal with one (RF SQUID) or two (DC SQUID) weak links made of a thin insulating barrier. Inside this link, a quantum interference of Cooper pair wavefunctions occurs (electron pairs weakly coupled by the electron-phonon interaction, responsible for the conventional BCS superconductivity). In the DC SQUID, a DC current is applied and the sample is oscillated through the ring, influencing the critical current and causing quasi-static flux variations. In the RF (radio-frequency) SQUID, variation of magnetic flux inside the ring causes a change of impedance, detuning a weakly coupled resonator circuit driven by a RF current.

The RSO option measures the magnetic moment by rapidly oscillating the sample through the SQUID pickup coils in a sinusoidal manner by using a servo motor, as opposed to the DC extraction mode, which moves the sample through the coils in discrete steps. The absolute sensitivity of the RSO mode is given as 1×10^{-8} emu in fields of 0 - 2.5 T. [42]

The temperature-dependent magnetization curves were measured in two modes: the zero-field-cooled (ZFC) and field-cooled (FC) mode. In the ZFC regime, the sample is first cooled down to the lowest measuring temperature (well below its transition temperature) and only then, a desired field is applied and the measurement is run on heating. After the ZFC measurement finishes, the sample is cooled back down to the starting temperature, while the field is still kept at the same value. The FC measurement is then performed on heating. Materials with history dependence, such as magnetically ordered states or spin glasses, will show a splitting of the ZFC and FC curves below the transition temperature (the ordering temperature T_C or the freezing temperature T_f).

2.3.2 AC susceptibility

Temperature, frequency and field dependent AC susceptibility measurements were made using the ACMS II option in a Quantum Design Physical Property Measurement System (PPMS).

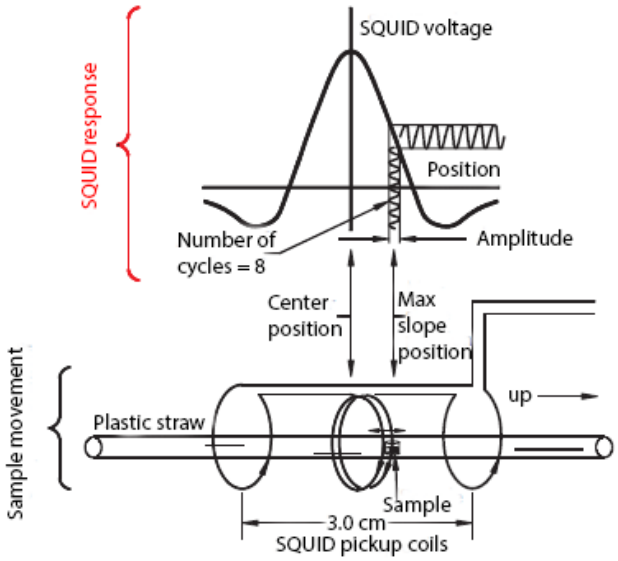

Figure 2.2: RSO measurement with a small amplitude. Taken from [42]

AC magnetometry is a useful technique to probe the spin dynamics of various magnetic systems. As opposed to DC magnetometry, where a constant DC field is applied to determine the equilibrium magnetic moment of the sample, a small driving AC field is superimposed on the DC field, producing a time-dependent magnetic moment. As a result, the changing magnetic moment induces a current in the detection coils without the need of oscillating the sample. [43]

At very low AC frequencies, the sample follows the same $M(H)$ curve as measured in the DC measurement. Provided that the alternating field is small, the induced AC moment can be expressed as

$$M_{AC} = \left(\frac{dM}{dH}\right) H_{AC} \sin(\omega t) \tag{2.6}$$

where $\chi = dM/dH$ is the susceptibility (the slope of the $M(H)$ curve), H_{AC} is the AC field amplitude and $\omega = 2\pi\nu$ is the driving frequency. AC susceptibility is therefore sensitive to very small changes in $M(H)$, as it is related to the slope and not the absolute values.

At higher AC frequencies, dynamic effects in the sample start to manifest and the magnetization starts lagging behind the driving field, not following the DC magnetization curve. The resulting AC susceptibility $\chi(\omega)$ can be thought of as consisting of a real, in-phase component $\chi'(\omega)$ and an imaginary, phase-shifted component $\chi''(\omega)$ defined as

$$\chi(\omega) = \chi'(\omega) + i\chi''(\omega) \tag{2.7}$$

$$\chi' = \chi \cos\phi, \quad \chi'' = \chi \sin\phi \tag{2.8}$$

$$\chi = \sqrt{\chi'^2 + \chi''^2}, \quad \phi = \arctan\left(\frac{\chi''}{\chi'}\right) \tag{2.9}$$

where ϕ is the phase shift with respect to the driving signal. The imaginary component χ'' signals the energy dissipation during the relaxation processes.

In spin-glass materials, we can determine the freezing temperature T_f from the center of the cusp seen in the temperature dependence of the real part, $\chi'(T)$.

The position of the cusp is dependent on the AC-field frequency and can be characterized by a relative shift of T_f per decade of frequency [32]

$$\delta T_f = \frac{\Delta T_f}{T_f \Delta log_{10}\nu} \tag{2.10}$$

the magnitude of which is characteristic for a certain class of materials (canonical spin-glasses, cluster-glasses and superparamagnets).

Further characterization of spin glasses is done by the Vogel-Fulcher law (1.69) by performing a linear fit of T_f vs. $1/\ln(\tau_0\nu)$ in the form

$$T_f = T_0 - \frac{E_a}{k_B}\frac{1}{\ln(\tau_0\nu)} \tag{2.11}$$

where $\tau_0 = 2\pi/\omega_0$ is the intrinsic relaxation time and $\nu = \omega/2\pi$ is the drive field frequency.

2.4 Specific heat

The thermodynamic properties of materials can be accessed through measuring their heat capacity, defined as the amount of heat that needs to be supplied to the material to change its temperature by 1 Kelvin. At constant volume V,

$$C_V = \left(\frac{\delta Q}{dT}\right)_V = \left(\frac{dU}{dT}\right)_V = T\left(\frac{dS}{dT}\right)_V \tag{2.12}$$

where $dU = \delta Q + dW$ is the change of the system's internal energy (the 1st law of thermodynamics) and $\delta Q = TdS$ is an infinitesimal heat given to the system with temperature T, causing a change in entropy dS (the 2nd law of thermodynamics). The experimental value is, however, usually measured at constant pressure, allowing for thermal expansion of the material (extra work $dW = -pdV$ has to be done), always resulting in $C_p > C_V$. At low temperatures, the difference is small and we can assume $C_p \approx C_V$. Specific heat is then defined as the heat capacity per one mole (or unit mass) of the material.

By measuring the specific heat of solids, we are able to probe their lattice, electronic and magnetic properties. Every component of the system (electrons, phonons, magnons, crystal field excitations, phase transitions, etc.) contributes to the total entropy of the system. From the additivity of entropy follows the additivity of specific heat (see (2.12)):

$$S_{tot} = S_e + S_{ph} + S_{mag} + S_{etc} \quad \rightarrow \quad C_{tot} = C_e + C_{ph} + C_{mag} + C_{etc} \tag{2.13}$$

In this work, we restrict ourselves to insulating magnetic materials, so the low-temperature Sommerfeld term $C_e = \gamma T$ [30] corresponding to the specific heat from conduction electrons can be ignored.

By measuring the specific heat of a non-magnetic analogue - an appropriate non-magnetic material with the same crystal structure as the material of interest, we can estimate the phonon contribution from lattice vibrations and subtract it to estimate the magnetic specific heat, C_{mag}. The magnetic entropy is then given by

$$S_{mag}(T) = \int_0^T \frac{C_{mag}(T')}{T'} dT' + S_0 \tag{2.14}$$

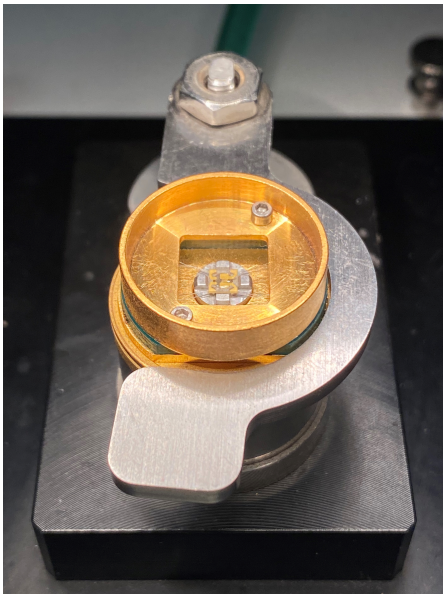

Figure 2.3: PPMS calorimeter puck on a sample-mounting station with vacuum suction holding the sapphire stage without applying stress to the eight electrical wires. [44]

where S_0 is *the residual entropy*, an integration constant corresponding to the entropy at $T = 0$ K (the 3rd law of thermodynamics). It is equal to zero if a unique ground state is present, but is non-zero in the case of magnetically frustrated systems.

We can compare this experimental value with a theoretically predicted entropy of a magnetic ion with a total angular momentum J inside a crystal field generated by the surrounding ions. In the high temperature limit, the probability of populating all energy levels is equal. This gives the magnetic entropy per one mole $S_{mag} = \mathrm{R}\ \ln(\Omega)$, where R is the universal gas constant and Ω is the multiplicity of energy levels. In the isotropic Heisenberg model $\Omega = 2J + 1$, whereas in the Ising model $\Omega = 2$, corresponding to a doublet ground state:

$$S_{mag}^{\mathrm{Heisenberg}} = R\ \ln(2J+1) \quad \text{and} \quad S_{mag}^{\mathrm{Ising}} = R\ \ln 2 \tag{2.15}$$

In the present work, specific heat was measured via the heat relaxation method (the "two-tau model"), using the Heat Capacity option in the Quantum Design Physical Property Measurement System (PPMS). [44] A calorimeter puck with a non-magnetic sapphire stage was used, with Apiezon-N grease for mounting the sample.

3. Materials review

3.1 $A_2B_2O_7$ pyrochlore oxides

Among the most extensively studied pyrochlores, a family of materials isostructural to the naturally occuring mineral pyrochlore $(Na,Ca)_2(Nb,Ta)_2O_6(F,OH)$, are *pyrochlore oxides* with the general formula $A_2B_2O_7$. [45] Typically, A is a 3^+ rare-earth ion and B is a 4^+ transition metal ion, but $A_2^{2+}B_2^{5+}O_7$ and off-stoichiometric pyrochlores also exist. Both A and B sites make up two separate interpenetrating sublattices of corner-sharing tetrahedra. Considering that either A, B or both ions can be magnetic, large geometrical frustration arises due to the nearest-neighbor antiferromagnetic exchange interactions on the pyrochlore lattice, producing a myriad of exotic magnetic ground states. [4]

Table 3.1: Structural details of $A_2B_2O_7$ pyrochlores

$A_2B_2O_6O'$ pyrochlores - S.G.: $Fd\bar{3}m$ (#227, origin 2), cubic, $Z = 8$					
Atom	Wyckoff site	Occupancy	Point group	x, y, z	Charge
A	16d	1.0	$\bar{3}$m (D_{3d})	$\frac{1}{2}, \frac{1}{2}, \frac{1}{2}$	+3 or +2
B	16c	1.0	$\bar{3}$m (D_{3d})	0, 0, 0	+4 or +5
O	48f	1.0	mm (C_{2v})	$x, \frac{1}{8}, \frac{1}{8}$	-2
O$'$	8b	1.0	$\bar{4}$3m (T_d)	$\frac{3}{8}, \frac{3}{8}, \frac{3}{8}$	-2

Pyrochlore oxides crystallize in the face-centered cubic system with the space group $Fd\bar{3}m$ (#227), with four non-equivalent atomic positions and eight formula units per unit cell ($Z = 8$), see Table 3.1. The A site is 8-fold (dodecahedrally) coordinated, while the B site is 6-fold (octahedrally) coordinated by oxygen atoms, as shown in Figure 3.4. Based on more than 180 $A_2B_2O_7$-type compounds, a structural tolerance factor $\tau = 3(R_A + R_O)/(\sqrt{17}(R_B + R_O))$ was developed on the basis of polyhedral geometry dictated by the ionic radii, predicting the pyrochlore phase stability for compounds in range $\tau \in [0.826, 0.943]$. [16]

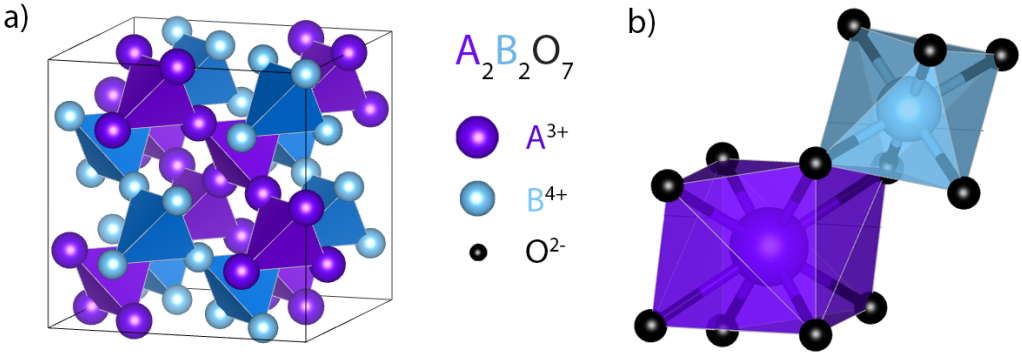

Figure 3.1: a) A (purple) and B (blue) site sublattices of corner-sharing tetrahedra in $A_2B_2O_7$ pyrochlores. b) Coordination polyhedra around A and B site ions - dodecahedra and octahedra, respectively.

The interest in pyrochlore oxides was sparked by the 1997 discovery of the spin-ice state in $Ho_2Ti_2O_7$ [46, 47], shortly followed by the alleged spin-liquid

state discovery in $Tb_2Ti_2O_7$ in 1999. [48] Today, a multitude of pyrochlore oxides have been studied [4], showing a variety of magnetic ground states such as long-range-ordered [49, 50, 51], spin glass [52, 53, 54], spin ice [55, 56, 57] and spin liquid candidates [58, 59, 60]. These ground states seem to be very fragile, as shown by experiments in extreme applied pressures [61], high magnetic fields [62], off-stoichiometry compositions [63] and thin epitaxial films [64].

The variety of properties seen in the rare-earth pyrochlores often comes about due to the enhanced importance of crystal-electric field splitting in $4f$ electron magnetism, that can change the isotropy of the magnetic interaction from Heisenberg [65] (3D isotropic) to XY-type [66] (2D isotropic interaction, usually inside the plane perpendicular to the local <111> axis) to Ising [67] (1D interaction constrained to a specific crystallographic direction, usually the local <111> axis). The contracted nature of the $4f$ orbitals typically leads to low orbital overlap and weak magnetic exchange interactions ($J \sim 10^0 - 10^1$ K), requiring extremely low temperatures (well below 1 K) to reach the most interesting properties and physics.

3.2 $AA'B_2F_7$ pyrochlore fluorides

Since the correlated ground states of the weakly-interacting rare-earth-based pyrochlore oxides can only be accessed at very low temperatures, the implementation of magnetic $3d$ transition metals with stronger exchange interactions ($J \sim 10^2 - 10^3$ K) is essential to make the exotic phenomena more accessible. However, it is extremely difficult to use the late $3d$ metal ions (Mn - Cu) on either A or B sites in the $A_2B_2O_7$ pyrochlores due to the problems with charge neutrality and the structural tolerance factor. [16]

To solve this problem, the divalent oxygen O^{2-} is replaced by a monovalent fluorine F^{-1}, allowing for the creation of $(A_2)^{3+}B_2^{2+}F_7^{-1}$ pyrochlore fluorides with magnetic $B = Mn^{2+}$, Fe^{2+}, Co^{2+}, Ni^{2+} and Cu^{2+} ions, where the exchange interactions are mediated by superexchange through fluoride ligands. The overall electrical neutrality, however, results in a potential issue - an effective 1.5^+ valence state on the A site. As a result, chemical disorder is introduced on the A site, shared between a monovalent A^+ ion and a divalent A'^{2+} ion randomly distributed over the A sublattice. This brings us to $A^+A'^{2+}B_2^{2+}F_7^{1-}$ pyrochlore fluorides, where in the so-far-studied compounds $A = Na^+$ is an alkali metal and $A' = Ca^{2+}$, Sr^{2+} are alkaline earths. [68]

Table 3.2: Structural details of $AA'B_2F_7$ pyrochlores

$AA'B_2F_6F'$ pyrochlores - S.G.: $Fd\bar{3}m$ (#227, origin 2), cubic, $Z = 8$					
Atom	Wyckoff site	Occupancy	Point group	x, y, z	Charge
A/A'	$16d$	0.5/0.5	$\bar{3}$m (D_{3d})	$\frac{1}{2}, \frac{1}{2}, \frac{1}{2}$	1+/2+
B	$16c$	1.0	$\bar{3}$m (D_{3d})	0, 0, 0	2+
F	$48f$	1.0	mm (C_{2v})	x, $\frac{1}{8}, \frac{1}{8}$	1-
F'	$8b$	1.0	$\bar{4}$3m (T_d)	$\frac{3}{8}, \frac{3}{8}, \frac{3}{8}$	1-

Pyrochlore fluorides share the same cubic $Fd\bar{3}m$ crystal structure with 8 formula units per unit cell as pyrochlore oxides, see Table 3.2. The main difference

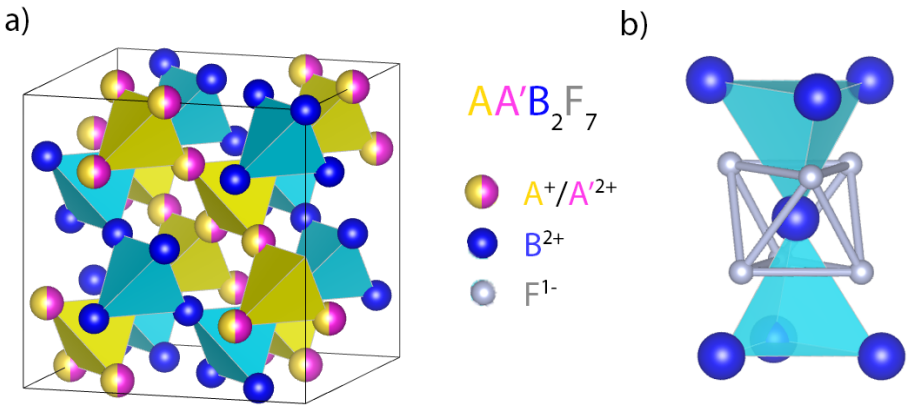

Figure 3.2: a) A/A' (yellow/pink) and B (blue) site sublattices of corner-sharing tetrahedra in $AA'B_2F_7$ pyrochlores. b) Octahedrally coordinated B site by fluorine atoms.

is the randomly occupied A site by A^+ and A'^{2+} ions, each with a 50% occupancy. The only free structural parameter, the x coordinate of the fluorine ions on the $48f$ site dictates the geometry of the coordination polyhedra of A and B site ions. If $x = 0.3125$, the fluorine ions create an ideal BF_6 octahedron around the B site, while for $x = 0.375$ an ideal AF_8 cube of fluorine ions surrounds the A site [45, 69], see Figure 3.3. For $x > 0.3125$, the BF_6 octahedra are compressed along the local <111> axis with two different F-Co-F bond angles, differing from the ideal 90° value. [10] Since the magnetic ions reside on the B site, the geometry of the coordination octahedra influences the magnetism of pyrochlore fluorides, as the superexchange pathways are dictated by the Co-F-Co bond angles, while the position of the coordinating fluorine ions also determines the size and effect of the crystal field on the magnetic B ion.

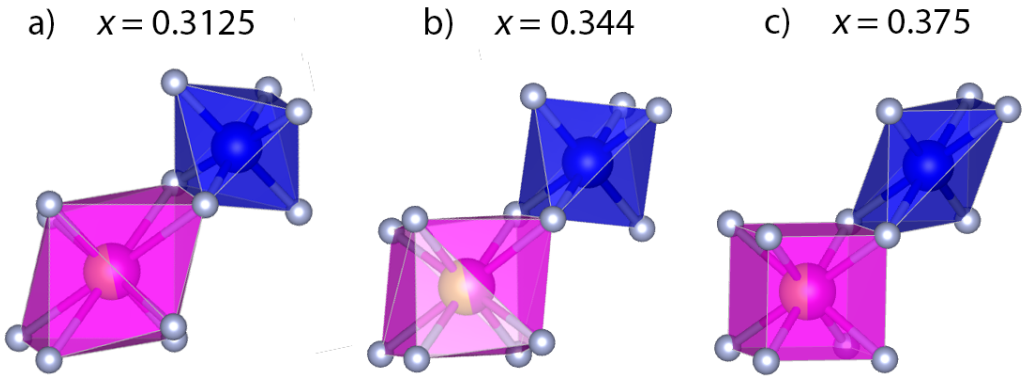

Figure 3.3: Coordination polyhedra - AF_8 (pink dodecahedron) and BF_6 (blue octahedron) as a function of the free parameter x of the $48f$ fluorine site. a) Ideal BF_6 octahedron for $x = 0.3125$. b) AF_8 dodecahedron around A and a distorted octahedron around B for $0.3125 < x < 0.375$. c) Ideal AF_8 cube for $x = 0.375$.

Crystallographic studies on polycrystalline pyrochlore fluorides were first performed in 1970 [9], but it was not until 2014 when first magnetic studies appeared on $NaCaCo_2F_7$ [10] due to the use of advanced floating zone technique for the growth of large single crystals.

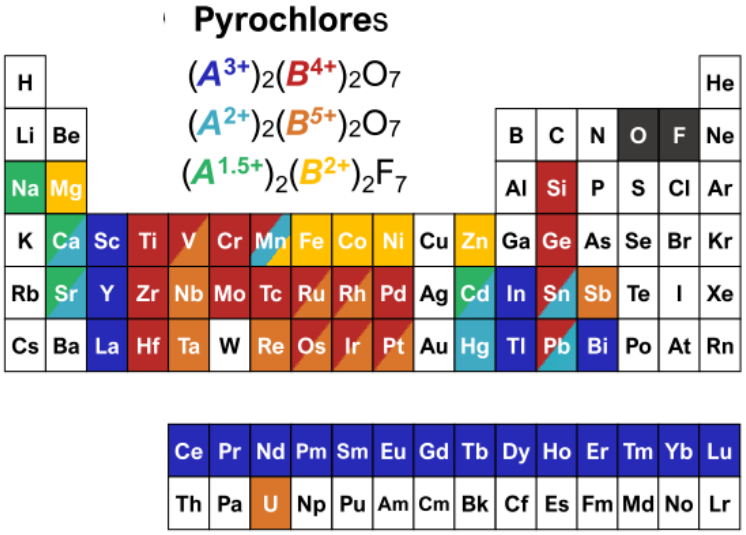

Figure 3.4: Elements known to form pyrochlore oxides and fluorides. Taken from [68].

In all of the so-far-studied $AA'B_2F_7$ materials ($A = Na^+$, $A' = Ca^{2+}$, Sr^{2+} and $B = Mn^{2+}$, Fe^{2+}, Co^{2+}, Ni^{2+}) [10, 11, 12, 13], despite strong antiferromagnetic interactions evidenced by Curie-Weiss temperatures ranging from θ_{CW} = -73 K in $NaCaFe_2F_7$ [13] to -140 K in $NaCaCo_2F_7$ [10], no magnetic order is observed with cooling down to below 4 K, indicating a large magnetic frustration. In all of the studied cases, this frustration is quenched by a spin-freezing transition at a temperature T_f. The spin freezing is believed to originate from the exchange disorder Δ (assuming an average nearest-neighbor exchange interaction J with small fluctuations Δ, such that $\Delta \ll J$), introduced by the chemical disorder on the A site. [70] Theoretical studies show that the magnetic bond disorder in the pyrochlore Heisenberg antiferromagnets can induce a spin-glass transition commensurate with the energy scale of the bond disorder, $k_B T_f = \sqrt{8/3}\Delta$. [71] The glassy nature is evidenced by the bifurcation of ZFC and FC magnetic susceptibility [10, 13]. Indeed, an extensive study of the short range magnetic correlations of $NaA'Co_2F_7$ (A‘ = Sr, Ca) shows frozen XY-like magnetism at low temperature, but with magnetic correlations that persist up to 200 K [14]. A recent investigation of the inelastic neutron excitation spectra of $NaCaNi_2F_7$ found a continuum of scattering with low energy pinch points indicating a correlated spin-liquid character [15].

In recent years, the interesting properties of Co^{2+}-based pyrochlore fluorides $NaA'Co_2F_7$ (A‘ = Ca, Sr) have been extensively studied due to the intriguing magnetism invoked by the octahedral CoF_6 complexes on the pyrochlore lattice. Unlike most of the 3d transition metals where the orbital moment is quenched, when the high spin Co^{2+} ($S = 3/2$) ion is placed in an octahedrally coordinated cubic environment with small tetragonal distortions, the crystal electric field combined with spin-orbit coupling forms a $J_{\text{eff}} = 1/2$ single-ion Kramers doublet groundstate [72]. A strong XY-like anisotropy (evidenced by the g-tensor components $g_{xy}/g_z \sim 3$) has been found in a single-ion energy level study by inelastic

neutron scattering [73]. At sufficiently low temperatures, the $J_{\text{eff}} = 1/2$ Kramers doublet is the only occupied state (indicated by the entropy change approaching the R ln2 limit [10, 11]), making Co^{2+}-based pyrochlores a new promising avenue in the search of a quantum spin liquid. Recent high frequency/high field electron spin resonance investigation of $NaCaCo_2F_7$ revealed two coexisting magnetic phases above a spin-glass freezing temperature ($T_f \sim 2.4$ K) – a cooperative paramagnetic phase characterised by a gapless excitation mode, as well as a spin-glass phase below 20 K with a gapped low-energy excitation. [74] Ultrasound velocity measurements of $NaCaCo_2F_7$ uncovereded elastic anomalies in the bulk modulus and the trigonal shear modulus below 20 K, revealing an enhancement of the exchange disorder (responsible for the spin freezing) due to the spin-lattice coupling, as well as a coupling of the lattice to the dynamical spin-cluster state. [75]

Despite the increasing interest in a number of members of this family, beyond the intial report of a pyrochlore structure compound with formula $NaCdCu_2F_7$ [9], no properties have been reported for any Cu^{2+} containing pyrochlore fluorides, where enhanced quantum fluctuations of the low spins state ($S = 1/2$) Cu^{2+} ion are expected to further destabilise magnetic order, retaining a quantum spin-liquid ground-state. [21]

3.3 $A_3A'M_3M'F_{14}$, $A_2M_3M'F_{12}$ kagome fluorides

The kagome lattice, a 2D layered network of vertex-sharing triangles, is one of the most geometrically frustrated systems. The 2D kagome planes can be isolated within the 3D pyrochlore structure by selectively diluting the pyrochlore lattice with non-magnetic ions in an appropriate, ordered way. This ordered dilution is found in the natural mineral Coulsellite, $Na_3CaMg_3AlF_{14}$ [20] with full 1:3 ordering of Ca:Na on the A sites and Al:Mg on the B sites, but has so far not been reported in any synthetic fluorides.

Table 3.3: Predicted structural details of $A_3A'M_3M'F_{14}$ kagomes (based on $Na_3CaMg_3AlF_{14}$ [20] and standardized in VESTA[76])

$A_3A'M_3M'F_{14}$ kagomes - S.G.: $R\bar{3}m$ (#166, setting 1), rhombohedral, $Z = 3$					
Atom	Wyckoff position	Occupancy	Point group	x, y, z	Charge
A	$9d$	1.0	$.2/m$	$\frac{1}{2}, 0, \frac{1}{2}$	1+
A'	$3a$	1.0	$\bar{3}$m	$0, 0, 0$	2+
M	$9e$	1.0	.2/m	$\frac{1}{2}, 0, 0$	2+
M'	$3b$	1.0	$\bar{3}$m	$0, 0, \frac{1}{2}$	3+
F1	$18h$	1.0	.m	$x+1, -x, z$	1-
F2	$18h$	1.0	.m	$x+1, -x, z$	1-
F3	$6c$	1.0	3m	$0, 0, z$	1-

A series of crystallographically ordered, ideal rare earth 2D kagome compounds have been reported, e.g. the $RE_3Sb_3Zn_2O_{14}$ family (RE = La, Pr, Nd, Sm, Eu, Gd), [77] as well as the magnetic transition-element-based $RE_3Sb_3Mn_2O_{14}$ (RE = La, Pr, and Nd) [78] and $RE_3Sb_3Co_2O_{14}$ (RE = La, Pr, Nd, Sm-Ho) [79],

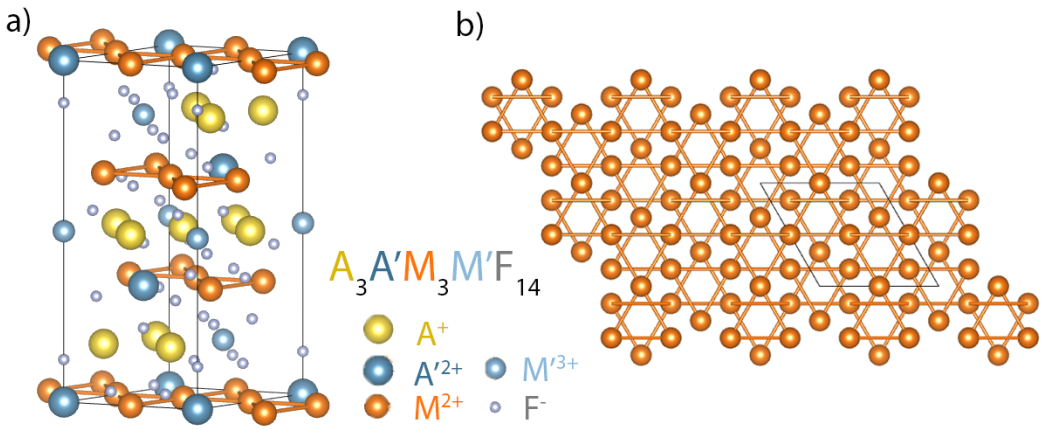

Figure 3.5: a) Predicted unit cell of $A_3A'M_3M'F_{14}$ kagomes (based on $Na_3CaMg_3AlF_{14}$ [20]). b) 2D kagome network of M^{2+} ions viewed along the c axis.

all showing high frustration with strong antiferromagnetic interactions, evidenced by the Curie-Weiss temperatures down to θ_{CW} = -620 K. This motivates us to examine the possibility of synthesizing isostructural fluoride-based $A_3A'M_3M'F_{14}$ kagome compounds, where A is a 1^+ alkali metal, A‘ is a 2^+ alkaline earth, M is a magnetic 2^+ transition metal and M‘ is a non-magnetic 3^+ ion (Al, Ga).

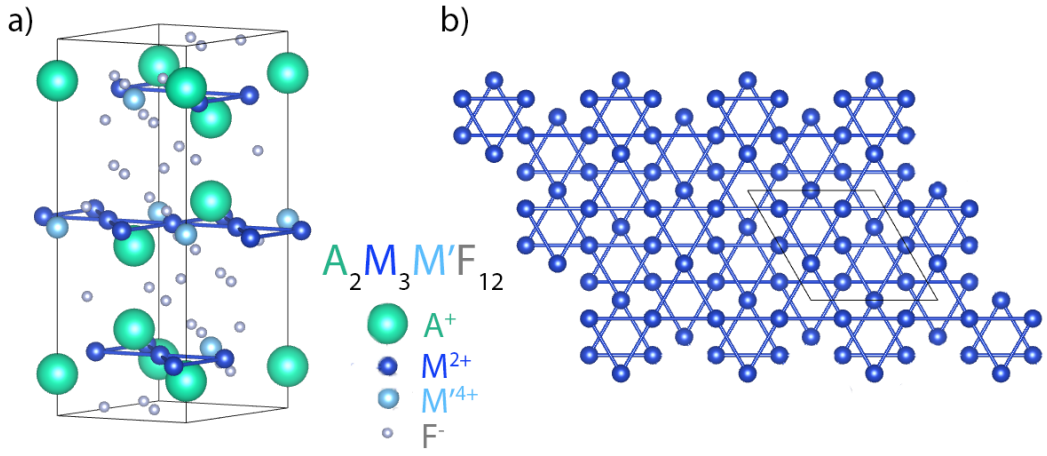

Figure 3.6: a) Predicted unit cell of $A_2M_3M'F_{12}$ kagome fluorides (based on $Cs_2Cu_3TiF_{12}$ [80]). b) 2D kagome network of M^{2+} ions viewed along the c axis.

In fact, some structurally related kagome fluorides have already been successfully synthesised – systems with the composition $A_2Cu_3M'F_{12}$ (A = Rb, Cs; M‘ = Sn, Zr, Hf, Ti) have been studied (see eg. [17, 18, 81, 80]), all based on the $3d$ transition metal Cu^{2+} ($S = 1/2$) ion, aiming to utilize large quantum fluctuations in the $T \to 0$ limit to potentially destabilise magnetic order. However, a symmetry-lowering structural phase transition is seen in these materials (from T_t = 172 K in $Cs_2Cu_3HfF_{12}$ to 225 K in $Cs_2Cu_3ZrF_{12}$) and magnetic ordering occurs from T_N = 20 K ($Cs_2Cu_3HfF_{12}$) to 24.5 K ($Cs_2Cu_3SnF_{12}$), resulting in a small ferromagnetic moment. No Co^{2+}-based analogues have yet been reported,

motivating our research towards synthesizing $A_2Co_3M'F_{12}$ compounds (A = Rb, Cs; M‘ = Sn, Zr, Hf, Ti) with the hope of obtaining a $J_{\text{eff}} = 1/2$ Heisenberg kagome antiferromagnet with a quantum spin liquid groundstate.

Table 3.4: Predicted structural details of $A_2M_3M'F_{12}$ kagomes (based on [80], at room temperature)

$A_2M_3M'F_{12}$ kagomes - S.G.: $R\bar{3}m$ (#166), rhombohedral, $Z = 3$					
Atom	Wyckoff position	Occupancy	Point group	x, y, z	Charge
A	$6c$	1.0	3m	$0, 0, z$	1+
M	$9d$	1.0	.2/m	$\frac{1}{2}, 0, \frac{1}{2}$	2+
M'	$3b$	1.0	$\bar{3}$m	$0, 0, \frac{1}{2}$	4+
F1	$18h$	1.0	.m	$x, -x, z$	1-
F2	$18h$	1.0	.m	$x, -x, z$	1-

4. Results

4.1 NaCdB_2F_7 pyrochlore fluorides

By applying the previously discussed $A_2B_2O_7$ pyrochlore oxide structure tolerance factor τ [16] to the $AA'B_2F_7$ pyrochlore fluorides, we attempted to predict and synthesize new stable pyrochlore fluorides with the composition NaCdB_2F_7 (B = Mn^{2+}, Fe^{2+}, Co^{2+}, Ni^{2+}, Cu^{2+} and Zn^{2+}). The adjusted tolerance factor is

$$\tau = \frac{3(R_A + R_F)}{\sqrt{17}(R_B + R_F)}, \qquad \tau \in [0.826, 0.943] \tag{4.1}$$

where $R_A = \frac{1}{2}(R_{A^+} + R_{A'^{2+}})$ is the effective A-site ionic radius taken as the arithmetic mean of the A^+ and A'^{2+} ionic radii, and R_B and R_F are the ionic radii of the B site ion and fluorine, respectively. The calculation of τ is based on the Shannon ionic radii [82] of elements with a specific coordination number (CN): CN = 8 for the dodecahedrally coordinated A site, CN = 6 for the octahedrally coordinated B site and CN = 4 for the tetrahedrally coordinated $48f$ and $8b$ fluorine sites. The octahedrally coordinated B = Mn, Fe and Co typically take the high-spin configuration, for which the ionic radius is shown.

Table 4.1: Shannon ionic radii [82] for the actual CN of A, B and F sites (CN = 8, 6 and 4, respectively) and Ahrens ionic radii [83] for CN = 6.

ion	Na^+	Cd^{2+}	Mn^{2+}	Fe^{2+}	Co^{2+}	Ni^{2+}	Cu^{2+}	Zn^{2+}	F^{1-}
$R_{Shannon}$ [Å]	1.18	1.10	0.83	0.78	0.745	0.69	0.73	0.74	1.31
R_{Ahrens} [Å]	0.97	0.97	0.80	0.74	0.72	0.69	0.72	0.71	1.33

We are also able to predict the lattice parameter of the cubic $AA'B_2F_7$ pyrochlore fluorides [84], based on the Chakoumakos function [85] in the form $a_{\text{pred}} = MR_A + NR_B + O$, where R_A and R_B are the Ahrens ionic radii [83] of A and B site corresponding to CN = 6 (where $R_A = \frac{1}{2}(R_{A^+} + R_{A'^{2+}})$ is defined as above) and M, N and O are refinable parameters. By applying the multiple linear regression analysis, the best match with the previously-reported compounds [9, 10, 11, 12, 13, 77] was reached with the formula [84]

$$a_{\text{pred}} = 2.846R_A + 2.567R_B + 5.762 \tag{4.2}$$

Applying these formulae, we predict the stability of the pyrochlore structure as well as the lattice parameters for the whole series of compounds with the formula NaCdB_2F_7 (B = Mn^{2+}, Fe^{2+}, Co^{2+}, Ni^{2+}, Cu^{2+}, Zn^{2+}), see Table 4.2.

Table 4.2: Calculated pyrochlore tolerance factor τ (stable in range [0.826, 0.943]) [16] and predicted lattice parameters a_{pred} for NaCdB_2F_7 pyrochlores. [84]

B^{2+} ion	Mn^{2+}	Fe^{2+}	Co^{2+}	Ni^{2+}	Cu^{2+}	Zn^{2+}
τ	0.833	0.853	0.867	0.891	0.874	0.870
a_{pred} [Å]	10.576	10.422	10.371	10.294	10.371	10.345

4.1.1 $NaCdZn_2F_7$

To begin with, we decided to synthesize a non-magnetic Zn^{2+}-based pyrochlore fluoride, $NaCdZn_2F_7$, previously reported in several polycrystalline and single crystal studies. [9, 86, 87, 88] The main purpose of this compound is to be later used as a non-magnetic analogue in the specific heat subtraction of the lattice vibration (phonon) contribution, separating the magnetic specific heat of the magnetic pyrochlores and probing the nature of their ground state by means of magnetic entropy analysis. We were able to successfully synthesize a polycrystalline powder as well as grow single crystals of $NaCdZn_2F_7$.

4.1.1.1 Solid state synthesis, PXRD

A stoichiometric mix ($m = 2$ g) of dry, high-purity binary fluorides was weighed out and ground inside the glovebox with a protective argon atmosphere to prevent any reaction with air moisture. The mix was poured into a platinum crucible along with 30 mg of XeF_2 and crimp-sealed with a pair of pliers, creating a double-fold for a good protection against a possible expansion and leakage of the Pt tube at high temperatures. The Pt tube was then placed inside two enclosing alumina crucibles with a small portion of CaO inside, which would react with fluorine gas in the case of a leakage, preventing a damage of the furnace heating elements. The crucibles were inserted into a programmable furnace with an extraction hood. The furnace was programmed to ramp up to 700 °C at the rate of 2 °C/min, dwell there for 5 days and rapidly cool to room temperature. The intended solid state (marked as the subscript (s)) reaction is described by the following equation:

$$NaF_{(s)} + CdF_{2(s)} + 2\ ZnF_{2(s)} \xrightarrow[5\ \text{days}]{700°C\ \text{in}\ Ar_{(g)}/F_{2(g)}} NaCdZn_2F_{7(s)}$$

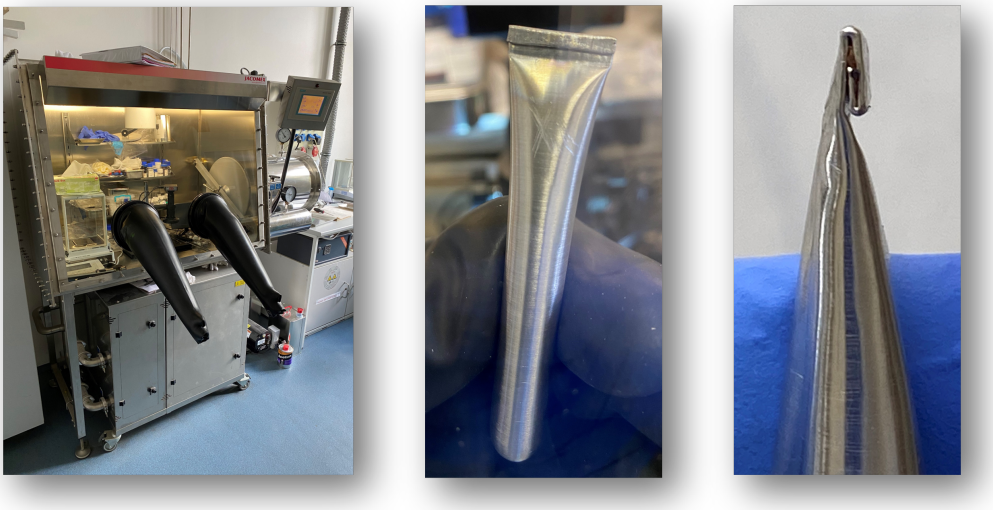

Figure 4.1: Glovebox used for the preparation of the stoichiometric mix (left). Sealed Pt crucible (middle). A close-up view of the double-folded seal (right).

White polycrystalline material was obtained and a small portion was ground for a Powder X-Ray Diffraction measurement. PXRD confirmed a successful synthesis of polycrystalline $NaCdZn_2F_7$ with a 96 wt.% phase fraction, confirming the cubic $Fd\bar{3}m$ structure with the lattice parameter refined to $a = 10.3450(3)$

Å, agreeing perfectly with the predicted value in Table 4.2. However, a 4 wt.% impurity phase was also detected - the fluoperovskite β-$NaZnF_3$ [89] (the low-temperature phase of $NaZnF_3$ existing below 683 °C) with the orthorhombic space group *Pnma* (#62) and refined lattice parameters $a = 5.587(2)$ Å, $b = 7.773(3)$ Å and $c = 5.414(2)$ Å.

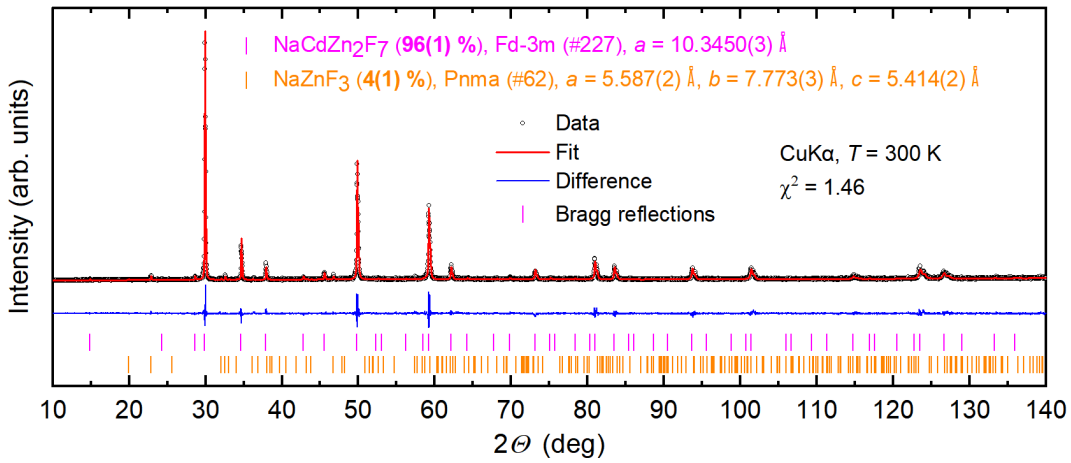

Figure 4.2: PXRD refinement of the solid-state-reacted $NaCdZn_2F_7$ (96 wt.%), revealing a $NaZnF_3$ impurity (4 wt.%).

4.1.1.2 Crystal growth, PXRD

A 4g stoichiometric mix of binary fluorides was prepared in the glovebox and filled into a hollow graphite crucible, which was then installed into the laser floating zone furnace and used for pre-melting into a precursor rod. The pre-melting took place inside a dynamic argon flow of 0.25 l/min at the pressure of 8 bar to minimize evaporation. The graphite was heated at constant 18% power (∼ 1050 °C @ 0.72 emissivity). The hot zone was moved up-down-up along the crucible length at the speed of 100 mm/hr with a 5 RPM rotation to further homogenize the heating. The precursor rod was then broken into two pieces - a seed and a feed rod, which were again installed in the laser furnace for the crystal growth.

The growth was again performed in a dynamic argon flow of 0.25 l/min at 8 bar, this time with 9.2% power (∼ 650 °C @ 0.85 emissivity), 2 mm/hr and 4 mm/hr pulling speed (upper and lower shaft, respectively) and 5 RPM rotation of both shafts. An oligocrystalline ingot was obtained, which was then broken into small single grain segments. A small selection of single crystals were crushed into a fine powder and analyzed by PXRD.

PXRD analysis confirmed a phase-pure $NaCdZn_2F_7$ pyrochlore with a refined parameter $a = 10.3399(3)$ Å and a refined 48*b* site fluorine (F2) x coordinate, $x_{F2} = 0.3268(7)$. A good chi-squared value of the fit was reached, [90] $\chi^2 = 1.13$. The previous room-temperature single crystal diffraction data report slightly higher values, $a = 10.34657(3)$ Å and $x_{F2} = 0.3327(1)$. [86, 87]

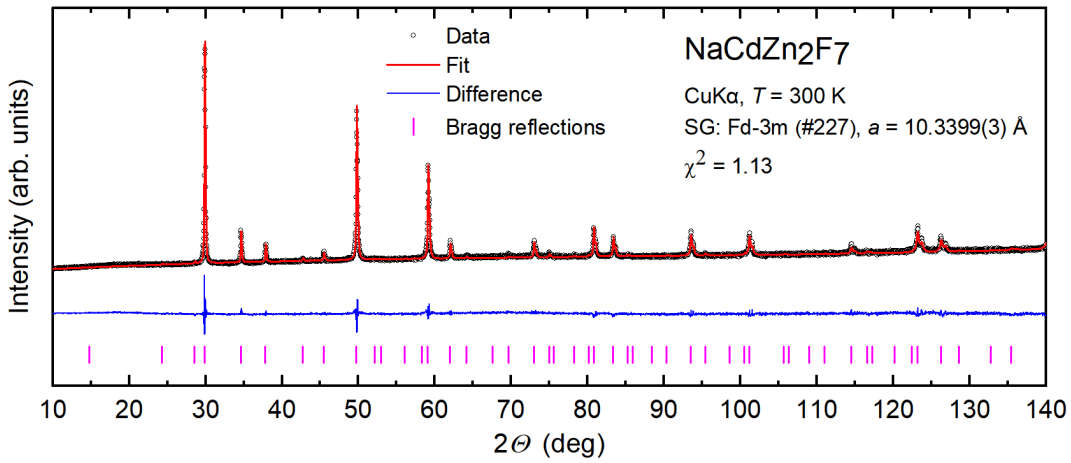

Figure 4.3: PXRD refinement of the powdered $NaCdZn_2F_7$ crystal, grown in the laser floating zone furnace.

4.1.2 $NaCdCo_2F_7$

The first interesting magnetic candidate is the Co^{2+}-based pyrochlore fluoride, $NaCdCo_2F_7$. The previously studied compounds, $NaCaCo_2F_7$ and $NaSrCo_2F_7$ [10, 11], reported a $J_{\text{eff}} = 1/2$ groundstate with XY-type anisotropy [73, 91]. We managed to successfully synthesize a polycrystalline powder and subsequently grow and characterize single crystals of $NaCdCo_2F_7$, allowing for a comparison with the $A' =$ Ca, Sr compounds.

4.1.2.1 Solid state synthesis, PXRD

Similarly to $NaCdZn_2F_7$, 2 grams of the stoichiometric binary-fluoride mix were prepared in the glovebox, filled into a Pt tube with 30 mg of XeF_2, crimp-sealed with a double fold and inserted into the furnace inside two alumina crucibles with CaO. The same heating program was used - ramp up to 700 °C at the rate of 2 °C/min, hold there for 5 days and cool to room temperature:

$$NaF_{(s)} + CdF_{2(s)} + 2\ CoF_{2(s)} \xrightarrow[5\ \text{days}]{700°C\ \text{in}\ Ar_{(g)}/F_{2(g)}} NaCdCo_2F_{7(s)}$$

Dark red polycrystalline material was obtained, a small portion of which was ground and analyzed via PXRD. The $Fd\bar{3}m$ pyrochlore structure of $NaCdCo_2F_7$ (96 wt.% phase fraction) was confirmed with a refined lattice parameter $a =$ 10.3658(1) Å, lower than the predicted value in Table 4.2 by 0.07 %. Two impurity phases were also revealed: 2 wt.% of CoF_2, crystallizing in the tetragonal $P4_2/mnm$ (#136) rutile structure [92] with refined lattice parameters $a =$ 4.7197(5) Å and $c =$ 3.1997(7) Å, and also 2 wt.% of $NaCoF_3$, crystallizing in the orthorhombic $Pbnm$ (#62) perovskite structure [93] with refined lattice parameters $a = 5.480(2)$ Å, $b = 5.611(2)$ Å and $c = 7.797(2)$ Å.

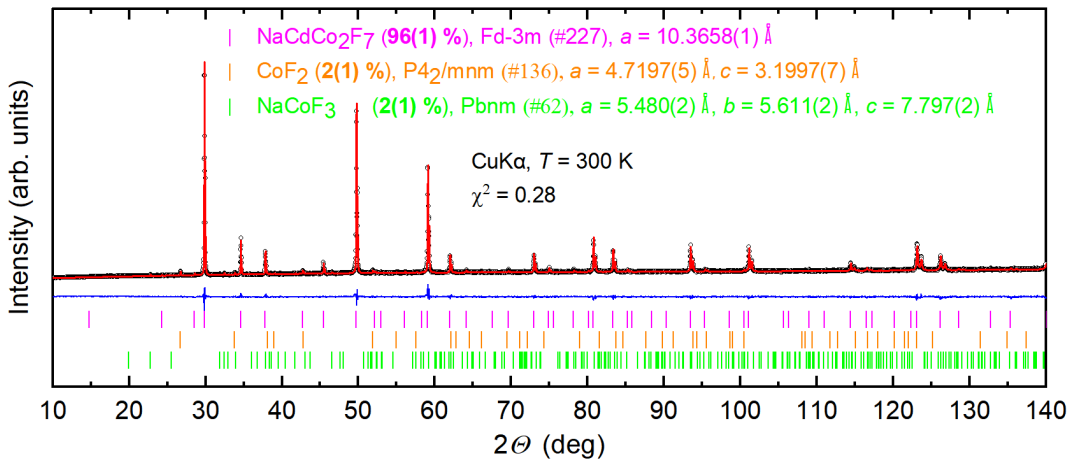

Figure 4.4: PXRD refinement of the polycrystalline $NaCdCo_2F_7$ (96 wt.%) with two impurity phases: CoF_2 (2 wt.%) and $NaCoF_3$ (2 wt.%).

4.1.2.2 Crystal growth, PXRD

Similarly to $NaCdZn_2F_7$, single crystals of $NaCdCo_2F_7$ were grown using the laser floating zone furnace. A 4 gram stoichiometric mix of elemental fluorides was weighed out and ground in the glovebox. The ground powder was then filled into a hollow graphite tubular crucible and melted in the laser furnace under an 8 bar atmosphere of argon, at 16.6 % laser power ($\sim$ 1000 °C at 0.72 emmisivity of graphite), to form a polycrystalline precursor. After cooling, the rod was extracted from the graphite and re-mounted within the furnace for standard floating-zone growth using platinum wire. The growth was again performed under a dynamic flow of argon atmosphere (0.25 l/min) at high pressure (8 bar) to minimize evaporation.

The obtained oligocrystalline ingot was broken into smaller pieces, many of which were single grain fragments. A black layer on the surface of the oligocrystalline ingot was formed due to the pre-melting in the graphite crucible, but did not influence the purity of the crystals in the center. Large multiple-grain crystals appeared to have white/grey impurities formed on the grain boundaries, later identified as CoF_2 by PXRD analysis. These crystals were not used in the measurements, instead small transparent single-grain crystals were picked and oriented on the Laue diffractometer for directional single crystal property measurements.

A small selection of the transparent single-grain crystals were crushed into a fine powder and analyzed by PXRD, which confirmed a phase pure $NaCdCo_2F_7$ pyrochlore with the lattice parameter $a = 10.3636(2)$ Å and the $F(2)$ x-coordinate $x_{F2} = 0.3329(5)$.

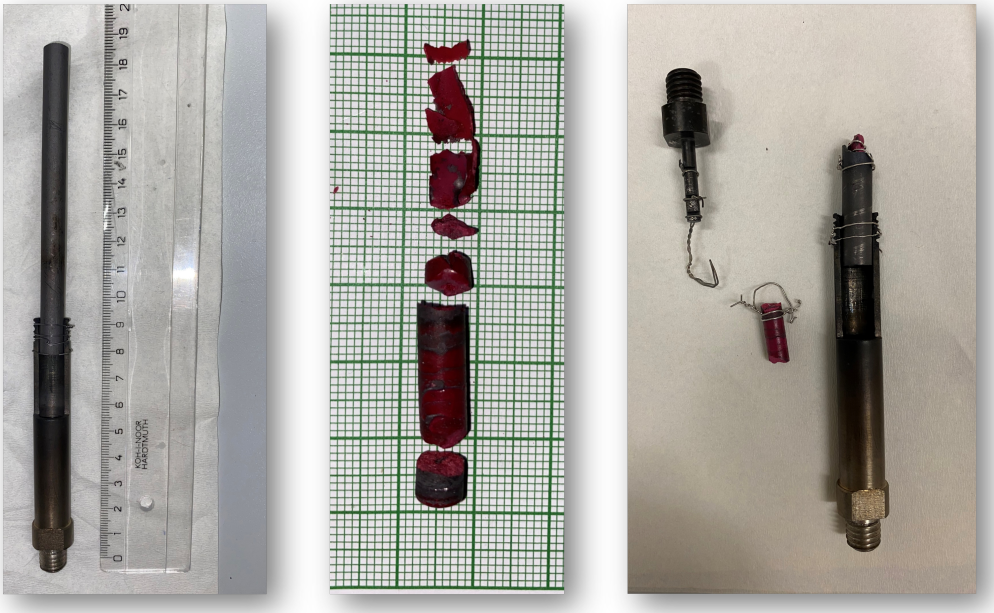

Figure 4.5: Mounted graphite crucible (left). Obtained pre-melted $NaCdCo_2F_7$ rod with a black surface layer from the graphite (middle). A feed rod with a Pt hook and a mounted seed (right).

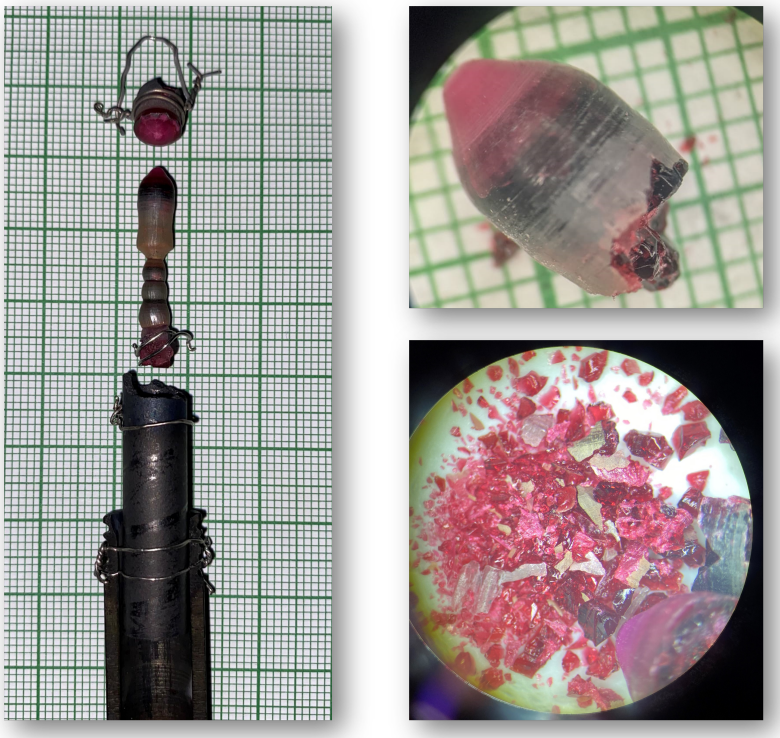

Figure 4.6: Obtained oligocrystalline ingot (left), broken into smaller pieces containing pure transparent single-grain crystals, as well as impure crystals with grey CoF_2 inclusions and/or surface layers. (right)

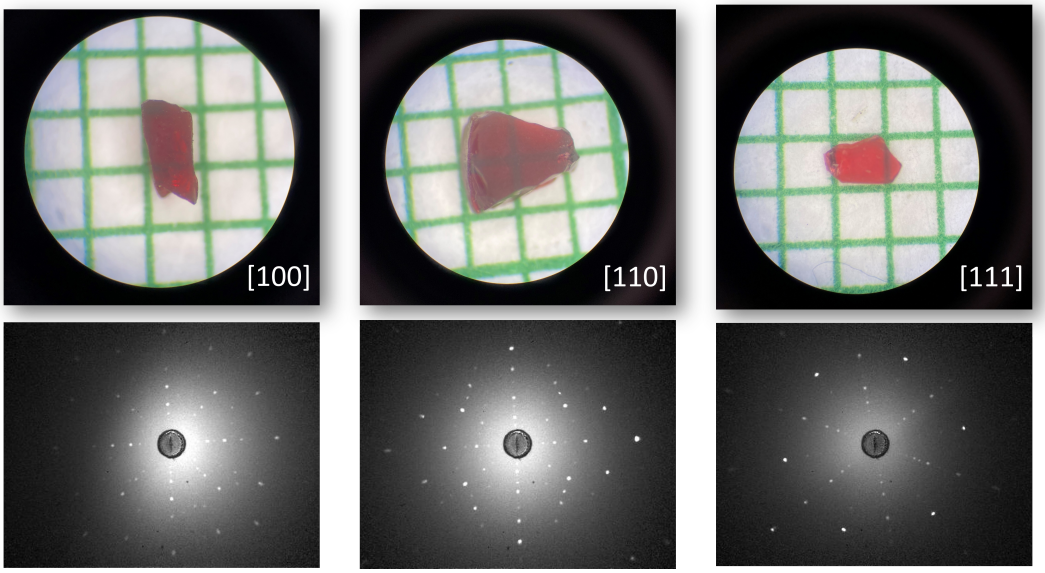

Figure 4.7: $NaCdCo_2F_7$ single crystals oriented along the [100], [110] and [111] directions, used for directional measurements (top). Laue diffraction patterns showing four-fold, two-fold and three-fold rotational symmetry, respectively. (bottom)

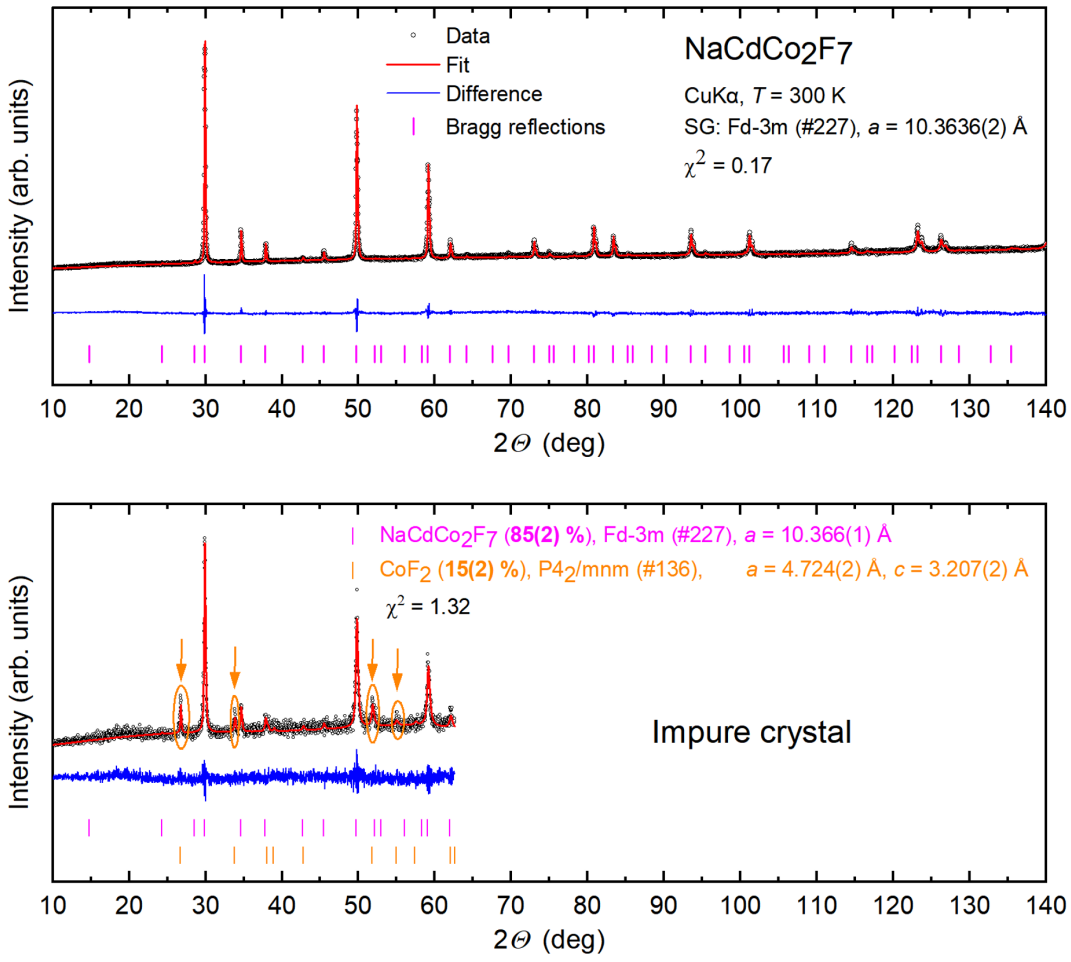

Figure 4.8: PXRD refinement of the powdered transparent $NaCdCo_2F_7$ crystals (top) and crystals containing grey CoF_2 impurities (bottom, stopped at 65°).

4.1.2.3 Single crystal diffraction

Single crystal X-ray diffraction (SCXRD) was performed by a collaborator, Prof. Gerald Giester (Department of Mineralogy and Crystallography, Faculty of Geosciences, Geography and Astronomy, University of Vienna), at room temperature using a Bruker Kappa X8 APEX diffractometer equipped with a CCD detector and Incoatec Microfocus Source IμS (30 W, multilayer mirror, MoKα).

The single crystal reflections could be indexed by space-group $Fd\bar{3}m$ with cell parameter a = 10.3488(5) Å. The solved structure, summarised in Table 4.3, is isostructural to that of $NaCdZn_2F_7$ [86, 87] with (Na, Cd), Zn, and F(1) atoms at the special positions (0,0,0), ($\frac{1}{2}$,$\frac{1}{2}$,$\frac{1}{2}$), and ($\frac{1}{8}$,$\frac{1}{8}$,$\frac{1}{8}$), respectively. The F(2) atom is at the position ($\frac{1}{8}$,$\frac{1}{8}$,z), where the free z coordinate can be converted to $x = -z+\frac{3}{4}$ to directly compare with the free x_{F2} coordinate of $NaSrCo_2F_7$ (0.33289(14)) [10], $NaCaCo_2F_7$ (0.3285(2)) [11] and the other recently studied pyrochlore fluorides [13, 12]. The refined F(2) z-coordinate in $NaCdCo_2F_7$ is z_{F2} = 0.41580(10) and after conversion, x_{F2} = 0.33420(10), which is close to the $NaSrCo_2F_7$ value and signals a compression of the CoF_6 octahedra along the <111>-type direction.

As with these previous examples, no superstructure reflections were seen, indicating no ordering of Na and Cd on the pyrochlore (16d) A-site. No $A-B$ intersite mixing was detected either.

Table 4.3: Refined $NaCdCo_2F_7$ single crystal diffraction data.

Space group: $Fd\bar{3}m$ (#227, origin 2)					
a = 10.3488(5) Å		V = 1108.3(3) Å^3		Z = 8	
Atom	Site	x/a	y/a	z/a	Occ.
Na	16d	0	0	0	0.5
Cd	16d	0	0	0	0.5
Co	16c	0.5	0.5	0.5	1
F(1)	8b	0.125	0.125	0.125	1
F(2)	48f	0.125	0.125	0.41580(10)	1

Table 4.4: Displacement parameters from the single-crystal refinement.

Atom	U_{11}	U_{22}	U_{33}	U_{23}	U_{13}	U_{12}
Na	0.01507(12)	0.01507(12)	0.01507(12)	-0.00292(4)	-0.00292(4)	-0.00292(4)
Cd	0.01507(12)	0.01507(12)	0.01507(12)	-0.00292(4)	-0.00292(4)	-0.00292(4)
Co	0.00836(10)	0.00836(10)	0.00836(10)	-0.00034(3)	-0.00034(3)	-0.00034(3)
F(1)	0.0167(3)	0.0167(3)	0.0167(3)	0	0	0
F(2)	0.0201(3)	0.0201(3)	0.0245(5)	0	0	-0.0106(3)

4.1.2.4 Magnetization

Temperature-dependent DC magnetization measurements in a constant field H = 2000 Oe (converted to magnetic susceptibility as $\chi = M/H$), with the field applied along the [100], [110] and [111] crystallographic directions of $NaCdCo_2F_7$, are shown in Figure 4.9. The data in all three high symmetry directions overlap,

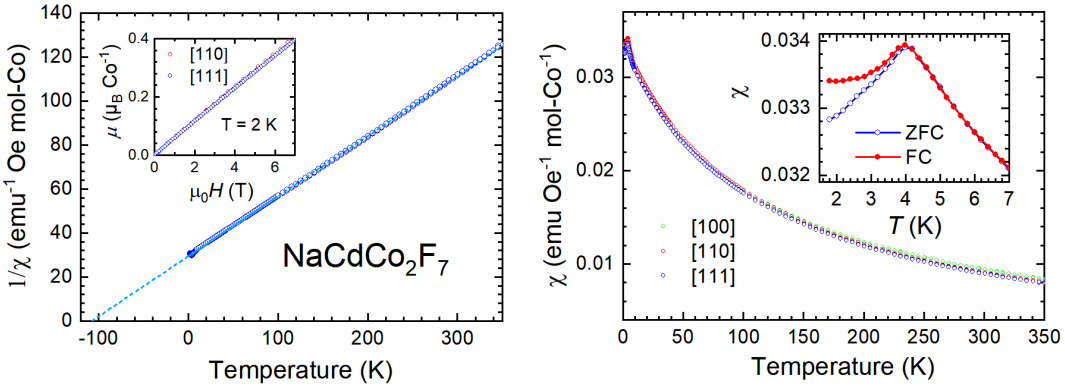

Figure 4.9: Inverse DC susceptibility of $NaCdCo_2F_7$ in $H \parallel [111]$ with the Curie-Weiss fit (left) and magnetization vs. field at $T = 2$ K in the [110] and [111] directions (top left inset). DC susceptibility in all three high-symmetry directions (right) and ZFC/FC splitting at $T_f = 4$ K (top right inset).

confirming the isotropic behaviour of DC susceptibility of $NaCdCo_2F_7$, as seen in the previously reported compounds $NaCaCo_2F_7$ and $NaSrCo_2F_7$. [10, 11] The inverse susceptibility $1/\chi$ data with $H \parallel [111]$ (main panel) were used for the Curie-Weiss fit in the temperature range of 100 - 350 K, in the standard form $\chi = C/(T - \theta_{CW})$, described in (1.45) and (1.66). The top left inset shows a very linear dependence of magnetization vs. field (at $T = 2$ K) up to $\mu_0 H = 7$ T in the [110] and [111] directions, justifying our calculation of susceptibility as M/H at 2000 Oe. The Curie-Weiss fit of the temperature-dependent susceptibility data yields a large negative Curie-Weiss temperature (a mean-field measure of the interaction strength) of θ_{CW} = -108.0(2) K, confirming that $NaCdCo_2F_7$ is a strongly frustrated Co-based pyrochlore with dominant antiferromagnetic interactions. A magnetic transition is seen at $T_f = 4.0$ K as a sharp cusp in the DC susceptibility, resulting in a high frustration index $f = |\theta_{CW}| / T_f = 27$. The effective moment per cobalt was extracted as $\mu_{eff} = 5.40(1)\ \mu_B$, which significantly differs from the $S = 3/2$ Co^{2+} spin-only value (3.87 μ_B) with quenched orbital momentum, and is approaching the $J = 9/2$ total angular momentum value (6.63 μ_B), as was seen previously in the other isostructural analogues. [10, 11]

The top right inset shows the zero field cooled (ZFC) and field cooled (FC) DC susceptibility data measured in a 100 Oe field applied parallel to the [110] direction of $NaCdCo_2F_7$. The cusp at $T = 4.0$ K, along with bifurcation of the ZFC and FC data indicate a magnetic transition with history dependence, either magnetic ordering or spin freezing into a disordered state – a spin glass. Cooling a spin-glass material below T_f in zero field results in a metastable state, in which the clusters of spins are frozen in random directions. Upon applying a field, the spin clusters partially align with the field, resulting in a configuration with a smaller net moment than in the field cooled process, where the clusters of spins are already preferentially aligned with the field at $T > T_f$ and freeze in this configuration below T_f.

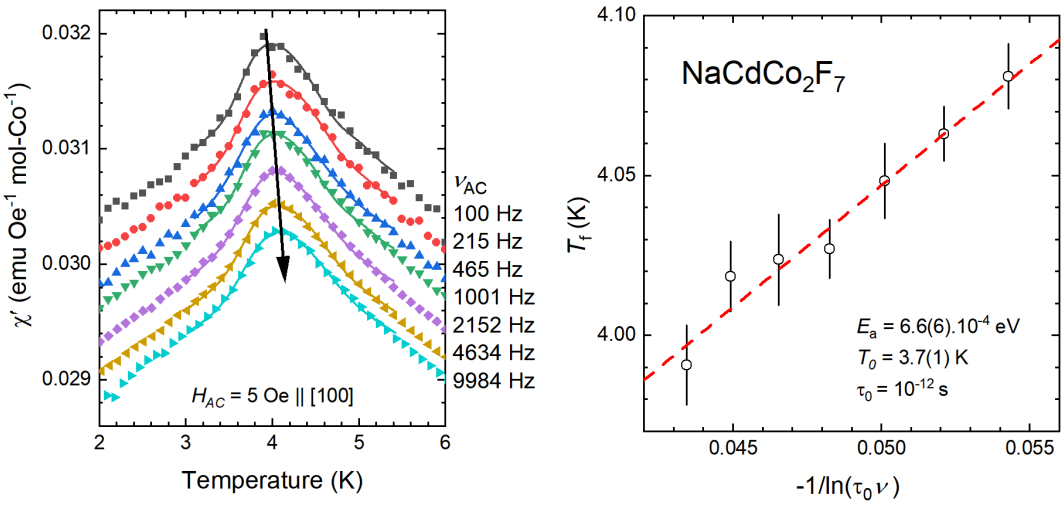

Figure 4.10: Real phase of AC susceptibility $\chi'(T)$ in $NaCdCo_2F_7$: shift of T_f with increasing frequency (left), fitted with the Vogel-Fulcher law (right).

4.1.2.5 AC susceptibility

AC susceptibility was measured as a function of temperature in the vicinity of the transition temperature ($T_f = 4.0$ K) to probe the spin dynamics of $NaCdCo_2F_7$ around the transition (Figure 4.10). A frequency-dependent excitation field with the amplitude of $H_{AC} = 5$ Oe was applied along the [100] crystallographic direction, with no additional DC field used. A frequency range of 10 Hz to 10 000 Hz (evenly distributed on the $\log_{10}$ scale) was employed, although the 10 Hz, 21.5 Hz and 46.4 Hz data were later omitted due to a large noise contribution to the signal. The data in Figure 4.10 with a frequency higher than 100 Hz are offset by a constant value of -2.5×10^{-4} emu/Oe.mol-Co for the sake of clarity.

The temperature-dependent measurement of the real component of AC susceptibility χ‘ reveals a rounded cusp centered around T_f with a weak but well defined frequency-dependent shift, indicative of a spin-glass ground-state. The peaks were fitted using an asymmetric “perturbed pseudo-Voigt“ function [94] to extract the freezing temperature as the maximum of χ‘. A shift in the freezing temperature $\Delta T_f = 0.12$ K (between 100 Hz and 10 000 Hz) was observed with increasing frequency as a shift of the χ‘ peak to higher temperatures. A quantitative measure of the frequency-dependent shift of the freezing temperature is given by the expression $\delta T_f = \Delta T_f / (T_f \Delta log_{10}\nu)$ (see (2.10)), describing a relative shift of T_f per decade of frequency in spin-glasses or spin-glass-like materials. [32] It can be evaluated from the linear fit of T_f vs. $\log_{10}\nu$ as the slope of the line divided by T_f. For $NaCdCo_2F_7$, we obtained $\delta T_f = 0.010(1)$. This value is similar to that of canonical (RKKY-type) spin-glasses such as AuFe (0.010) or CuMn (0.005), but lower than what is expected for insulating spin-glasses such as (EuSr)S (0.060) [32] or the pyrochlore fluorides $NaCaCo_2F_7$ (0.029) and $NaSrCo_2F_7$ (0.027). [10, 11].

Additional inferences about the properties of the spin-glass are typically extracted by fitting the frequency-dependent shift to the Vogel-Fulcher law (see (2.11), which takes into account the interactions of clusters of spins during the dynamic freezing process [32], as opposed to the Arrhenius law, which only con-

siders a thermally activated glass transition of non-interacting clusters (typical for superparamagnets). These parameters can be extracted from a linear fit on T_f vs. $-1/ln(\tau_0\nu)$, but since we are fitting a restricted frequency range (7 datapoints), free fitting of all parameters is not possible. Instead, the intrinsic relaxation time τ_0 is usually fixed to a value typical for the particular class of material (ranging from 10^{-13} s in conventional spin-glasses, to 10^{-7} s for cluster glasses and superparamagnets [10]). For a direct comparison with the compounds $NaCaCo_2F_7$ and $NaSrCo_2F_7$ [10, 11], the same value $\tau_0 = 10^{-12}$ s was used in our Vogel-Fulcher fit of $NaCdCo_2F_7$. We obtained $E_a = 6.6(6) \times 10^{-4}$ eV and $T_0 = 3.7(1)$ K, as opposed to 1.0×10^{-3} eV and 2.17 K in $NaCaCo_2F_7$, or 1.3×10^{-3} eV and 2.6(1) K in $NaSrCo_2F_7$. The actual physical meaning of "the ideal glass temperature" is still in dispute – the main possibilities are either relating it to the inter-cluster interaction strength in a spin-glass, or associating it with the true critical temperature of the phase transition, whereas T_f is the dynamic indication of the spin-freezing process. [32]

4.1.2.6 Specific heat

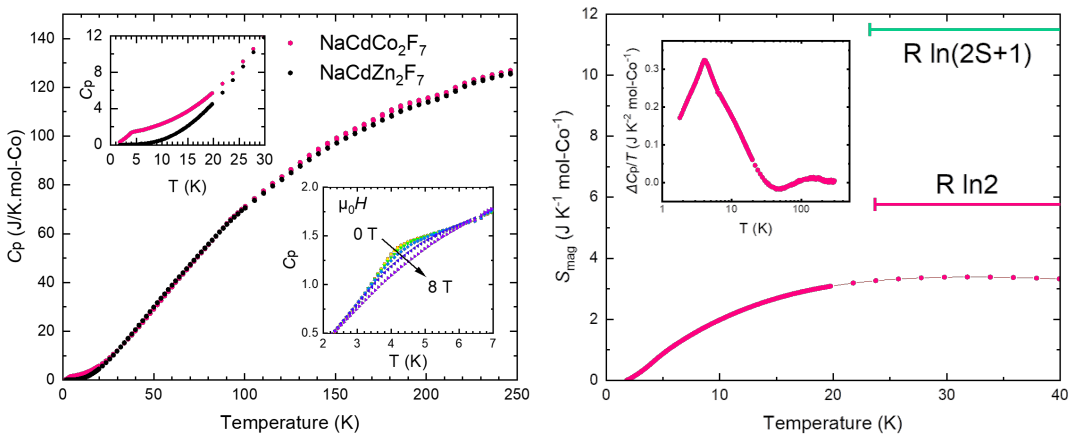

Figure 4.11: Specific heat of $NaCdCo_2F_7$ and $NaCdZn_2F_7$ (left panel), with the broad peak around 4 K zoomed in (top left inset) and suppressed with applied field (lower right inset). Magnetic entropy of $NaCdCo_2F_7$ (right panel) and the C_{mag}/T vs. T plot (top left inset).

The temperature dependence of the specific heat is shown in Figure 4.11. The lattice contribution was subtracted using the previously grown isostructural non-magnetic analogue $NaCdZn_2F_7$. In the left panel of Figure 4.11 we show the raw specific heat data of $NaCdCo_2F_7$, as well as the non-magnetic analogue $NaCdZn_2F_7$ with no further scaling.

To approximate the magnetic contribution to the specific heat, we subtracted the non-magnetic Zn data from the data of Co, to remove the phonon contribution as well as the step-like anomaly around 215 K from the Apiezon-N grease. The magnetic heat capacity $C_{mag} \approx \Delta C_p$ can be seen in the top-left inset of the right panel, where it is shown on the $\Delta C_p/T$ vs. T semi-logarithmic scale. A close-up look on the low-temperature region of the raw specific heat (top-left inset in the left panel) reveals that the specific heat of Co is much higher than that of Zn,

indicating a loss of entropy due to the spin-freezing transition. This transition is reflected on the magnetic specific heat as a broad peak around 4 K, which coincides with the freezing temperature extracted from the DC susceptibility cusp. Suppression of the peak with increasing applied field can be seen in the lower right inset, and is typical in spin-glass systems.

To estimate the magnetic entropy loss as a function of temperature, we integrated $\Delta C_p/T$ in the low-temperature region up to 40 K (right panel), in which the possible differences in the phonon contributions of Zn and Co do not play a significant part. We see a saturation of the magnetic entropy by 40 K, the value of which we can compare to the Heisenberg limit (R ln $(2S+1)$) and Ising limit (R ln2) for a $S = 3/2$ Co^{2+} magnetic ion. The saturated entropy is almost 60% of R ln(2) (similar result as seen in $NaCaCo_2F_7$ [10]), which may suggest an Ising-like nature of the system or a $J_{\text{eff}} = 1/2$ ground state, similar to the XY-type groundstate seen in the $J_{\text{eff}} = 1/2$ pyrochlores, $NaA'Co_2F_7$ (A' = Ca, Sr). [73] However, a microscopic look at the magnetic interactions is needed to further characterise the nature of the magnetism present in $NaCdCo_2F_7$.

4.1.3 $NaCdMn_2F_7$

The next compound we successfully managed to synthesize and fully characterize (however only in the polycrystalline form) is the $S = 5/2$ Mn^{2+}-based pyrochlore, $NaCdMn_2F_7$. Only one previous crystallographic and magnetic study was performed on the isostructural $NaSrMn_2F_7$ [13], allowing us to compare our results with the Mn^{2+}-based pyrochlore with Sr^{2+} on the A' site.

In the very late stage of the project, phase-pure crystals of $NaCdMn_2F_7$ were finally grown, but are yet to be fully characterized.

4.1.3.1 Solid state synthesis, PXRD

Similarly to the previous two compounds, 2 grams of the stoichiometric binary-fluoride mix were prepared in the glovebox, filled into a Pt tube, crimp-sealed with a double fold and inserted into the furnace inside two alumina crucibles with CaO. This time, a different heating protocol was used - ramp up to 800 °C at the rate of 2 °C/min, hold there for 3 hours and slow-cool to 600 °C over 7 days, then rapidly cool to room temperature:

$$NaF_{(s)} + CdF_{2(s)} + 2\ MnF_{2(s)} \xrightarrow[7\ \text{days}]{800°C \rightarrow 600°C} NaCdMn_2F_{7(s)}$$

White polycrystalline material was obtained, a small portion of which was ground and analyzed via PXRD. A phase-pure $NaCdMn_2F_7$ with the $Fd\bar{3}m$ pyrochlore structure was confirmed, with a refined lattice parameter $a = 10.5384(1)$ Å, lower than the predicted value in Table 4.2 by 0.4%. The F(2) x-coordinate was refined to $x_{F2} = 0.365(1)$.

4.1.3.2 Crystal growth, PXRD

About a gram of polycrystalline $NaCdMn_2F_7$, produced by solid-state synthesis described above, was filled into a Pt tube inside the glovebox, crimp-sealed with a double-fold and used for a recrystallization in the furnace. Aiming for a slow

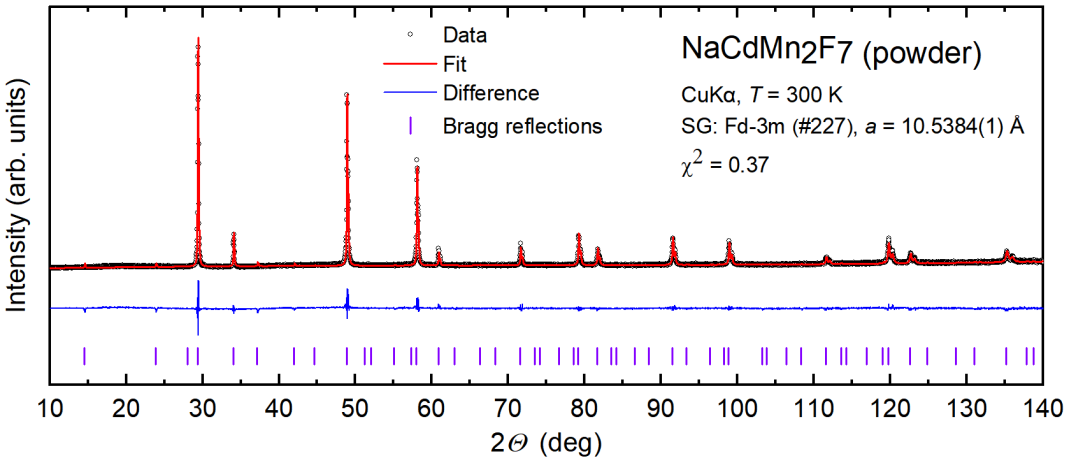

Figure 4.12: PXRD refinement of the phase-pure polycrystalline $NaCdMn_2F_7$.

crystallization from the melt, the following heating protocol was used: ramp up to 850°C at the rate of 2 °C/min, hold there for 3 hours, slow-cool to 650°C over 7 days, then rapidly cool to room temperature:

$$NaF + CdF_2 + 2\ MnF_2 \xrightarrow[7\ \text{days}]{850°C \rightarrow 650°C} NaCdMn_2F_7$$

Light-yellow transparent crystals were obtained, a small portion of which was ground and analyzed via PXRD. A phase-pure $NaCdMn_2F_7$ with the $Fd\bar{3}m$ pyrochlore structure was confirmed, with a refined lattice parameter $a = 10.5645(2)$ Å, higher than in the polycrystalline sample, but lower than the predicted value in Table 4.2 by 0.3%. The F(2) x-coordinate was refined to $x_{F2} = 0.3592(6)$.

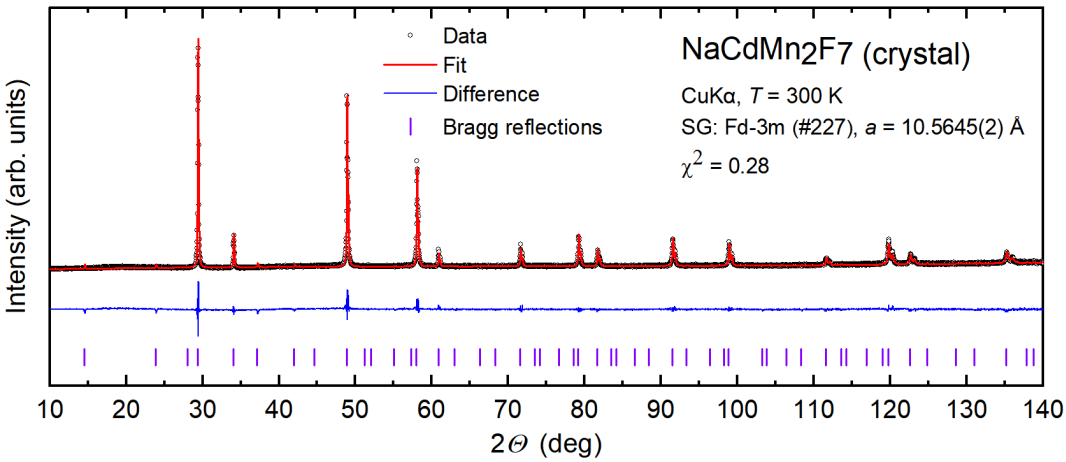

Figure 4.13: PXRD refinement of powdered crystals of $NaCdMn_2F_7$.

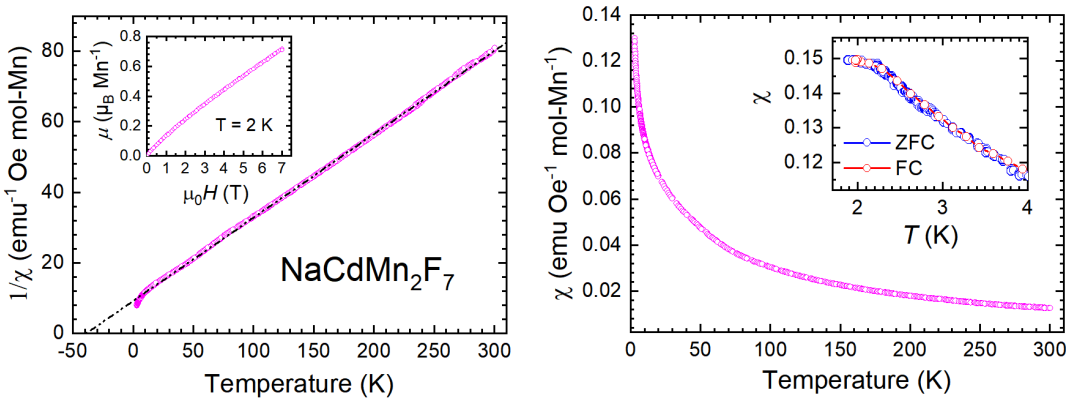

Figure 4.14: Inverse DC susceptibility of $NaCdMn_2F_7$ in $H = 2000$ Oe with the Curie-Weiss fit (left panel) and magnetization vs. field at $T = 2$ K (top left inset). DC susceptibility in $H = 2000$ Oe (right panel) and ZFC/FC curves in $H = 200$ Oe above 2 K (top right inset).

4.1.3.3 Magnetization

Temperature-dependent magnetizaton measurements in a constant field $H = 2000$ Oe (converted to magnetic susceptibility as $\chi = M/H$) on polycrystalline $NaCdMn_2F_7$ were performed in a Quantum Design Physical Property Measurement System (PPMS) using the Vibrating Sample Magnetometer (VSM) option [38] and can be seen in Figure 4.14. The top left inset shows a subtle curvature of the isothermal magnetization curve $\mu(H)$ (measured at $T = 2$ K) up to $\mu_0 H = 7$ T, however the magnetic moment is far from saturation ($\mu_{sat} = 2S\mu_B = 5\mu_B$).The inverse susceptibility $1/\chi$ data (left panel) were used for the Curie-Weiss fit in the temperature range of 100-300 K. The fit yields a negative Curie-Weiss temperature of θ_{CW} = -38.4(2) K, resulting in a frustration index $f = 19$ (as opposed to $\theta_{\mathrm{CW}} = -89.7$ K and $f = 35.9$ in $NaSrMn_2F_7$ [13]). The effective moment per manganese was extracted as $\mu_{\mathrm{eff}} = 5.81(1)\ \mu_B$, which closely approaches the high-spin free-ion $S = 5/2$ Mn^{2+} spin-only value (5.92 μ_B) with quenched orbital momentum ($L = 0$). Inside an octahedral crystal field, the $3d^5$ Mn^{2+} is usually found in the high spin configuration, with all three t_{2g} orbitals and both e_g orbitals singly occupied. However, a deviation from the ideal MnF_6 octahedral crystal field, dictated by the F(2) fluorine x-coordinate, can result in a deviation from the $L = 0$ effective moment due to an increased orbital contribution. This is seen in the higher effective moment of $NaSrMn_2F_7$ ($\mu_{\mathrm{eff}} = 6.25\ \mu_B$ for $x_{F2} = 0.3331(2)$), however, in our $NaCdMn_2F_7$ sample a lower effective moment is seen despite the large deviation from the ideal $x_{F2} = 0.3125$ value ($\mu_{\mathrm{eff}} = 5.81(1)$ μ_B for $x_{F2} = 0.365(1)$). Since our x_{F2} value was refined from a PXRD Rietveld refinement, it may not be trustworthy and single crystal diffraction measurements would be essential to confirm this x_{F2} value.

The right panel shows the DC susceptibility of $NaCdMn_2F_7$ measured in a 2000 Oe applied field. Due to the problems with temperature stabilization between 1.8-2.5 K, the measurement was performed in the temperature range 2.5-300 K and hence no cusp is seen in the low-temperature $\chi(T)$ data. The top right inset shows the zero field cooled (ZFC) and field cooled (FC) DC susceptibility data measured in a 200 Oe applied field between 1.9-4 K. Again, no cusp or bi-

furcation is seen in this temperature interval, although the maximum of $\chi(T)$ is reached around $T_f \approx 2.0$ K, again indicating a magnetic transition likely to be a spin-glass transition. The spin-freezing temperature in $NaSrMn_2F_7$ was taken as $T_f \approx 2.5$ K. [13]

4.1.3.4 AC susceptibility

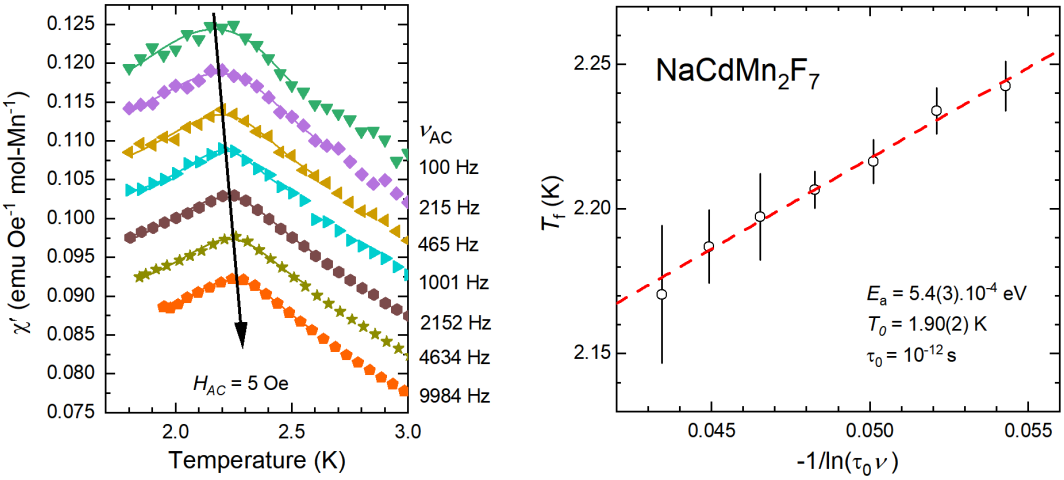

Figure 4.15: Real phase of AC susceptibility $\chi'(T)$ in $NaCdMn_2F_7$: a shift of T_f with increasing frequency (left), fitted with the Vogel-Fulcher law (right).

Temperature- and frequency-dependent AC susceptibility was measured in the vicinity of the transition temperature ($T_f \approx 2.0$ K) to probe the low-temperature freezing behaviour of polycrystalline $NaCdMn_2F_7$ (Figure 4.15). A frequency-dependent excitation field with the amplitude of $H_{AC} = 5$ Oe was applied with no additional DC field used. A frequency range of 10 Hz to 10 000 Hz (evenly distributed on the $\log_{10}$ scale) was employed, although the 10 Hz, 21.5 Hz and 46.4 Hz data were again omitted due to the large noise. The data in Figure 4.15 with a frequency higher than 100 Hz are offset by a constant value of -0.005 emu/Oe.mol-Mn for the sake of clarity.

The spin-glass ground-state is again indicated by the frequency-dependent shift of the rounded $\chi'(T)$ cusps, centered around the freezing temperature T_f. The peaks were fitted using an asymmetric "perturbed pseudo-Voigt" function [94] to extract the freezing temperature as the maximum of χ'. A shift in the freezing temperature $\Delta T_f = 0.07$ K (between 100 Hz and 10 000 Hz) was observed with increasing frequency. The relative shift of T_f per decade of frequency was evaluated as $\delta T_f = 0.018(1)$ from the linear fit of T_f vs. $\log_{10}\nu$, as the slope of the line divided by T_f. Unfortunately, the δT_f value for $NaSrMn_2F_7$ [13] is not explicitely stated. However, it could be recalculated from the Vogel-Fulcher graph using the "Digitize Image" function in Origin Pro 2019 software [95], using which we estimated a shift of approximately $\Delta T_f = 0.09$ K between two decades of frequency (100 Hz and 10 000 Hz), corresponding to $\delta T_f = 0.018$, agreeing with our obtained $NaCdMn_2F_7$ result.

Further probing of the spin-glass properties can again be done by fitting the frequency-dependent shift to the Vogel-Fulcher law with a linear fit of T_f vs.

$-1/ln(\tau_0\nu)$, but due to the fitting of a restricted frequency range (7 datapoints), the intrinsic relaxation time τ_0 was fixed to a reasonable spin-glass value $\tau_0 = 10^{-12}$, allowing us to directly compare with the fitted values with $NaSrMn_2F_7$ [13]. We obtained $E_a = 5.4(3) \times 10^{-4}$ eV and $T_0 = 1.90(2)$ K, as opposed to $8.3(4) \times 10^{-4}$ eV and 2.2(7) K in $NaSrMn_2F_7$. The lower spin-freezing activation energy and the ideal glass temperature can be ascribed to the lower mean-field interaction strength in $NaCdMn_2F_7$ given by θ_{CW} = -38.4(2) K, as opposed to $\theta_{CW} = -89.7$ K in $NaSrMn_2F_7$ [13].

4.1.3.5 Specific heat

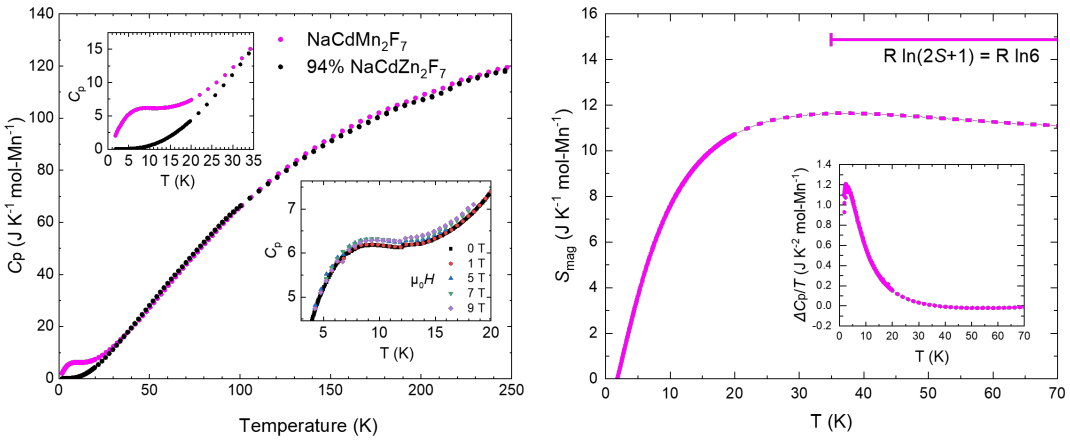

Figure 4.16: Specific heat of $NaCdMn_2F_7$ and 94%-scaled $NaCdZn_2F_7$ (left panel), with the broad low-temperature peak zoomed in (top left inset), not influenced by the applied field (lower right inset). Magnetic entropy of $NaCdMn_2F_7$ (right panel) and the C_{mag}/T vs. T plot (lower right inset).

The temperature-dependent specific heat is shown in Figure 4.16. The lattice contribution was again subtracted using the previously grown isostructural non-magnetic analogue $NaCdZn_2F_7$. In the left panel of Figure 4.11 we show the raw specific heat data of $NaCdMn_2F_7$ between 2-250 K in zero applied field, as well as the non-magnetic analogue $NaCdZn_2F_7$, this time scaled by a factor of 0.94 (or 94%) to better match the Mn data.

To approximate the magnetic contribution to the specific heat, we subtracted the scaled non-magnetic Zn data from the data of Mn, approximately removing the lattice vibration contribution. The magnetic heat capacity $C_{mag} \approx \Delta C_p$ can be seen in the bottom-right inset of the right panel, where it is shown on the linear $\Delta C_p/T$ vs. T scale. The zoomed-in low-temperature region of the raw specific heat (top-left inset in the left panel) reveals a rounded maximum between 2-20 K, with a much higher specific heat of Mn than that of Zn, indicating a loss of entropy due to the spin-freezing transition. As opposed to $NaCdCo_2F_7$, we do not see a suppression of the peak with increasing applied field, but rather the curves overlap, as can be seen in the bottom right inset of the left panel.

To provide a rough estimate of the magnetic entropy loss as a function of temperature, we integrated $\Delta C_p/T$ in the low-temperature region up to 70 K (right panel), in which there are only subtle differences in the phonon contributions of

Zn and Co. We see a saturation of the magnetic entropy by 35 K, the value of which we can compare to the Heisenberg limit (R ln $(2S+1) = R$ ln6) for a $S = 5/2$ Mn^{2+} magnetic ion. The saturated entropy is approximately 78% of R ln(6), meaning that less entropy is released in the spin-freezing transition than expected in a $S = 5/2$ Heisenberg magnetic system. Conversely, in the previously-studied $NaSrMn_2F_7$ the magnetic entropy saturates above R ln6, releasing more entropy during the transition.

4.1.4 $NaCdCu_2F_7$

Due to the strong Jahn-Teller effect in octahedral Cu^{2+} complexes [96], no Cu^{2+}-based pyrochlores have yet been studied [68] beyond the initial crystallographic report of the pyrochlore structure in the polycrystalline $NaCdCu_2F_7$ [9]. Synthesis of a single-crystalline $S = 1/2$ Cu^{2+}-based pyrochlore is of great interest due to the strong quantum fluctuations of the low-spin state in the $T \to 0$ limit, which could further destabilise magnetic order and potentially reach a quantum spin-liquid ground-state.

Here we report our latest progress with the crystal growth of the $S = 1/2$ $NaCdCu_2F_7$ pyrochlore fluoride. A small selection of basic characterization experiments were performed due to the rather large impurity content, aiming to optimize the growth before a full characterization of a phase-pure crystal is done.

4.1.4.1 Crystal growth, PXRD

Two grams of the stoichiometric binary-fluoride mix were prepared in the glovebox, filled into a Pt tube, crimp-sealed with a double fold and inserted into the furnace inside two alumina crucibles with CaO. Aiming for a slow crystallization from the melt, the following heating protocol was used: ramp up to 710 °C at the rate of 2 °C/min, hold there for 1 hour and slow-cool to 600 °C over 7 days, then rapidly cool to room temperature:

$$NaF + CdF_2 + 2\ CuF_2 \xrightarrow[7\ \text{days}]{710°C \to 600°C} NaCdCu_2F_7$$

A large number of small, clear transparent crystals with black and white inclusions/surface layers was obtained. A small selection of crystals was ground and analyzed via PXRD. The $Fd\bar{3}m$ pyrochlore structure of $NaCdCu_2F_7$ (91 wt.%) was confirmed, with a refined lattice parameter $a = 10.3278(4)$ Å, lower than the previously reported value 10.35 Å[9] by 0.2% and also lower than the predicted value in Table 4.2 by 0.4%. The F(2) x-coordinate was refined to $x_{F2} = 0.331(2)$. Two impurities were revealed: 3 wt.% of CdF_2 and 6 wt.% of $CdCuF_4$. [97] The black inclusions impurity is not shown in the PXRD refinement due to its low abundance, but they were later isolated and identified as CuO (also known as tenorite - monoclinic, S.G. $C12/c1$) in a separate PXRD refinement, meaning that our Pt tube leaked at high temperatures, hence the molten fluorides were exposed to air and subsequently oxidized. The oxidation could also happen due to any remaining adsorbed water in the highly hygroscopic CuF_2 precursor.

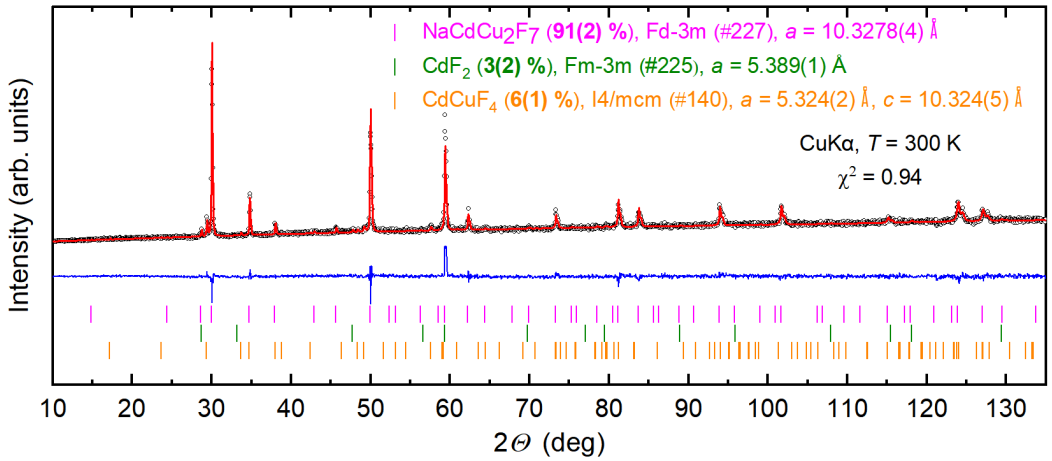

Figure 4.17: PXRD refinement of $NaCdCu_2F_7$ powdered crystals (91 wt.%), revealing CdF_2 (3 wt.%) and $CdCuF_4$ (6 wt.%) impurities.

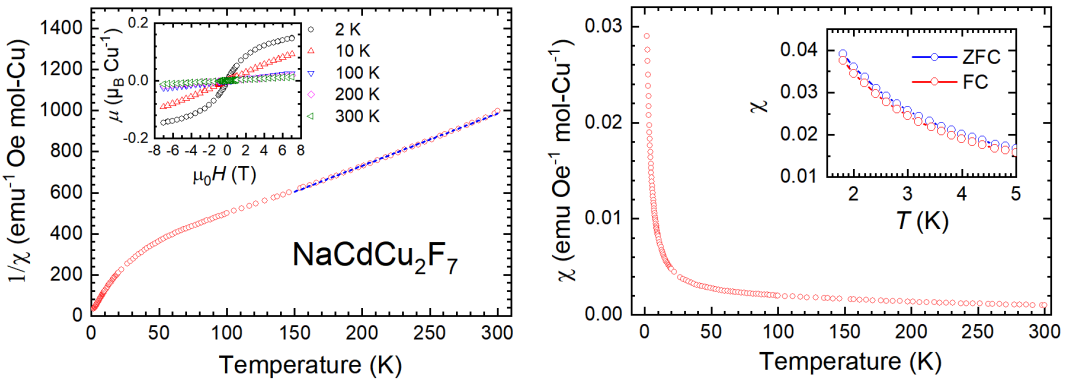

Figure 4.18: Inverse DC susceptibility of $NaCdCu_2F_7$ in $\mu_0 H = 1$ T with the 150-300 K Curie-Weiss fit (left panel) and magnetization vs. field at different temperatures (top left inset). DC susceptibility in $\mu_0 H = 1$ T (right panel) and ZFC/FC curves in $H = 1000$ Oe between 1.8-5 K (top right inset).

4.1.4.2 Magnetization

Temperature-dependent magnetizaton measurements in a constant field $H = 10$ 000 Oe (converted to magnetic susceptibility as $\chi = M/H$) were performed in a SQUID magnetometer inside a Quantum Design Magnetic Property Measurement System (model MPMS-XL 7T) using the Reciprocating Sample Option (RSO) mode and can be seen in Figure 4.18. The inverse susceptibility $1/\chi$ data (left panel) were used for the Curie-Weiss fit in the temperature range of 150-300 K. The fit yields a negative Curie-Weiss temperature of θ_{CW} = -87(2) K and the effective moment per copper $\mu_{eff} = 1.77(1)\ \mu_B$, which is slightly higher than the free-ion $S = 1/2$ Cu^{2+} spin-only value (1.73 μ_B) with quenched orbital momentum, possibly due to the additional orbital contribution as a result of the CuF_6 octahedron distortion (given by the refined free parameter $x_{F2} = 0.331(2)$). The top left inset shows the field dependence of the magnetic moment per copper at $T = 2$, 10, 100, 200 and 300 K. We see a highly linear dependence down to 10

K, however, at $T = 2$ K we see a Brillouin-shaped magnetization curve with no hysteresis. The curve approaches saturation at only 0.2 μ_B/Cu, whereas the saturated moment of a free $S = 1/2$ Cu^{2+} ion is expected to be 1 μ_B. The origin of this feature is still unknown to us, but one possible explanation includes a small unknown ferromagnetic impurity superimposed on the linear $\mu(H)$ curve. However, none of the impurities shown by PXRD are ferromagnetic: that includes the non-magnetic CdF_2, the long-range-ordered antiferromagnetic CuO ($T_N \sim$ 230 K) [98] and $CdCuF_4$, which shows a very linear inverse susceptibility down to 20 K and cooperative antiferromagnetic interactions ($\theta_{CW} \approx$ -3 K) down to the lowest measured temperature, 4.2 K. [97]

The right panel shows the DC susceptibility of $NaCdCu_2F_7$ measured in a 10 000 Oe applied field. No magnetic transition can be seen down to 1.8 K. The top right inset shows the zero field cooled (ZFC) and field cooled (FC) DC susceptibility data measured in a 1000 Oe applied field between 1.8-5 K. Again, no cusp or bifurcation is seen in this temperature interval, hence a sub-1.8 K Hall probe magnetometry measurement would be essential to uncover the magnetic ground-state of $NaCdCu_2F_7$. [13]

4.1.4.3 Specific heat

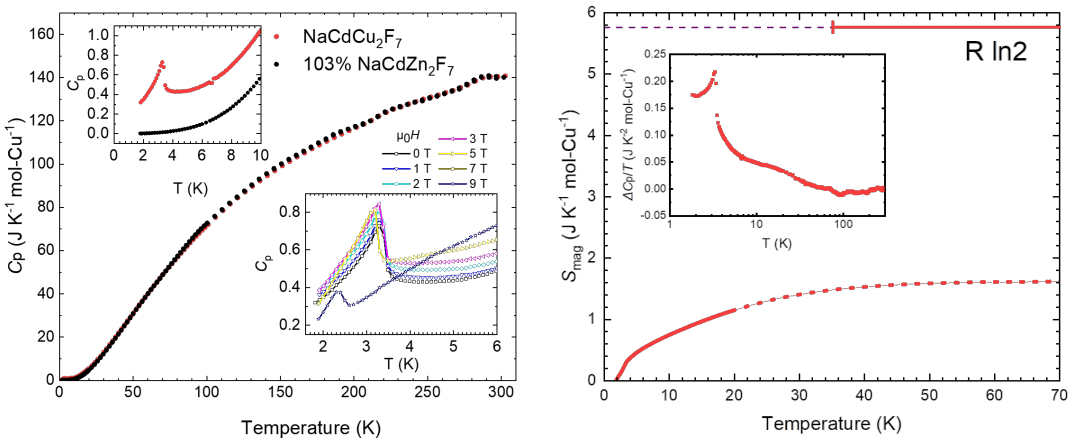

Figure 4.19: Specific heat of $NaCdCu_2F_7$ and 103%-scaled $NaCdZn_2F_7$ (left panel), with the low-temperature lambda-type peak zoomed in (top left inset), moved to lower temperatures by the applied field (lower right inset). Magnetic entropy of $NaCdCu_2F_7$ (right panel) and the C_{mag}/T vs. T plot (top inset).

The temperature-dependent specific heat is shown in Figure 4.19. The lattice contribution was once again subtracted using the previously grown isostructural non-magnetic analogue $NaCdZn_2F_7$. In the left panel of Figure 4.11 we show the raw specific heat data of $NaCdCu_2F_7$ between 1.8-300 K in zero applied field, as well as the non-magnetic analogue $NaCdZn_2F_7$ scaled by a factor of 1.03 (or 103 %) to better match the $NaCdCu_2F_7$ phonon contribution to the specific heat.

To approximate the magnetic contribution to the specific heat, we subtracted the scaled non-magnetic Zn data from the data of Cu, approximately removing the lattice vibration contribution. The magnetic heat capacity $C_{mag} \approx \Delta C_p$ can be seen in the top-left inset of the right panel, where it is shown on the semilogarithmic $\Delta C_p/T$ vs. T scale. The zoomed-in low-temperature region of the raw

specific heat (top-left inset in the left panel) reveals a lambda-shaped peak centered at $T_C = 3.3$ K, which shifts to lower temperatures with the application of an external field (down to 2.3 K at $\mu_0 H = 9$ T), as can be seen in the bottom right inset of the left panel. This behaviour is indicative of an antiferromagnetic ordering transition at $T_N = 3.3K$, although the peak is too small to originate from the primary phase and most likely comes from an unknown antiferromagnetic impurity. Looking at the impurities revealed by PXRD, the only potential candidate could be $CdCuF_4$, the only magnetic study of which reports weak antiferromagnetic interactions below 20 K, evidenced by a small negative Curie-Weiss temperature $\theta_{\mathrm{CW}} = -3K$. [97] The measurement of $CdCuF_4$ was carried out between 4.2-300 K, it is therefore unknown what happens in the low-temperature region below 4.2 K, where the peak in our specific heat appears.

To provide a rough estimate of the magnetic entropy loss as a function of temperature, we integrated $\Delta C_p/T$ in the low-temperature region up to 70 K (right panel). We see a saturation of the magnetic entropy by 60 K, the value of which we can compare to the Heisenberg limit (R ln $(2S{+}1) = R$ ln2) for a $S = 1/2$ Cu^{2+} magnetic ion, which in this case is equal to the Ising limit. The saturated entropy is only approximately 28% of R ln2. The explanation for this behaviour remains unknown at this point, hence new sub-1.8 K ^{3}He-probe specific heat measurements on a pure single-phase crystal are needed to confirm and fully explain this behaviour seen in our $NaCdCu_2F_7$ measurements.

4.1.5 $NaCdNi_2F_7$

Another member of the $NaCdB_2F_7$ pyrochlore fluoride family we decided to synthesize is the $S = 1$ Ni^{2+}-based pyrochlore, $NaCdNi_2F_7$. The previously-reported isostructural $NaCaNi_2F_7$ pyrochlore [12] was used in studies of spin freezing and persistent spin dynamics by μSR measurements [99]. Inelastic neutron scattering experiments [15, 100] showed a continuum of quantum fluctuations and proved that $NaCaNi_2F_7$ is an almost ideal model material for the realization of the $S = 1$ Heisenberg antiferromagnet on the pyrochlore lattice, despite the A-site Na/Ca disorder.

We managed to successfully synthesize polycrystalline $NaCdNi_2F_7$, however due to the rather large impurity content only magnetization was measured. In the very late stage of the project, several small phase-pure crystals of $NaCdNi_2F_7$ were finally grown, but are yet to be fully characterized.

4.1.5.1 Solid state synthesis, PXRD

Similarly to previous samples, 2 grams of the stoichiometric binary-fluoride mix were prepared in the glovebox, filled into a Pt tube with 30 mg of XeF_2, crimp-sealed with a double fold and inserted into the furnace inside two alumina crucibles with CaO. The following heating program was used: ramp up to 700 °C at the rate of 2 °C/min, hold there for 5 days and cool to room temperature:

$$\mathrm{NaF}_{(s)} + \mathrm{CdF}_{2(s)} + 2\ \mathrm{NiF}_{2(s)} \xrightarrow[5\ \mathrm{days}]{700°C\ \mathrm{in}\ \mathrm{Ar}_{(g)}/\mathrm{F}_{2(g)}} \mathrm{NaCdNi_2F_{7(s)}}$$

Lime green polycrystalline material was obtained, a small portion of which was ground and analyzed via PXRD. The $Fd\bar{3}m$ pyrochlore structure of $NaCdNi_2F_7$

(91 wt.%) was confirmed with a refined lattice parameter $a = 10.2528(1)$ Å, lower than the predicted value in Table 4.2 by 0.4% but agreeing perfectly with the previously-reported value [9]. The F(2) fluorine x-coordinate was refined to $x_{F2} = 0.3277(5)$. An impurity phase was also revealed: 9 wt.% of $NaNiF_3$ crystallizing in the orthorhombic *Pbnm* (#62) structure [101], with refined lattice parameters $a = 5.371(1)$ Å, $b = 5.533(1)$ Å and $c = 7.781(1)$ Å.

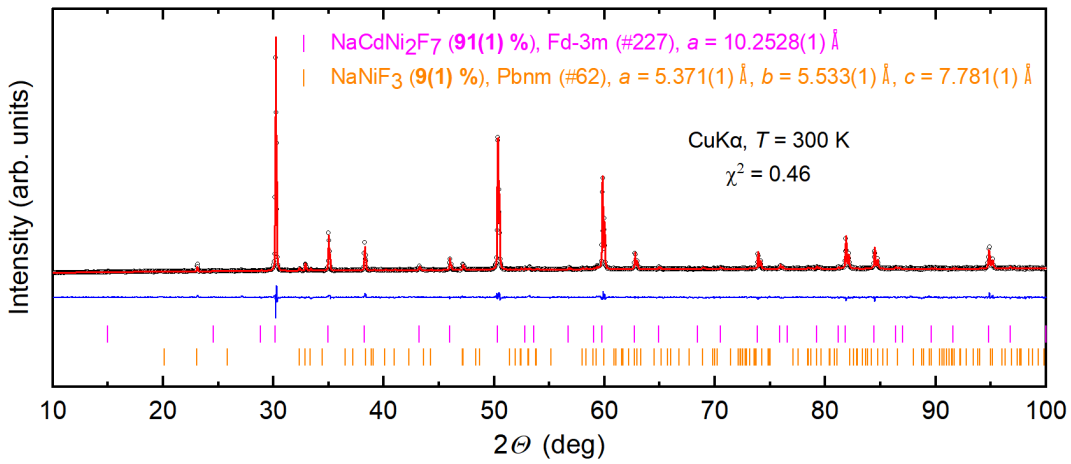

Figure 4.20: PXRD refinement of the polycrystalline $NaCdNi_2F_7$ (96 wt.%) with a 9 wt.% impurity phase, $NaNiF_3$ (2 wt.%).

4.1.5.2 Crystal growth, PXRD

Two grams of the stoichiometric binary-fluoride mix were sealed in a Pt crucible and inserted into the furnace like described above. Aiming for a slow crystallization from the melt, but not knowing the exact melting temperature, four different heating protocols were gradually tested with intermediate regrinds: ramp up to 800°C (1st regrind) / 850°C (2nd regrind) / 900°C (3rd regrind) / 950°C (4th regrind) at the rate of 2 °C/min, hold there for 3 hours and slow-cool by 100°C over 7 days, then rapidly cool to room temperature. The final successful heating protocol was as follows:

$$NaF + CdF_2 + 2\ NiF_2 \xrightarrow[7\ \text{days}]{950°C \rightarrow 850°C} NaCdNi_2F_7$$

Several small ($\sim$ 1 mm^3) transparent crystals of lime green color were obtained. Rest of the material was sintered into one polycrystalline lump, suggesting that a slightly higher temperature should be utilized in the next growth attempt. PXRD of the powdered crystals confirmed 98 % purity of $NaCdNi_2F_7$ with a refined lattice parameter $a = 10.2565(4)$ Åand the F(2) fluorine x-coordinate $x_{F2} = 0.326(1)$. A 2 wt.% CdF_2 impurity was also identified.

4.1.5.3 Magnetization

Temperature-dependent magnetization measurements in different fields (converted to magnetic susceptibility as $\chi = M/H$) on polycrystalline $NaCdNi_2F_7$ were per-

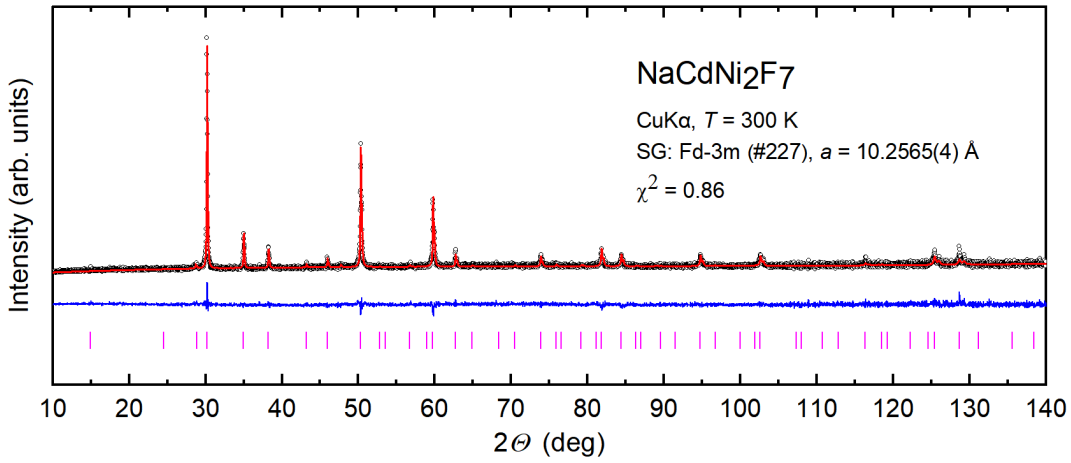

Figure 4.21: PXRD refinement of powdered $NaCdNi_2F_7$ single crystals (98 wt.%) with a 2 wt.% CdF_2 impurity phase.

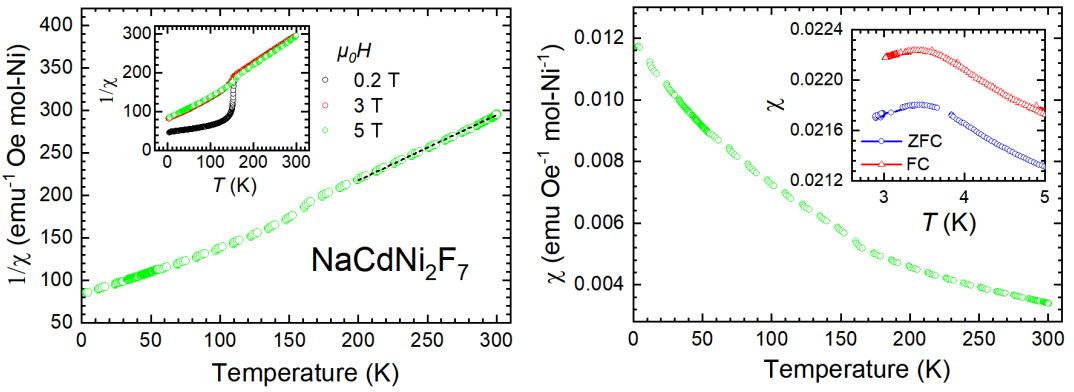

Figure 4.22: Inverse DC susceptibility of $NaCdMn_2F_7$ in $\mu_0 H = 5$ T with the 200-300 K Curie-Weiss fit (left panel) and inverse susceptibility at different fields (top left inset). DC susceptibility in $\mu_0 H = 5$ T (right panel) and ZFC/FC curves in $H = 2000$ Oe ($\mu_0 H = 0.2$ T) above 3 K (top right inset).

formed in a Quantum Design Physical Property Measurement System (PPMS) using the Vibrating Sample Magnetometer (VSM) option [38] and can be seen in Figure 4.14. Looking at the inverse susceptibility measured at 0.2 T, 2 T and 5 T applied fields (top left inset), we immediately spot a ferromagnetic impurity in the 0.2 T data, which saturates at higher applied field. According to the PXRD, there was a 9% impurity of $NaNiF_3$, which is an antiferromagnet (T_N = 156 K) with weak ferromagnetism along the c-axis and is matching the transition temperature seen in our data.

Despite the impurity, the inverse susceptibility $1/\chi$ data in applied field $\mu_0 H$ = 5 T (left panel) were used for the Curie-Weiss fit in the temperature range of 200-300 K to provide an estimate of the effective moment and the Curie-Weiss temperature. The fit yields a negative Curie-Weiss temperature of θ_{CW} = -82(1) K, as opposed to -129 K in $NaCaNi_2F_7$. [12] The effective moment per nickel was extracted as $\mu_{\mathrm{eff}} = 3.22(1)\ \mu_B$, which is higher than the free-ion $S = 1$

Ni^{2+} spin-only value (2.83 μ_B) with quenched orbital momentum ($L = 0$), but smaller than the $NaCaNi_2F_7$ value (3.7(1) μ_B/Ni). The higher effective moment seen in $NaCaNi_2F_7$ most likely originates from the enhanced distortion of NiF_6 octahedron ($x_{F2} = 0.3303(2)$) producing a higher orbital contribution, as opposed to the lower distortion in $NaCdNi_2F_7$ ($x_{F2} = 0.3277(5)$), causing a lower effective moment.

The right panel shows the DC susceptibility of $NaCdNi_2F_7$ measured in a 5 T applied field. The top right inset shows the zero field cooled (ZFC) and field cooled (FC) DC susceptibility data measured in a 2000 Oe applied field between 2.9-5 K, revealing a rounded cusp at $T_f \approx 3.5$ K, corresponding to a magnetic transition likely to be a spin-glass transition (seen at $T_f = 3.6$ K in $NaCaNi_2F_7$). The ZFC and FC curves are already split due to the history dependence of the impurity transition at 156 K.

4.1.6 $NaCdFe_2F_7$

The last compound from the transition-metal based $NaCdB_2F_7$ pyrochlore fluoride family is the $S = 2$ Fe^{2+}-based $NaCdFe_2F_7$. Two isostructural compounds, $NaCaFe_2F_7$ and $NaSrFe_2F_7$ have so far been reported in a single magnetic and structural study [13].

A solid-state synthesis as well as crystallization from the melt were attempted, however both resulted in a very large impurity content, making it impossible for us to further characterize this compound.

4.1.6.1 Solid state synthesis, PXRD

500 milligrams of the stoichiometric binary-fluoride mix were prepared in the glovebox, pressed into pellets using a quick-press kit for a better contact of the reactants, inserted into a Pt tube with 30 mg of XeF_2, crimp-sealed with a double fold and inserted into the furnace inside two alumina crucibles with CaO. The following heating program was used: ramp up to 700 °C at the rate of 2 °C/min, hold there for 1 day and cool to room temperature:

$$NaF_{(s)} + CdF_{2(s)} + 2\ FeF_{2(s)} \xrightarrow[1\ \text{day}]{700°C\ \text{in}\ Ar_{(g)}/F_{2(g)}} NaCdFe_2F_{7(s)}$$

After two regrinds, grey/silver polycrystalline material was obtained, a small portion of which was ground and analyzed via PXRD. We were able to confirm the $Fd\bar{3}m$ pyrochlore structure of $NaCdFe_2F_7$ (73 wt.%) with a refined lattice parameter $a = 10.4291(3)$ Å, lower than the predicted value in Table 4.2 by 0.07%. The F(2) fluorine x-coordinate was refined to $x_{F2} = 0.332(1)$. Two impurity phases were revealed: 13 wt.% of CdF_2 and 14 wt.% of FeF_2. [92]

4.1.6.2 Crystal growth, PXRD

Two grams of the stoichiometric binary-fluoride mix were sealed in a Pt crucible and inserted into the furnace like before. Aiming for a slow crystallization from the melt, the following heating protocol was tested: ramp up to 800°C at the rate of 2 °C/min, hold there for 3 hours, slow-cool to 600°C over 7 days, then rapidly

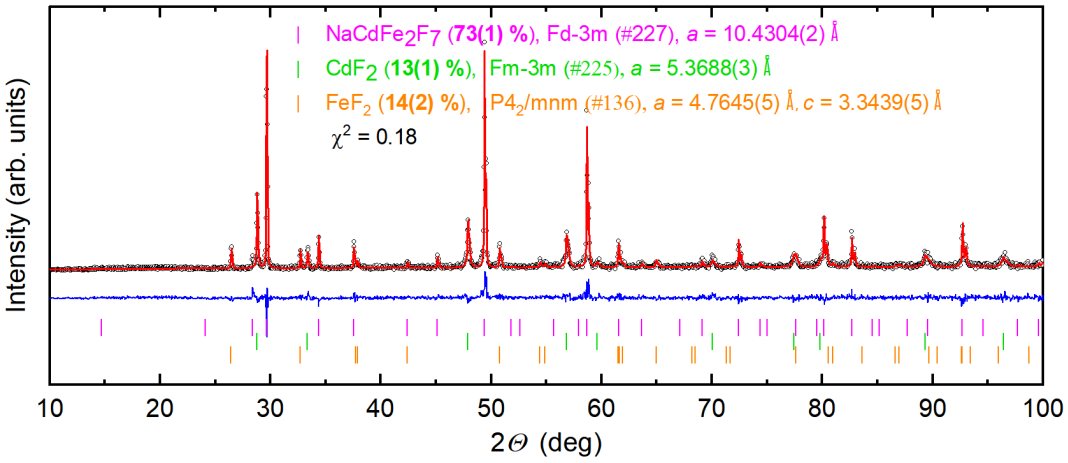

Figure 4.23: PXRD refinement of the polycrystalline $NaCdFe_2F_7$ (73 wt.%) prepared by solid-state synthesis at 700°C, with 13 wt.% CdF_2 and 14 wt.% FeF_2 impurities.

cool to room temperature:

$$NaF + CdF_2 + 2\ FeF_2 \xrightarrow[7\ \text{days}]{800°C \rightarrow 600°C} NaCdFe_2F_7$$

Multi-phase material consisting of crystals of different colors (brown, metallic silver, black and yellow) was obtained. A selection of the crystals were crushed for PXRD, which confirmed only 64 % of $NaCdFe_2F_7$ pyrochlore with a refined lattice parameter $a = 10.4422(3)$ Åand the F(2) fluorine x-coordinate $x_{F2} = 0.326(1)$. Impurities identified by PXRD included CdF_2 (22%) and FeF_2 (14 wt.%).

As we can see, $NaCdFe_2F_7$ decomposes at temperatures too high above the melting point, meaning that the highest temperature of the heating profile has to be optimized. In the future growth attempts, several temperatures between 700 and 800 $°C$ will be utilized to find the ideal temperature for the growth of phase-pure $NaCdFe_2F_7$ single crystals.

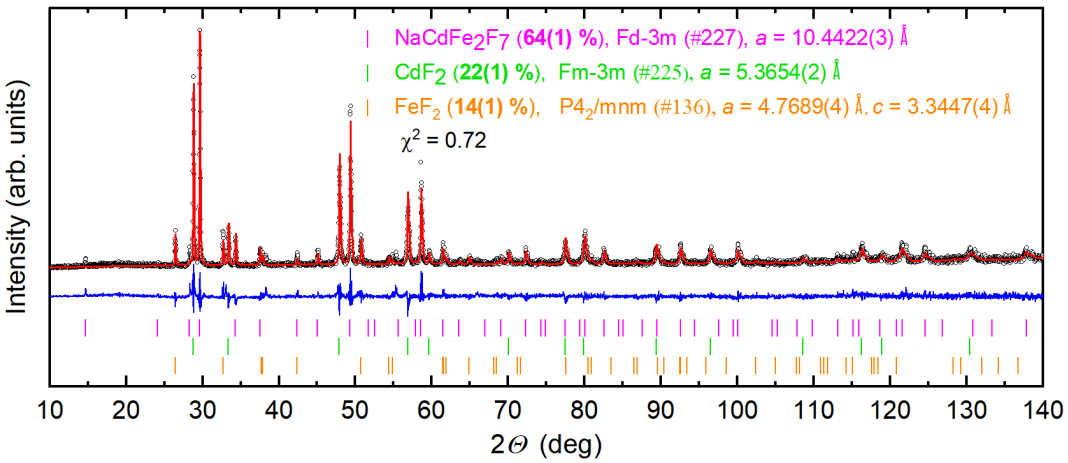

Figure 4.24: PXRD refinement of powdered $NaCdFe_2F_7$ crystals prepared at 800°C: $NaCdFe_2F_7$ (64 wt.%) with 22 wt.% CdF_2 and 14 wt.% FeF_2 impurites.

4.2 Kagome fluorides

4.2.1 $Na_3CdCo_3AlF_{14}$

Based on the mineral Coulsellite $Na_3CaMg_3AlF_{14}$ [20], which features an ordered dilution of the $NaCaMg_2F_7$ pyrochlore lattice by non-magnetic Al^{3+} ions and thus features 2D kagome networks of Mg ions in the *ab* plane, we decided to synthesize a magnetic $Na_3CdCo_3AlF_{14}$ kagome fluoride by replacing the non-magnetic Mg^{2+} ions by the magnetic $J_{\text{eff}} = 1/2$ Co^{2+} ions, as well as replacing the divalent Ca by Cd. By implementing the $J_{\text{eff}} = 1/2$ Co^{2+} ions on the kagome lattice, we hope to produce a new highly frustrated kagome antiferromagnet with a quantum liquid groundstate.

4.2.1.1 Crystal growth, PXRD

500 milligrams of the stoichiometric binary-fluoride mix were prepared in the glovebox, pressed into pellets using a quick-press kit, inserted into a Pt tube with 30 mg of XeF_2, crimp-sealed with a double fold and inserted into the furnace inside two alumina crucibles with CaO. The following heating program was used: ramp up to 800 °C at the rate of 1 °C/min, hold there for 60 minutes, slow-cool to 500 °C over the course of 7 days and rapidly cool to room temperature:

$$3\ NaF + CdF_2 + 3\ CoF_2 + AlF_3 \xrightarrow[7\ \text{days}]{800°C \rightarrow 500°C} Na_3CdCo_3AlF_{14}$$

A black/red recrystallized lump of multi-phase polycrystalline material was obtained, a small portion of which was ground and analyzed via PXRD. We were unable to confirm the $R\bar{3}m$ kagome structure of $Na_3CdCo_3AlF_{14}$, but we could identify the $Fd\bar{3}m$ pyrochlore structure of $NaCdCo_2F_7$ (20 wt.%) with a refined lattice parameter $a = 10.3157(4)$ Å, although it was not the most abundant phase. The biggest phase fraction (41 wt.%) belonged to Na_3AlF_6 (also known as the mineral cryolite) with a monoclinic $P2_1/n$ symmetry [102] and refined lattice parameters $a = 5.417(2)$ Å, $b = 5.570(1)$ Å, $c = 7.700(3)$ Å and $\beta = 90.18(4)°$. The second most abundant phase was identified as Na_2AlCoF_7 (28 wt.%) with the weberite-related monoclinic $C2/c$ structure [103] and refined lattice parameters $a = 12.386(3)$ Å, $b = 7.211(3)$ Å, $c = 24.053(6)$ Å and $\beta = 99.67(2)°$. Lastly, we identified 12 wt.% of CdF_2 [104] with the cubic $Fm\bar{3}m$ structure and a refined lattice parameter $a = 5.3842(3)$ Å.

Several different heating protocols will have to be attempted in the future to be able to produce single crystals of a new kagome antiferromagnet, $Na_3CdCo_3AlF_{14}$.

4.2.2 $Rb_2Co_3SnF_{12}$

Motivated by the previous research on $A_2Cu_3M'F_{12}$ compounds (A = Rb, Cs; M' = Sn, Zr, Hf, Ti) [17, 18, 81, 80], all based on the $S = 1/2$ Cu^{2+} ions on the kagome lattice, we decided to try to synthesize a new $J_{\text{eff}} = 1/2$ Co^{2+}-based kagome compound, $Rb_2Co_3SnF_{12}$ with the hope of destabilizing magnetic order down to the lowest temperatures.

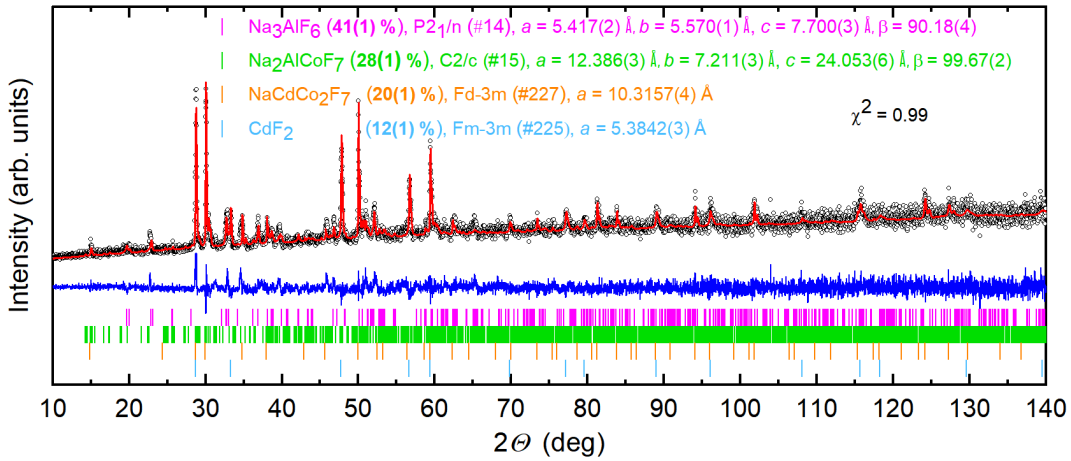

Figure 4.25: PXRD refinement of attempted $Na_3CdCo_3AlF_{14}$ synthesis, revealing Na_3AlF_6 (41 wt.%), Na_2AlCoF_7 (28 wt.%), $NaCdCo_2F_7$ (20 wt.%) and CdF_2 (12 wt.%) phases.

4.2.2.1 Crystal growth, PXRD

500 milligrams of the stoichiometric binary-fluoride mix were prepared in the glovebox, pressed into pellets using a quick-press kit, inserted into a Pt tube with 30 mg of XeF_2, crimp-sealed with a double fold and inserted into the furnace inside two alumina crucibles with CaO. The following heating program was used: ramp up to 800 °C at the rate of 1 °C/min, hold there for 60 minutes, slow-cool to 500 °C over the course of 7 days and rapidly cool to room temperature:

$$2\ RbF + SnF_4 + 3\ CoF_2 \xrightarrow[7\ \text{days}]{800°C \rightarrow 500°C} Rb_2SnCo_3F_{12}$$

A dark-red/white recrystallized lump of multi-phase polycrystalline material was obtained, a small portion of which was ground and analyzed via PXRD. We were unable to confirm the $R\bar{3}m$ kagome structure of $Rb_2Co_3SnF_{12}$. The biggest phase fraction (43 wt.%) belonged to Rb_2SnF_6 with a hexagonal $P\bar{3}m1$ symmetry [105] and refined lattice parameters $a = 6.0589(3)$ Å and $c = 4.8385(4)$ Å. The second most abundant phase was identified as CoF_2 (39 wt.%) [92] with the tetragonal $P4_2/mnm$ structure and refined lattice parameters $a = 4.6966(2)$ Å and $c = 3.1812(2)$ Å. Lastly, we identified 18 wt.% of $RbCoF_3$ [106] with the cubic $Pm\bar{3}m$ structure and a refined lattice parameter $a = 4.1282(2)$ Å.

We will have to be optimize the growth process using several different heating protocols to be able to produce single crystals of a new kagome antiferromagnet, $Rb_2Co_3SnF_{12}$.

4.2.3 $Cs_2Co_3ZrF_{12}$

Similarily to $Rb_2Co_3SnF_{12}$, we decided to attempt a synthesis of $J_{\text{eff}} = 1/2$ Co^{2+}-based kagome compound, $Cs_2Co_3ZrF_{12}$ by replacing the divalent $S = 1/2$ copper in the previously reported compound, $Cs_2Cu_3ZrF_{12}$ [107] by cobalt, again hoping to produce a highly frustrated $J_{\text{eff}} = 1/2$ kagome antiferromagnet.

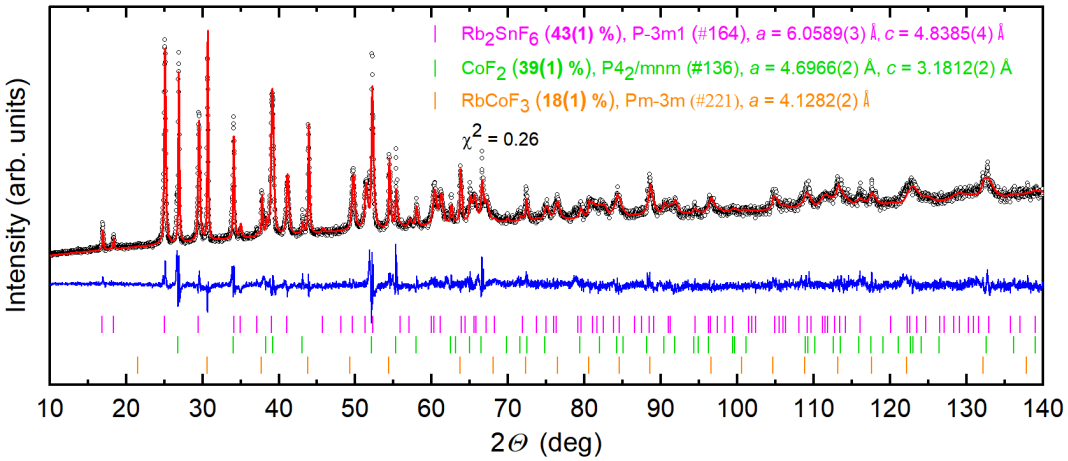

Figure 4.26: PXRD refinement of attempted $Rb_2Co_3SnF_{12}$ synthesis, revealing Rb_2SnF_6 (43 wt.%), CoF_2 (39 wt.%) and $RbCoF_3$ (18 wt.%) phases.

4.2.3.1 Crystal growth, PXRD

500 milligrams of the stoichiometric binary-fluoride mix were prepared in the glovebox, pressed into pellets using a quick-press kit, inserted into a Pt tube with 30 mg of XeF_2, crimp-sealed with a double fold and inserted into the furnace inside two alumina crucibles with CaO. The following heating program was used: ramp up to 800 °C at the rate of 1 °C/min, hold there for 60 minutes, slow-cool to 500 °C over the course of 7 days and rapidly cool to room temperature:

$$2\ CsF + ZrF_4 + 3\ CoF_2 \xrightarrow[7\ \text{days}]{800°C \rightarrow 500°C} Cs_2ZrCo_3F_{12}$$

A pink recrystallized lump of multi-phase polycrystalline material was obtained, a small portion of which was ground and analyzed via PXRD. We were unable to confirm the $R\bar{3}m$ kagome structure of $Cs_2Co_3ZrF_{12}$. The biggest phase fraction (74 wt.%) belonged to Cs_2ZrF_6 with a hexagonal $P\bar{3}m1$ symmetry [108] and refined lattice parameters $a = 6.4138(3)$ Å and $c = 5.0173(3)$ Å. The second most abundant phase was again identified as CoF_2 (21 wt.%) [92] with the the tetragonal $P4_2/mnm$ structure and refined lattice parameters $a = 4.6957(2)$ Å and $c = 3.1808(3)$ Å. Lastly, we identified 5 wt.% of $CsCoF_3$ [106] with the rhombohedral $R\bar{3}m$ structure and refined lattice parameters $a = 6.2003(5)$ Å and $c = 22.658(4)$ Å.

The growth procedure will have to be optimized using several different heating protocols in order to produce single crystals of a new kagome antiferromagnet, $Cs_2Co_3ZrF_{12}$.

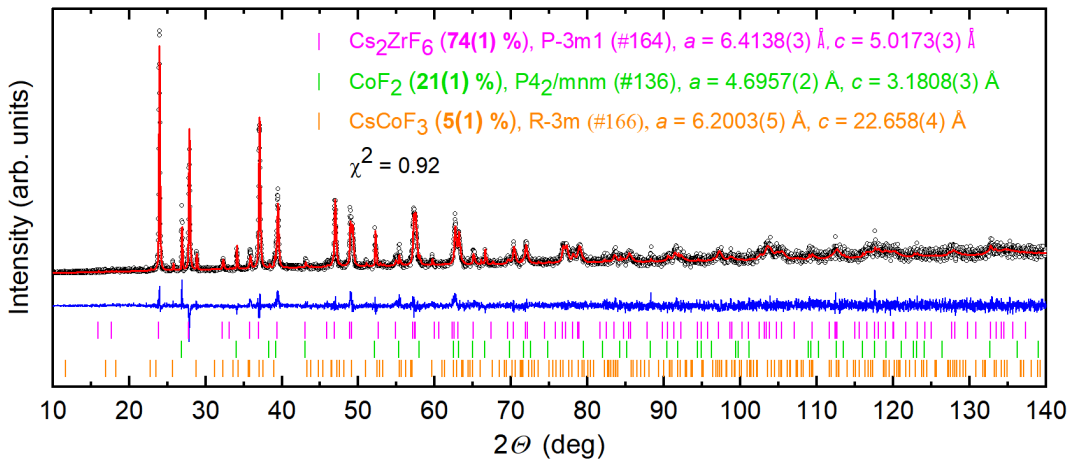

Figure 4.27: PXRD refinement of attempted $Cs_2Co_3ZrF_{12}$ synthesis, revealing Cs_2ZrF_6 (74 wt.%), CoF_2 (21 wt.%) and $CsCoF_3$ (5 wt.%) phases.

5. Discussion

The successful synthesis of a new series of pyrochlore fluoride compounds with the formula $NaCdB_2F_7$ ($B = Mn^{2+}$, Fe^{2+}, Co^{2+}, Ni^{2+}, Cu^{2+} and Zn^{2+}) confirmed the pyrochlore structure stability prediction [16] given by the tolerance factor τ described in the previous sections.

All newly-synthesized pyrochlore fluoride compounds were analyzed by PXRD and could be refined with the cubic $Fd\bar{3}m$ structure with one free parameter - the F(2) fluorine x-coordinate, x_{F2}. As was already shown, this parameter dictates the geometry of the BF_6 octahedra as well as the AF_8 dodecahedra. If $x_{F2} = 0.3125$, the BF_6 complex is an ideal octahedron with six equal F-B bond lengths and eight 90° F-B-F bond angles. When $x_{F2} > 0.3125$, the BF_6 octahedra are distorted in such a way that they are flattened along the local <111> direction (the axis of the octahedron), distorting away from the ideal 90° F-B-F bond angle by a value δ (creating 90°-δ and 90°+δ bond angles), but retaining 6 equal F-B bond lengths. This is important for the magnetism of $3d$ metals in octahedral complexes, as the distortion from the ideal octahedral crystal field can result in an orbital contribution to the effective moment, as opposed to the expected quenched orbital momentum value. The PXRD-refined structural parameters of samples used in the magnetization/AC-susceptibility/heat capacity measurements, as well as the data of the previously-reported isostructural pyrochlore fluoride compounds for comparison, are summarized in Table 5.1.

Single crystal diffraction performed on $NaCdCo_2F_7$ revealed no ordering of Na/Cd on the A-site, as well as no $A - B$ intersite mixing, as was the case in all of the previously studied pyrochlore fluorides. The rest of our single-crystalline samples are yet to be measured by SCXRD.

Table 5.1: Structural details of cubic ($Fd\bar{3}m$, origin 2) $AA'B_2F_7$ pyrochlores: our data (bold) vs. the previously reported data, including the experimentally determined lattice parameter a_{exp}, the free F(2) fluorine x-coordinate x_{F2}, the F-B-F bond angles distorted away from the ideal 90° value, the super-exchange pathway B-F-B bond angle and the B-F bond distance (from VESTA [76]).

Compound	a_{exp} (Å)	x_{F2}	F-B-F (°)	B-F-B (°)	B-F (Å)
$NaCdZn_2F_7$	**10.3399(3)**	**0.3268(7)**	**84.5(3) and 95.5(3)**	**133.0(4)**	**1.993(3)**
$NaCdZn_2F_7$ [86]	10.34657(3)	0.33273(10)	82.35(3) and 97.65(3)	129.80(6)	2.0197(5)
$NaCdMn_2F_7$	**10.5384(1)**	**0.365(1)**	**73.1(1) and 106.9(1)**	**114.4(3)**	**2.217(3)**
$NaSrMn_2F_7$ [13]	10.8012(3)	0.3331(2)	82.2 and 97.8	129.5	2.11
$NaCdFe_2F_7$	**10.4291(3)**	**0.332(1)**	**82.7(5) and 97.3(1)**	**130.3(7)**	**2.031(6)**
$NaCaFe_2F_7$ [13]	10.4471(2)	0.33702(18)	80.9 and 99.1	127.6	2.06
$NaSrFe_2F_7$ [13]	10.6323(4)	0.3313(2)	82.9 and 97.1	130.6	2.07
$NaCdCo_2F_7$	**10.3636(2)**	**0.3329(5)**	**82.3(2) and 97.7(2)**	**129.7(3)**	**2.024(3)**
$NaCaCo_2F_7$ [10]	10.4056(2)	0.33289(14)	82.3 and 97.7	129.8	2.03
$NaSrCo_2F_7$ [11]	10.545(4)	0.3285(2)	83.9 and 96.1	132.1	2.05
$NaCdNi_2F_7$	**10.2528(1)**	**0.3277(5)**	**84.2(2) and 95.8(2)**	**132.5(3)**	**1.980(3)**
$NaCaNi_2F_7$ [12]	10.3001(1)	0.3303(2)	83.2 and 96.8	131.3	2.00
$NaCdCu_2F_7$	**10.3278(4)**	**0.331(2)**	**82.9(6) and 97.1(6)**	**130.6(1)**	**2.010(8)**

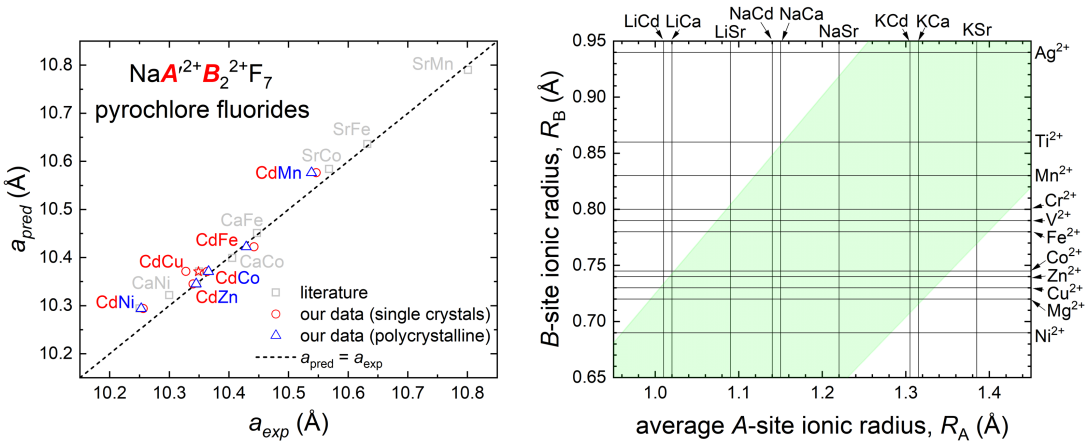

Figure 5.1: Predicted $NaA'B_2F_7$ lattice parameters [84] vs. the experimental values. (left) Prediction of new stable $AA'B_2F_7$ pyrochlores based on the structure tolerance factor τ [16]. The pyrochlore structure stability is expected in the green shaded region, where the predicted compounds are shown as the intersections of the vertical (AA') and horizontal (B) lines. (right)

The prediction of the lattice parameters of the $AA'B_2F_7$ disordered cubic fluoride pyrochlores [84] in the form $a_{\text{pred}} = 2.846R_A + 2.567R_B + 5.762$ also turned out exceedingly well, as can be seen in the plot in Figure 5.1 with a comparison with previously-reported compounds. The maximum difference between the predicted and experimentally determined values was around 0.04 Å($NaCdNi_2F_7$, $NaCdCu_2F_7$ and $NaCdMn_2F_7$). Ahrens ionic radii for a six-fold coordination of ions were used in this calculation, as suggested by Sidey. [84]

As we were able to confirm, the pyrochlore structure tolerance factor τ can be used to predict new families of stable $AA'B_2F_7$ pyrochlore fluorides, based purely on the average A-site ionic radius, R_A and the B-site ionic radius, R_B. Shannon ionic radii [82] (CN = 6 for R_B, CN = 8 for AA') are used in the calculation of τ. In Figure 5.1, we show the plot of R_B vs. R_A with the predicted stability region (shaded green) given by $0.823 \leq 3(R_A + R_F)/(\sqrt{17}(R_B + R_F)) \leq 0.946$, which can be used in our future work to plan a synthesis of new $AA'B_2F_7$ families. For each AA' combination (vertical line), we are able to predict stable $AA'B_2F_7$ compounds as the intersections with B^{2+} ions (horizontal lines) inside the green region. As an example, combinations of $A = Li^+$, Na^+, K^+ and $A' = Ca^{2+}$, Sr^{2+} and Cd^{2+} are shown for $B = Mg^{2+}$, Ti^{2+},V^{2+}, Cr^{2+}, Mn^{2+}, Fe^{2+}, Co^{2+}, Ni^{2+}, Cu^{2+}, Zn^{2+} and Ag^{2+} (the rest is ommited for clarity).

The measured magnetic properties of $NaCdB_2F_7$ pyrochlores (except for Fe, which has not yet been measured) are summarized in Table 5.2 and compared with the previous results. Curie-Weiss fits of the high-temperature DC inverse susceptibility regions reveal large negative Curie-Weiss temperatures (ranging from -38.4 K in $NaCdMn_2F_7$ to -108 K in $NaCdCo_2F_7$), indicating strong antiferromagnetic interactions. No magnetic ordering is visible until a magnetic transition is seen below 5 K in B = Mn, Co and Ni as a cusp in the DC susceptibility, confirming that $NaCdB_2F_7$ fluorides are highly frustrated pyrochlore antiferromagnets with frustration indices ranging from 19 in $NaCdMn_2F_7$ to more than 48 in $NaCdCu_2F_7$ (no magnetic transition seen down to the lowest measured temper-

Table 5.2: Magnetic properties of $AA'B_2F_7$ pyrochlores: our data (bold) vs. the previously reported data, including the B^{2+}-ion's spin-state S, the extracted effective moment per B^{2+} ion, the calculated free-ion spin-only moment $\mu_S = 2\sqrt{S(S+1)}\mu_B$, the calculated free-ion J moment $\mu_J = g_J\sqrt{J(J+1)}\mu_B$, the spin-freezing temperature T_f, the Curie-Weiss temperature θ_{CW} and the frustration index $f = |\theta_{CW}|/T_f$. Question marks imply unknown or questionable data.

Compound	S	μ_{eff}/B^{2+} (μ_B)	μ_S (μ_B)	μ_J (μ_B)	T_f (K)	θ_{CW} (K)	f
$NaCdMn_2F_7$	$\frac{5}{2}$	**5.81(1)**	5.92	5.92	**2.0**	**-38.4(2)**	**19**
$NaSrMn_2F_7$ [13]		6.25			2.5	-127	51
$NaCdFe_2F_7$		**?**			**?**	**?**	**?**
$NaCaFe_2F_7$ [13]	2	5.61	4.90	6.70	3.9	-72.8	19
$NaSrFe_2F_7$ [13]		5.94			3.7	-98.1	27
$NaCdCo_2F_7$		**5.40(1)**			**4.0**	**-108.0(2)**	**27**
$NaCaCo_2F_7$ [10]	$\frac{3}{2}$	6.1	3.87	6.63	2.4	-140	58
$NaSrCo_2F_7$ [11]		5.9			3.0	-127	42
$NaCdNi_2F_7$	1	**3.22(1)?**	2.83	5.59	**3.5**	**-82(1)**	**23**
$NaCaNi_2F_7$ [12]		3.7			3.6	-129	36
$NaCdCu_2F_7$	$\frac{1}{2}$	**1.77(1)**	1.73	3.55	**<1.8**	**-87(2)**	**>48**

ature, 1.8 K). These transitions show a history dependence, which is evidenced by the ZFC/FC curve splitting below the transition temperature. Additional AC susceptibility and heat capacity measurements in B = Co and Mn suggested that this transition is a spin-glass transition, as seen in all previously-reported pyrochlore fluorides. [10, 11, 12, 13] The spin-glass transition in the pyrochlore Heisenberg antiferromagnets is believed to originate from the enhanced magnetic bond disorder brought about by the chemical disorder on the A-site, which comes as a result of the effective 1.5+ valence state to preserve the overall chemical neutrality in $AA'B_2F_7$ pyrochlores. [71]

In Figure 5.2, we attempted to relate the magnetic properties of $NaA'B_2F_7$ (A' = Cd, Ca, Sr; B = Mn, Fe, Co, Ni) pyrochlore fluorides to the structural distortion of BF_6 octahedra. In the top right figure, we show the B-F-B bond angle between two corner-sharing BF_6 octahedra, which influences the character of the super-exchange interaction between two neighbouring B^{2+} ions, mediated by an intermediate fluorine F^- ligand. Generally, a 90 degree B-F-B bond angle results in a ferromagnetic exchange, while a 180 degree B-F-B bond angle causes an antiferromagnetic exchange interaction. Therefore, we would normally expect a larger negative Curie-Weiss temperature with the increasing B-F-B bond angle. This is seen in $NaCdMn_2F_7$-$NaSrMn_2F_7$ and $NaCaFe_2F_7$-$NaSrFe_2F_7$, but the trend is unclear with the rest. In the bottom-left figure, a similar consideration was made to relate the Curie-Weiss temperature to the B-F bond length, expecting larger negative Curie-Weiss temperature with a decreasing B-F bond distance due to a larger B-F wavefunction overlap, resulting in a stronger exchange interaction. This is only seen in $NaCdMn_2F_7$-$NaSrMn_2F_7$ and $NaCaCo_2F_7$-$NaSrCo_2F_7$, while the opposite is seen in the rest. In the bottom-right figure, we tried to relate the B^{2+} effective moment to the degree of distortion of the F-B-F bond from the ideal 90° value, δ. In octahedral complexes of 3d-metal B^{2+} ions, the orbital moment is

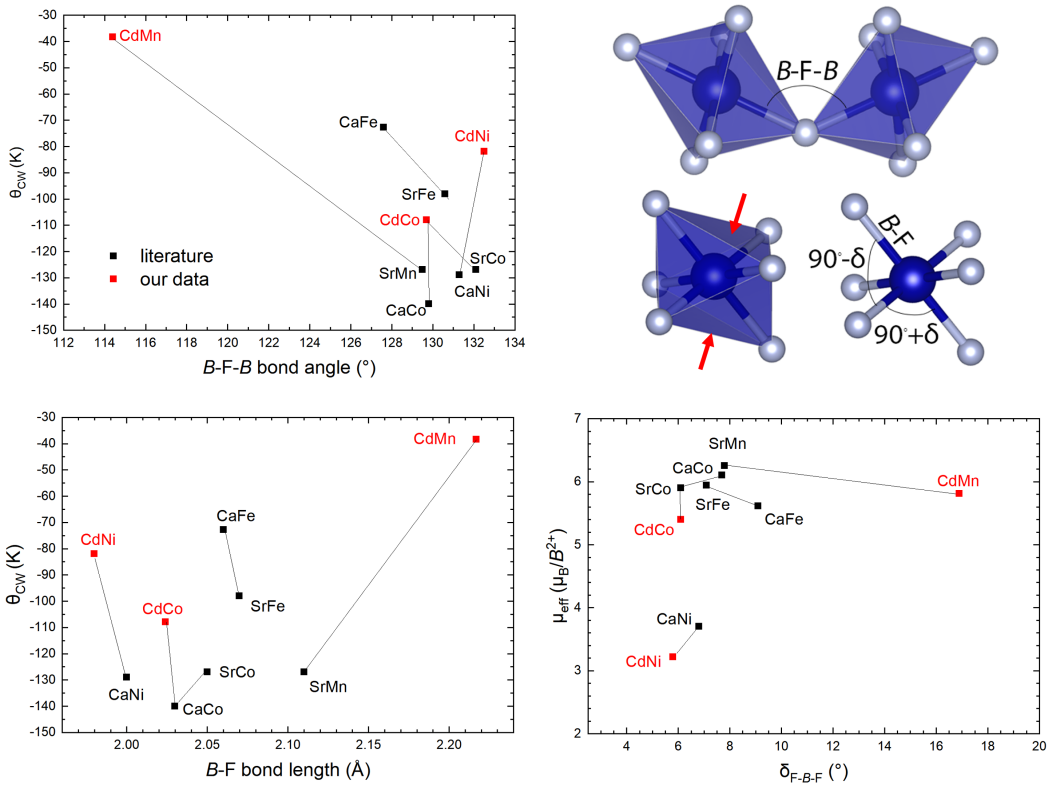

Figure 5.2: The super-exchange B-F-B bond angle, as well as the BF_6 octahedron distortion along the <111> direction. (top-right) The Curie-Weiss temperature as a function of the super-exchange B-F-B bond angle (top-left) and the B-F bond length (bottom-right). The B^{2+} effective moment as a function of the distortion angle, δ.

usually quenched by the ideal octahedral crystal electric field, resulting in an effective moment close to the free-ion spin-only value. As soon as the octahedron is distorted, some orbital contribution is present and the effective moment is larger. We see this only in $NaCdNi_2F_7$-$NaCaNi_2F_7$ and $NaCaCo_2F_7$-$NaSrCo_2F_7$, but not in the rest of the materials. The discrepancies in the expected trends could be caused by the imprecise refinement of the F(2) fluorine x_{F2} coordinate, which was done by a Rietveld refinement of the PXRD data. Accurate structural data from single crystal XRD, as well as a larger dataset would be essential to draw any conclusions from this analysis.

Temperature- and frequency-dependent AC susceptibility measurements of $NaCdCo_2F_7$ and $NaCdMn_2F_7$ showed a small frequency-dependent shift of the real-phase χ' peak (centered at the freezing temperature T_f) towards higher temperatures, a typical behaviour seen in spin-glass materials. [32] This is usually parametrized by the relative shift of T_f per decade of frequency, $\delta T_f = \Delta T_f/(T_f \Delta log_{10}\nu)$, the magnitude of which is usually typical for a particular class of materials. The lowest frequency-dependent shift is seen in canonical (metallic, RKKY-type) spin glasses with δT_f between 0.0045 (AuMn) and 0.018 (NiMn). The frequency dependence is a magnitude higher in insulating spin glasses (δT_f = 0.060 in (EuSr)S or 0.080 in $(FeMg)Cl_2$), while the biggest frequency-dependent shift is seen in superparamagnets (δT_f = 0.280 in α-$(Ho_2O_3)(B_2O_3)$). [32] The

Table 5.3: AC susceptibility data, including the relative shift of T_f per decade of frequency and the fitted Vogel-Fulcher parameters: the intrinsic relaxation time τ_0 (fixed), the spin-freezing activation energy E_a and the ideal glass temperature T_0.

Compound	δT_f	τ_0 (s)	E_a (meV)	T_0 (K)
$NaCdMn_2F_7$	**0.018(1)**	10^{-12}	**0.54(3)**	**1.90(2)**
$NaSrMn_2F_7$ [13]	0.018(1)	10^{-12}	0.83(4)	2.2(7)
$NaCdCo_2F_7$	**0.010(1)**	10^{-12}	**0.66(6)**	**3.7(1)**
$NaCaCo_2F_7$ [10]	0.029(1)	10^{-12}	1.0(1)	2.2(1)
$NaSrCo_2F_7$ [11]	0.027(1)	10^{-12}	1.3(1)	2.6(1)

obtained results, compared with the previously-reported data are summarized in Table 5.3. Equal δT_f was seen in $NaCdMn_2F_7$ and $NaSrMn_2F_7$ [13], while the relative shift seen in $NaCdCo_2F_7$ was approximately three times lower than in $NaCaCo_2F_7$ and $NaSrCo_2F_7$, although all values fall within the expected insulating spin-glass range. The frequency-dependent shift was fitted to the Vogel-Fulcher law with a fixed, physically reasonable intrinsic relaxation time $\tau_0 = 10^{-12}$ s, as was done in all previous pyrochlore fluoride studies. [10, 11, 12, 13] The activation energy of the spin-freezing transition, as well as the ideal glass temperature are lower in $NaCdMn_2F_7$ than in $NaSrMn_2F_7$, which could be ascribed to the lower mean-field interaction strength between the clusters of spins ($\theta_{CW} = -38$ K in $NaCdMn_2F_7$, while $\theta_{CW} = -127$ K in $NaSrMn_2F_7$). The same trend, however, is not seen in $NaCdCo_2F_7$ ($\theta_{CW} = -108$ K), which shows a lower E_a, but higher T_0 than the two previously-studied cobalt pyrochlore fluorides, which are more strongly frustrated ($\theta_{CW} = -140$ K and -127 K in $NaCaCo_2F_7$ and $NaSrCo_2F_7$, respectively). The physical meaning of T_0 is still unknown, but the possibilities include either relating it to the inter-cluster interaction strength in spin glasses, or it could be the actual critical temperature of the spin-freezing transition, for which T_f is just a dynamic manifestation. [32]

Specific heat measurements were done on the B = Co (single crystal), Mn and Cu (polycrystalline) samples to further probe the magnetic ground state of these highly frustrated pyrochlore fluorides. In $NaCdCo_2F_7$ and $NaCdMn_2F_7$, a broad peak in the low-temperature region was seen, again reinforcing the idea of a spin-glass ground state. [32] In $NaCdCu_2F_7$, we saw a small, sharp lambda-shaped peak at $T = 3.3$ K, which moved to lower temperatures upon the application of high fields, suggesting an antiferromagnetic ordering transition from an impurity (likely $CdCuF_4$). Following the specific heat subtraction of Zn, we were able to estimate the magnetic specific heat, which was used for a temperature-dependent entropy loss estimation as the integration of C_{mag}/T vs. T. The magnetic entropy of $NaCdCo_2F_7$ saturated at 40 K to about 60% of R ln2, suggesting either an Ising-like nature of the ground state or a $J_{eff} = 1/2$ ground state, in line with the previous studies of XY-type anisotropy in $J_{eff} = 1/2$ $NaA'Co_2F_7$ (A' = Ca, Sr). [73] In $NaCdMn_2F_7$, we saw a saturation at 35 K to about 80% of R ln6, indicative of the high-spin $S = 5/2$ Mn^{2+} configuration. In $NaCdCu_2F_7$, the saturation entropy only reached about 30% of R ln2, the reason of which is still unclear to us.

Conclusion

In this work, we presented a successful synthesis of a new pyrochlore fluoride family with the composition $NaCdB_2F_7$ (B = Zn, Mn, Fe, Co, Ni and Cu), and an unsuccessful synthesis of new $Na_3CdCo_3AlF_{14}$, $Rb_2SnCo_3F_{12}$ and $Cs_2ZrCo_3F_{12}$ kagome compounds. A variety of sample synthesis techniques were utilized, including the solid-state synthesis of polycrystalline materials, as well as laser floating zone melting and melt crystallization for the single crystal growth.

We were able to grow small single crystals (~ 1 mm^3) of B = Zn, Co, Mn, Ni and Cu pyrochlore fluorides, although only Co has so far been fully characterized. The Zn sample was used as a non-magnetic analogue in the heat capacity measurements. The crystals of Mn and Ni were grown in the late stage of the project, thus we only present the measurements on polycrystalline samples. The Cu crystals have a rather large impurity content and the growth has to be optimized before further measurements are performed. The Fe sample has so far not been synthesized in a phase-pure form, hence different synthesis techniques have to be attempted. On the other hand, the attempted syntheses of $Na_3CdCo_3AlF_{14}$, $Rb_2SnCo_3F_{12}$ and $Cs_2ZrCo_3F_{12}$ did not lead to the creation of the intended kagome phases.

The structural PXRD measurements on $NaCdB_2F_7$ compounds confirmed the $Fd\bar{3}m$ pyrochlore structure, while SCXRD showed full A-site disorder and no $A-B$ intersite mixing in the Co sample. The magnetic measurements revealed large negative Curie-Weiss temperatures, indicative of strong antiferromagnetic interactions. The materials show no magnetic transition down to temperatures as low as 4 K, suggesting that the new $NaCdB_2F_7$ compounds are strongly frustrated pyrochlore antiferromagnets with a weak bond disorder induced by the A-site chemical disorder, which precipitates a spin-freezing transition into a spin-glass ground state.

Bibliography

[1] L. Balents. Spin liquids in frustrated magnets. *Nature*, 464:199–208, Mar 2010.

[2] P.W. Anderson. Resonating valence bonds: A new kind of insulator? *Materials Research Bulletin*, 8(2):153–160, 1973.

[3] Lucile Savary and Leon Balents. Quantum spin liquids: a review. *Reports on Progress in Physics*, 80(1):016502, nov 2016.

[4] J. Gardner, M. Gingras, and J. Greedan. Magnetic Pyrochlore Oxides. *Reviews of Modern Physics*, 82, 06 2009.

[5] J.-J. Wen, S. M. Koohpayeh, K. A. Ross, B. A. Trump, T. M. McQueen, K. Kimura, S. Nakatsuji, Y. Qiu, D. M. Pajerowski, J. R. D. Copley, and C. L. Broholm. Disordered Route to the Coulomb Quantum Spin Liquid: Random Transverse Fields on Spin Ice in $Pr_2Zr_2O_7$. *Phys. Rev. Lett.*, 118:107206, Mar 2017.

[6] B. Tomasello, C. Castelnovo, R. Moessner, and J. Quintanilla. Single-ion anisotropy and magnetic field response in the spin-ice materials $Ho_2Ti_2O_7$ and $Dy_2Ti_2O_7$. *Phys. Rev. B*, 92:155120, Oct 2015.

[7] I. Mirebeau, H. Mutka, P. Bonville, A. Apetrei, and A. Forget. Investigation of magnetic fluctuations in $Tb_2Sn_2O_7$ ordered spin ice by high-resolution energy-resolved neutron scattering. *Physical Review B - PHYS REV B*, 78, 11 2008.

[8] H. Silverstein, K. Fritsch, F. Flicker, A. Hallas, J. Gardner, Y. Qiu, G. Ehlers, A. Savici, Z. Yamani, K. Ross, B. Gaulin, M. Gingras, J. Paddison, K. Foyevtsova, R. Valenti, F. Hawthorne, C. Wiebe, and H. Zhou. Liquidlike correlations in single-crystalline $Y_2Mo_2O_7$: An unconventional spin glass. *Physical Review B*, 89, 05 2013.

[9] R. Hänsler and W. Rüdorff. Notizen: $A_2B_2F_7$-Verbindungen mit Pyrochlor- und Weberitstruktur. *Zeitschrift für Naturforschung B*, 25(11):1306–1307, 1970.

[10] J. Krizan and R. Cava. $NaCaCo_2F_7$: A single-crystal high-temperature pyrochlore antiferromagnet. *Physical Review B*, 89, 05 2014.

[11] J Krizan and R Cava. $NaSrCo_2F_7$, a Co^{2+} pyrochlore antiferromagnet. *Journal of physics. Condensed matter : an Institute of Physics journal*, 27:296002, 07 2015.

[12] J. Krizan and R. Cava. $NaCaNi_2F_7$: A frustrated high temperature pyrochlore antiferromagnet with S=1 Ni^{2+}. *Physical Review B - Condensed Matter and Materials Physics*, 92, 04 2015.

[13] M. Sanders, J. Krizan, K. Plumb, T. McQueen, and R. Cava. $NaSrMn_2F_7$, $NaCaFe_2F_7$, and $NaSrFe_2F_7$: novel single crystal pyrochlore antiferromagnets. 08 2016.

[14] B. A. Frandsen, K. A. Ross, J. W. Krizan, G. J. Nilsen, A. R. Wildes, R. J. Cava, R. J. Birgeneau, and S. J. L. Billinge. Real-space investigation of short-range magnetic correlations in fluoride pyrochlores $NaCaCo_2F_7$ and $NaSrCo_2F_7$ with magnetic pair distribution function analysis. *Phys. Rev. Materials*, 1:074412, Dec 2017.

[15] K. W. Plumb, H. J. Changlani, A. Scheie, S. Zhang, J. W. Krizan, J. A. Rodriguez-Rivera, Y. Qiu, B. Winn, R. J. Cava, and C. L. Broholm. Continuum of quantum fluctuations in a three-dimensional S = 1 Heisenberg magnet. *Nature Physics*, 15(1):54–59, oct 2018.

[16] Z. Song and Q. Liu. Tolerance Factor, Phase Stability and Order-Disorder of the Pyrochlore Structure. *Inorganic Chemistry Frontiers*, 7, 02 2020.

[17] T. Ono, K. Morita, M. Yano, H. Tanaka, K. Fujii, H. Uekusa, Y. Narumi, and K. Kindo. Magnetic susceptibilities in a family of $S = \frac{1}{2}$ kagome antiferromagnets. *Phys. Rev. B*, 79:174407, May 2009.

[18] K. Morita, M. Yano, T. Ono, H. Tanaka, K. Fujii, H. Uekusa, Y. Narumi, and K. Kindo. Singlet Ground State and Spin Gap in $S = 1/2$ Kagomé Antiferromagnet $Rb_2Cu_3SnF_{12}$. *Journal of the Physical Society of Japan*, 77(4):043707, 2008.

[19] S. Reisinger, C. Tang, S. Thompson, F. Morrison, and P. Lightfoot. Structural Phase Transition in the S = 1 / 2 Kagome System $Cs_2ZrCu_3F_{12}$ and a Comparison to the Valence-Bond-Solid Phase in $Rb_2SnCu_3F_{12}$. *Chemistry of Materials*, 23:4234–4240, 09 2011.

[20] W. G. Mumme, I. E. Grey, W. D. Birch, A. Pring, C. Bougerol, and N. C. Wilson. Coulsellite, $CaNa_3AlMg_3F_{14}$, a rhombohedral pyrochlore with 1:3 ordering in both A and B sites, from the Cleveland Mine, Tasmania, Australia. *American Mineralogist*, 95(5-6):736–740, May 2010.

[21] R. Schäfer, I. Hagymási, R. Moessner, and D. J. Luitz. Pyrochlore $S = \frac{1}{2}$ Heisenberg antiferromagnet at finite temperature. *Phys. Rev. B*, 102:054408, Aug 2020.

[22] P. Mueller, A. Lohmann, J. Richter, and O. Derzhko. Thermodynamics of the pyrochlore-lattice quantum Heisenberg antiferromagnet. *Physical Review B*, 100(2), July 2019.

[23] S. Pal and S. Lal. Magnetization plateaus of the quantum pyrochlore Heisenberg antiferromagnet. *Phys. Rev. B*, 100:104421, Sep 2019.

[24] A. M. Läuchli, J. Sudan, and R. Moessner. $S = \frac{1}{2}$ kagome Heisenberg antiferromagnet revisited. *Phys. Rev. B*, 100:155142, Oct 2019.

[25] É. du Trémolet de Lacheisserie, D. Gignoux, and M. Schlenker. *Magnetism: Fundamentals*. Number zv. 1. Kluwer Academic, 2002.

[26] K. Buschow and R. Boer. Physics of Magnetism and Magnetic Materials. 7, 01 2003.

[27] S. Blundell. *Magnetism in Condensed Matter*. Oxford master series in condensed matter physics. Oxford University Press, Oxford, 2001.

[28] M. S. Dresselhaus. Magnetic Properties of Solids. *Massachusetts Institute of Technology*, 1999. 6.732 SOLID STATE PHYSICS lecture notes.

[29] D.C. Jiles. *Introduction to Magnetism and Magnetic Materials, Second Edition*. Taylor & Francis, 1998.

[30] N.W. Ashcroft and N.D. Mermin. *Solid State Physics*. HRW international editions. Holt, Rinehart and Winston, 1976.

[31] C. Kittel. *Introduction to Solid State Physics*. Wiley, 2004.

[32] J.A. Mydosh. *Spin Glasses: An Experimental Introduction*. Taylor & Francis, 1993.

[33] P. Fazekas and P. W. Anderson. On the ground state properties of the anisotropic triangular antiferromagnet. *The Philosophical Magazine: A Journal of Theoretical Experimental and Applied Physics*, 30(2):423–440, 1974.

[34] A. R. West. *Solid state chemistry and its applications*. Wiley, Chichester West Sussex ; New York, 1984.

[35] F. Rey-García, R. Ibanez, L. Angurel, F. Costa, and G. de la Fuente. Laser Floating Zone Growth: Overview, Singular Materials, Broad Applications, and Future Perspectives. *Crystals*, 11:38, 12 2020.

[36] J. Ulrich and H.C. Bülau. 7 - Melt crystallization. In Allan S. Myerson, editor, *Handbook of Industrial Crystallization (Second Edition)*, pages 161–179. Butterworth-Heinemann, Woburn, second edition edition, 2002.

[37] W. Höpfner. Handbook of Corrosion Data. 2nd Edition, hrsg. von Bruce D. Craig und David S. Anderson, ASM International Materials Park, OH 44073, Juni 1995, 998 S., $ 188,–, ISBN 0-87170-518-4. In Europa zu beziehen durch: American Technical Publishers Ltd., 27–29 Knowl Piece, Wilbury Way, Hitchin, Herts, SG4 OSX, England. *Materials and Corrosion*, 47(1):53–54, 1996.

[38] A. Kancko. Magnetic shape memory alloys: Effects of doping with Cu and Fe. Bachelor's thesis, Charles University, Prague, 2020.

[39] V. Valvoda, M. Polcarová, and P. Lukáč. *Základy strukturní analỳzy*. Karolinum, 1992.

[40] H. M. Rietveld. A profile refinement method for nuclear and magnetic structures. *Journal of Applied Crystallography*, 2(2):65–71, Jun 1969.

[41] A. A. Coelho. TOPAS and TOPAS-Academic: an optimization program integrating computer algebra and crystallographic objects written in C++. *Journal of Applied Crystallography*, 51(1):210–218, February 2018.

[42] Quantum Design. Magnetic Property Measurement System – MPMS®-XL. `http://www.lao.cz/data/ke-stazeni/Popis%20magnetick%C3%BDch%20vlastnost%C3%AD%20syst%C3%A9mu-d568.pdf`, August 2011.

[43] D. Martien. Introduction to: AC Susceptibility. `https://qdusa.com/siteDocs/appNotes/1078-201.pdf`. Quantum Design.

[44] Quantum Design. Physical Property Measurement System: Heat Capacity Option User's Manual. `https://web.njit.edu/~tyson/PPMS_Documents/PPMS_Manual/1085-150%20Heat%20Capacity.pdf`, January 2004. Part Number 1085-150, H-1.

[45] M.A. Subramanian, G. Aravamudan, and G.V. Subba Rao. Oxide pyrochlores — A review. *Progress in Solid State Chemistry*, 15(2):55–143, 1983.

[46] M. Harris, T. Bramwell, D. McMorrow, T. Zeiske, and K. Godfrey. Geometrical Frustration in the Ferromagnetic Pyrochlore $Ho_2Ti_2O_7$. *Physical Review Letters - PHYS REV LETT*, 79:2554–2557, 09 1997.

[47] A. P. Ramirez, A. Hayashi, R. J. Cava, R. Siddharthan, and B. S. Shastry. Zero-point entropy in 'spin ice'. , 399(6734):333–335, May 1999.

[48] J. Gardner, S. Dunsiger, B. Gaulin, M. Gingras, J. Greedan, R. Kiefl, M. Lumsden, W. MacFarlane, N. Raju, J. Sonier, I. Swainson, and Z. Tun. Cooperative Paramagnetism in the Geometrically Frustrated Pyrochlore Antiferromagnet $Tb_2Ti_2O_7$. *Physical Review Letters*, 82, 02 1999.

[49] N. P. Raju, M. Dion, M. J. P. Gingras, T. E. Mason, and J. E. Greedan. Transition to long-range magnetic order in the highly frustrated insulating pyrochlore antiferromagnet $Gd_2Ti_2O_7$. *Phys. Rev. B*, 59:14489–14498, Jun 1999.

[50] J. Champion, M. Harris, P. Holdsworth, A. Wills, G. Balakrishnan, T. Bramwell, E. Cizmar, T. Fennell, J. Gardner, J. Lago, D. McMorrow, M. Orendac, A. Orendacova, D. Paul, R. Smith, M. Telling, and A. Wildes. $Er_2Ti_2O_7$: Evidence of Order by Disorder in a Frustrated Antiferromagnet. *Physical Review B*, 68, 12 2001.

[51] N. Taira, M. Wakeshima, Y. Hinatsu, A. Tobo, and K. Ohoyama. Magnetic structure of pyrochlore-type $Er_2Ru_2O_7$. *Journal of Solid State Chemistry - J SOLID STATE CHEM*, 176:165–169, 11 2003.

[52] J. Greedan, D. Gout, A. Lozano-Gorrin, S. Derahkshan, T. Proffen, H.-J Kim, E. Bozin, and S. Billinge. Local and average structures of the spin-glass pyrochlore $Y_2Mo_2O_7$ from neutron diffraction and neutron pair distribution function analysis. *Physical Review B - PHYS REV B*, 79, 01 2009.

[53] S. Dunsiger, R. Kiefl, K. H. Chow, B. Gaulin, M. Gingras, J. Greedan, A Keren, K Kojima, G. Luke, W.A. MacFarlane, N. Raju, J. Sonier, Y.J. Uemura, and W. Wu. Muon Spin Relaxation Investigation of the Spin Dynamics of Geometrically Frustrated Antiferromagnets $Y_2Mo_2O_7$ and $Tb_2Mo_2O_7$ Static Critical Behavior of the Spin-Freezing. *Physical review. B, Condensed matter*, 54:9019–9022, 11 1996.

[54] K. Miyoshi, Y. Nishimura, K. Honda, K. Fujiwara, and J. Takeuchi. Successive Spin Freezing Behavior in a Pyrochlore Antiferromagnet $Y_2Mo_2O_7$ under Magnetic Fields. *Journal of the Physical Society of Japan*, 69(11):3517–3520, 2000.

[55] K. Matsuhira, Y Hinatsu, K Tenya, and Sakakibara. Low temperature magnetic properties of frustrated pyrochlore ferromagnets $Ho_2Sn_2O_7$ and $Ho_2Ti_2O_7$. *Journal of Physics: Condensed Matter*, 12:L649, 09 2000.

[56] K. Matsuhira, Y. Hinatsu, K. Tenya, H. Amitsuka, and T. Sakakibara. Low-Temperature Magnetic Properties of Pyrochlore Stannates. *Journal of the Physical Society of Japan*, 71(6):1576–1582, 2002.

[57] H Zhou, C. Wiebe, J. Janik, L. Balicas, J. Wu, Y. Qiu, J Copley, and J. Gardner. Dynamic spin ice: $Pr_2Sn_2O_7$. *Physical review letters*, 101:227204, 12 2008.

[58] J. S. Gardner, G. Ehlers, N. Rosov, R. W. Erwin, and C. Petrovic. Spin-spin correlations in $Yb_2Ti_2O_7$: A polarized neutron scattering study. *Phys. Rev. B*, 70:180404, Nov 2004.

[59] J. Lago, T. Lancaster, S. Blundell, T. Bramwell, F. Pratt, M. Shirai, and C. Baines. Magnetic ordering and dynamics in the XY pyrochlore antiferromagnet: A muon-spin relaxation study of $Er_2Ti_2O_7$ and $Er_2Sn_2O_7$. *J. Phys.: Condens. Matter*, 17, 02 2005.

[60] Y. Machida, S. Nakatsuji, Y. Maeno, T. Tayama, and T. Sakakibara. Geometrical frustration and spin-liquid behavior of the metallic pyrochlore antiferromagnet $Pr_2Ir_2O_7$. *Journal of Magnetism and Magnetic Materials*, 310(2, 2):1328–1330, March 2007. 17th International Conference on Magnetism (ICM 2006), Kyoto, JAPAN, AUG 20-25, 2006.

[61] I. Mirebeau, I. Goncharenko, P. Cadavez-Peres, T. Bramwell, M. Gingras, and J. Gardner. Pressure-induced crystallization of a spin liquid. *Nature*, 420:54–7, 12 2002.

[62] K. A. Ross, L. Savary, B. D. Gaulin, and L. Balents. Quantum Excitations in Quantum Spin Ice. *Phys. Rev. X*, 1:021002, Oct 2011.

[63] K. Arpino, B. Trump, A. Scheie, T. McQueen, and S. Koohpayeh. Impact of Stoichiometry of $Yb_2Ti_2O_7$ on its Physical Properties. 01 2017.

[64] L. Bovo, X Moya, D. Prabhakaran, Y.A. Soh, A. Boothroyd, N.D. Mathur, G. Aeppli, and T. Bramwell. Restoration of the third law in spin ice thin films. *Nature communications*, 5:3439, 03 2014.

[65] J. Stewart, J. Gardner, Y. Qiu, and G. Ehlers. Collective dynamics in the Heisenberg pyrochlore antiferromagnet $Gd_2Sn_2O_7$. *Phys. Rev. B*, 78, 10 2008.

[66] P. Sarte, K. Cruz-Kan, B. Ortiz, K. Hong, M. Bordelon, D. Reig-i Plessis, M. Lee, E. S. Choi, M. Stone, S. Calder, D. Pajerowski, L. Mangin-Thro, Y. Qiu, J. Attfield, S. Wilson, C. Stock, H. Zhou, A. Hallas, J. Paddison, and C. Wiebe. Dynamical ground state in the XY pyrochlore Yb_2GaSbO_7. *npj Quantum Materials*, 6:42, 05 2021.

[67] R. Siddharthan, B. S. Shastry, A. P. Ramirez, A. Hayashi, R. J. Cava, and S. Rosenkranz. Ising Pyrochlore Magnets: Low-Temperature Properties, "Ice Rules," and Beyond. *Phys. Rev. Lett.*, 83:1854–1857, Aug 1999.

[68] D. Reig-i Plessis and A. Hallas. Frustrated Magnetism in Fluoride and Chalcogenide Pyrochlore Lattice Materials. 12 2020.

[69] E. Oliveira, I. Guedes, A. Ayala, J.-Y. Gesland, J. Ellena, R. Moreira, and M. Grimsditch. Crystal structure and vibrational spectrum of the $NaCaMg_2F_7$ pyrochlore. *Journal of Solid State Chemistry*, 177:2943–2950, 08 2004.

[70] E.A Oliveira, I. Guedes, A.P Ayala, J.-Y. Gesland, J. Ellena, R.L Moreira, and M. Grimsditch. Crystal structure and vibrational spectrum of the $NaCaMg_2F_7$ pyrochlore. *Journal of Solid State Chemistry*, 177(8):2943–2950, 2004.

[71] T. E. Saunders and J. T. Chalker. Spin Freezing in Geometrically Frustrated Antiferromagnets with Weak Disorder. *Phys. Rev. Lett.*, 98:157201, Apr 2007.

[72] W. J. L. Buyers, T. M. Holden, E. C. Svensson, R. A. Cowley, and M. T. Hutchings. Excitations in $KCoF_3$. II. Theoretical. *Journal of Physics C: Solid State Physics*, 4(14):2139–2159, oct 1971.

[73] K. Ross, J. Brown, R. Cava, J. Krizan, S. Nagler, J. R. Rivera, and M. Stone. Single-Ion Properties of the $S_{eff} = 1/2$ XY Antiferromagnetic Pyrochlores $NaA'Co_2F_7$ ($A' = Ca^{2+}$, Sr^{2+}). (95), 2017-04-13 00:04:00 2017.

[74] J. Zeisner, S. A. Bräuninger, L. Opherden, R. Sarkar, D. I. Gorbunov, J. W. Krizan, T. Herrmannsdörfer, R. J. Cava, J. Wosnitza, B. Büchner, H.-H. Klauss, and V. Kataev. Magnetic interactions and spin dynamics in the bond-disordered pyrochlore fluoride $NaCaCo_2F_7$. *Phys. Rev. B*, 99:155104, Apr 2019.

[75] T. Watanabe, H. Kato, Y. Hara, J. Krizan, and R. Cava. Softening of breathing elastic mode and trigonal elastic mode in the disordered pyrochlore magnet $NaCaCo_2F_7$. *Physical Review B*, 101, 06 2020.

[76] F. Momma, K.and Izumi. VESTA: A Three-Dimensional Visualization System for Electronic and Structural Analysis. *Journal of Applied Crystallography - J APPL CRYST*, 41:653–658, 06 2008.

[77] M. B. Sanders, J. W. Krizan, and R. J. Cava. $RE_3Sb_3Zn_2O_{14}$ (RE = La, Pr, Nd, Sm, Eu, Gd): a new family of pyrochlore derivatives with rare earth ions on a 2D Kagome lattice. *J. Mater. Chem. C*, 4:541–550, 2016.

[78] C. Lee. Magnetic property studies of the rhombohedral pyrochlore $Re_3Sb_3Mn_2O_14$ (Re = La, Lu and Y). Master's thesis, Seoul: Chung-Ang University Graduate School, 2019.

[79] K. Li, Y. Hu, Y. Wang, T. Kamiyama, B. Wang, Z. Li, and J. Lin. Syntheses and properties of a family of new compounds $RE_3Sb_3Co_2O_{14}$ (RE = La, Pr, Nd, Sm–Ho) with an ordered pyrochlore structure. *Journal of Solid State Chemistry*, 217:80–86, 2014.

[80] L. Downie, E. Ardashnikova, C. Tang, A. Vasiliev, P. Berdonosov, V. Dolgikh, M. Vries, and P. Lightfoot. Novel $S = 1/2$ kagome lattice materials: $Cs_2TiCu_3F_{12}$ and $Rb_2TiCu_3F_{12}$. *Crystals*, 5:226, 05 2015.

[81] T. Ono, K. Morita, M. Yano, H. Tanaka, K. Fujii, H. Uekusa, Y. Narumi, and K. Kindo. New S=1/2 Kagomé antiferromagnets $A_2Cu_3SnF_{12}$: A = Cs and Rb. *Journal of Physics: Conference Series*, 145, 2009.

[82] R. D. Shannon. Revised effective ionic radii and systematic studies of interatomic distances in halides and chalcogenides. *Acta Crystallographica Section A*, 32(5):751–767, Sep 1976.

[83] L. H. Ahrens. The use of ionization potentials Part 1. Ionic radii of the elements. *Geochimica et Cosmochimica Acta*, 2(3):155–169, 1952.

[84] V. Sidey. Predicting the lattice parameters for the $A^IA^{II}B_2^{II}F_7$ disordered cubic fluoride pyrochlores. *Zeitschrift für Kristallographie - Crystalline Materials*, 232(10):729–731, 2017.

[85] B. C. Chakoumakos. Systematics of the pyrochlore structure type, ideal $A_2B_2X_6Y$. *Journal of Solid State Chemistry*, 53(1):120–129, 1984.

[86] K. Friese, A. Grzechnik, W. Morgenroth, G. Buth, S. Doyle, and J.Y. Gesland. Synchrotron study of pyrochlore-related $NaCdZn_2F_7$. *Acta Crystallographica Section E*, 61, 08 2005.

[87] A. Grzechnik, R. Kaindl, and K. Friese. Temperature dependent study of the crystal structure of $NaCdZn_2F_7$ pyrochlore. *Journal of Physics and Chemistry of Solids - J PHYS CHEM SOLIDS*, 68:382–388, 03 2007.

[88] A. Grzechnik, J. M. Posse, W. Morgenroth, and K. Friese. Compressibilities of disordered fluoride pyrochlores NaCdZn $_2$F $_7$ and NaCaMg $_2$F $_7$. *Journal of Solid State Chemistry France*, 180(7):1998–2003, July 2007.

[89] T Wallin and J Zeising. On the structure and electrical-conductivity of the fluoperovskite $NaZnF_3$. *Solid State Ionics*, 39(3-4):273–276, JUL 1990.

[90] B. Toby. R Factors in Rietveld Analysis: How Good is Good Enough? *Powder Diffraction*, 21:67–70, 03 2006.

[91] K. Ross, J. Krizan, R. Rodriguez Rivera, J.and Cava, and C. Broholm. Static and dynamic XY-like short-range order in a frustrated magnet with exchange disorder. *Physical Review B*, 93, 01 2016.

[92] J.W. Stout and S.A. Reed. The crystal structure of MnF_2, FeF_2, CoF_2, NiF_2 Aand ZnF_2. *Journal of the American Chemical Society*, 76(21):5279–5281, 1954.

[93] B. Lütgert and D. Babel. Kristallstrukturverfeinerungen an Natriumtrifluorometallaten $NaMF_3$ (M = Mg, Co, Ni, Zn): Oktaederkippung und Toleranzfaktor orthorhombischer Fluorperowskite. *Zeitschrift für anorganische und allgemeine Chemie*, 616:133–140, 1992.

[94] V. I. Korepanov and D. M. Sedlovets. An asymmetric fitting function for condensed-phase Raman spectroscopy. *Analyst*, 143:2674–2679, 2018.

[95] E. Seifert. Origin Pro 9.1: Scientific Data Analysis and Graphing Software-Software Review. *Journal of chemical information and modeling*, 54, 04 2014.

[96] R. Janes and E. Moore. *Metal-ligand Bonding*. The Royal Society of Chemistry, 2004.

[97] P. Gredin, A. de Kozak, J. Chassaing, and M. Quarton. The binary system CuF_2-CdF_2. Structural, spectroscopic and magnetic studies on $CdCuF_4$. *European Journal of Solid State Inorganic Chemistry*, 30:789–800, 1993.

[98] J. B. Forsyth, P. J. Brown, and B. M. Wanklyn. Magnetism in cupric oxide. *Journal of Physics C: Solid State Physics*, 21(15):2917–2929, may 1988.

[99] Y. Cai, M. N. Wilson, A. M. Hallas, L. Liu, B. A. Frandsen, S. R. Dunsiger, J. W. Krizan, R. J. Cava, O. Rubel, Y. J. Uemura, and G. M. Luke. μSR study of spin freezing and persistent spin dynamics in $NaCaNi_2F_7$. *Journal of Physics-Condensed Matter*, 30(38), SEP 26 2018.

[100] S. Zhang, H. J. Changlani, K. W. Plumb, O. Tchernyshyov, and R. Moessner. Dynamical Structure Factor of the Three-Dimensional Quantum Spin Liquid Candidate $NaCaNi_2F_7$. *Physical Review Letters*, 122(16), April 2019.

[101] M. Hidaka and M. Ono. The Crystal Structure of $NaNiF_3$. *Journal of the Physical Society of Japan*, 43(1):258–263, 1977.

[102] F. Hawthorne. Refinement of the crystal structure of cryolite. *The Canadian Mineralogist*, 13:377–382, 01 1975.

[103] A. Boireau, P. Gravereau, J.M. Dance, A. Tressaud, P. Hagenmuller, J.L. Soubeyroux, M. Welsch, and D. Babel. Structural and magnetic properties of several cobalt(ii) weberites. *Materials Research Bulletin*, 28(1):27–38, 1993.

[104] H.M. Haendler and W.J. Bernard. The Reaction of Fluorine with Cadmium and Some of its Binary Compounds. The Crystal Structure, Density and Melting Point of Cadmium Fluoride. *Journal of the American Chemical Society*, 73:5218–5219, 1951.

[105] A. Lari Lavassani, G. Jourdan, C. Avinens, and L. Cot. Etude cristallographique d'hexafluorostannates cubiques et hexagonaux $M_2^{1+}SnF_6$. Comptes Rendus des Seances de l'Academie des Sciences, Serie C: Sciences Chimiques, 1974.

[106] R.E. Schmidt, M. Welsch, S. Kummer-Doerner, and D. Babel. Einkristalluntersuchungen an hexagonalen Fluorperowskiten AMF_3 (M^{II} = Mg, Mn, Fe, Co, Ni). *Zeitschrift fuer Anorganische und Allgemeine Chemie (1950) (DE)*, 625:637–642, 1999.

[107] T. Suto, T. Ono, H. Tanaka, and H. Uekusa. Structural and Magnetic Properties of $S = 1/2$ Kagomé Antiferromagnet $Cs_2Cu_3ZrF_{12}$. *Progress of Theoretical Physics Supplement - PROG THEOR PHYS SUPPL*, 159:67–71, 05 2005.

[108] H. Bode and G. Teufer. Über Strukturen von Hexafluorozirkonaten und Hexafluorohafnaten. *Zeitschrift für anorganische und allgemeine Chemie*, 283(1-6):18–25, 1956.

List of Figures

List of Tables

List of Symbols and Abbreviations

$\boldsymbol{r}$	Position vector
$\boldsymbol{p}$	Linear momentum
m_e	Electron mass
γ	Gyromagnetic ratio
$\hbar$	Reduced Planck's constant
τ	Torque
ω_L	Larmor frequency
∇	Del (nabla) operator
$\boldsymbol{S}, \boldsymbol{L}, \boldsymbol{J}$	Spin, orbital and total angular momentum
$\hat{\boldsymbol{S}}, \hat{\boldsymbol{L}}, \hat{\boldsymbol{J}}$	Spin, orbital and total angular momentum operators
$\hat{\boldsymbol{\sigma}}$, $\hat{\sigma_x}$, $\hat{\sigma_y}$, $\hat{\sigma_z}$	Pauli vector, Pauli matrices
μ	Dipolar magnetic moment
μ_{eff}	Effective magnetic moment
μ_{sat}	Saturated magnetic moment
μ_S, μ_L, μ_J	Spin, orbital and total-angular-momentum magnetic moment
μ_B	Bohr magneton
μ_0, μ_r	Vacuum permeability, relative permeability
n, l, m_l, m_s	Principal, azimuthal, magnetic and spin quantum number
S, L, J	Spin, orbital and total angular momentum quantum numbers
g_S, g_J	Electron spin g-factor, Landé g-factor
$\hat{\mathscr{H}}$	Hamiltonian
$\boldsymbol{M}, M_s$	Magnetization, saturation magnetization
$\boldsymbol{m}$	Net magnetic moment
$\boldsymbol{B}$	Magnetic field (magnetic induction)
$\boldsymbol{H}$	Magnetic field (magnetic field strength)
$\chi, \chi^{\text{mol}}, \chi_g$	Magnetic susceptibility, molar and mass susceptibility

V_m	Molar volume
M_m	Molar mass
ρ	Density
U	Potential energy, internal energy
V	Potential energy
E, E_a	Energy, activation energy
$\hat{\boldsymbol{A}}(\boldsymbol{r})$	Vector potential
Z	Atomic number, or number of formula units per unit cell
T	Temperature
S, S_{mag}, S_0	Entropy, magnetic and residual entropy
F	Helmholtz free energy
p	Pressure
k_B	Boltzmann constant
$B_J(x)$	Brillouin function
$f.u.$	Formula unit
N, N_A	Number of particles, Avogadro's number
ψ	Wavefunction
$J, \tilde{\mathrm{J}}$	Exchange integral
$\boldsymbol{D}$	Dzyaloshinsky-Moriya vector
$RKKY$	Ruderman-Kittel-Kasuya-Yosida interaction
λ	Weiss molecular field constant
C, C^{mol}	Curie constant, molar Curie constant
T_C, T_N, T_f	Curie / critical, Néel and spin-freezing temperature
θ_{CW}	Curie-Weiss temperature
n	Number density
f	Frustration index
λ	Wavelength
hkl	Miller indices
$\boldsymbol{q}$	Scattering (diffraction) vector

$\boldsymbol{s}, \boldsymbol{s_0}$	Unit wavevectors
$\boldsymbol{G}_{hkl}$	Reciprocal lattice vector
$a, b, c, \alpha, \beta, \gamma$	Lattice parameters
d_{hkl}	Interplanar distance
ω, ν	Angular frequency, frequency
χ', χ''	Real and imaginary part of AC susceptibility
ϕ	Phase shift
τ_0	Intrinsic relaxation time
T_0	Ideal freezing temperature
$C_p, C_V, C_{\mathrm{mag}}$	Constant-pressure-, constant-volume-, magnetic heat capacity
Q	Heat
W	work
γ	Sommerfeld coefficient
τ	Pyrochlore structure tolerance factor
x, y, z	Atomic coordinates
R_A, R_B	Ionic radii of A- and B-site
J_{eff}	Effective spin-state
QSL	Quantum spin liquid
RVB	Resonating valence bond
PXRD, SCXRD	Powder and Single Crystal X-ray Diffraction
ZFC, FC	Zero-field-cooled, field-cooled
DC, AC	Direct current, alternating current
RSO	Reciprocating sample option
SQUID	Superconducting quantum interference device
VSM	Vibrating sample magnetometer
MPMS	Magnetic property measurement system
PPMS	Physical property measurement system
BCS	Bardeen-Cooper-Schrieffer theory
ACMS	AC magnetic susceptibility
VSM	Vibrating sample magnetometer
S.G.	Space group

A. Attachments

A.1 Effective magnetic moments of $4f$ and $3d$ compounds

Table 1 Effective magneton numbers p for trivalent lanthanide group ions

(Near room temperature)				
Ion	Configuration	Basic level	p(calc) = $g[J(J+1)]^{1/2}$	p(exp), approximate
Ce^{3+}	$4f^1 5s^2 p^6$	$^2F_{5/2}$	2.54	2.4
Pr^{3+}	$4f^2 5s^2 p^6$	$^3H_4$	3.58	3.5
Nd^{3+}	$4f^3 5s^2 p^6$	$^4I_{9/2}$	3.62	3.5
Pm^{3+}	$4f^4 5s^2 p^6$	$^5I_4$	2.68	—
Sm^{3+}	$4f^5 5s^2 p^6$	$^6H_{5/2}$	0.84	1.5
Eu^{3+}	$4f^6 5s^2 p^6$	$^7F_0$	0	3.4
Gd^{3+}	$4f^7 5s^2 p^6$	$^8S_{7/2}$	7.94	8.0
Tb^{3+}	$4f^8 5s^2 p^6$	$^7F_6$	9.72	9.5
Dy^{3+}	$4f^9 5s^2 p^6$	$^6H_{15/2}$	10.63	10.6
Ho^{3+}	$4f^{10} 5s^2 p^6$	$^5I_8$	10.60	10.4
Er^{3+}	$4f^{11} 5s^2 p^6$	$^4I_{15/2}$	9.59	9.5
Tm^{3+}	$4f^{12} 5s^2 p^6$	$^3H_6$	7.57	7.3
Yb^{3+}	$4f^{13} 5s^2 p^6$	$^2F_{7/2}$	4.54	4.5

Figure A.1: Groundstate configurations and effective magnetic moments for isolated trivalent rare-earth $4f$ ions. Taken from [31].

Table 2 Effective magneton numbers for iron group ions

Ion	Configuration	Basic level	p(calc) = $g[J(J+1)]^{1/2}$	p(calc) = $2[S(S+1)]^{1/2}$	p(exp)[a]
Ti^{3+}, V^{4+}	$3d^1$	$^2D_{3/2}$	1.55	1.73	1.8
V^{3+}	$3d^2$	$^3F_2$	1.63	2.83	2.8
Cr^{3+}, V^{2+}	$3d^3$	$^4F_{3/2}$	0.77	3.87	3.8
Mn^{3+}, Cr^{2+}	$3d^4$	$^5D_0$	0	4.90	4.9
Fe^{3+}, Mn^{2+}	$3d^5$	$^6S_{5/2}$	5.92	5.92	5.9
Fe^{2+}	$3d^6$	$^5D_4$	6.70	4.90	5.4
Co^{2+}	$3d^7$	$^4F_{9/2}$	6.63	3.87	4.8
Ni^{2+}	$3d^8$	$^3F_4$	5.59	2.83	3.2
Cu^{2+}	$3d^9$	$^2D_{5/2}$	3.55	1.73	1.9

[a] Representative values.

Figure A.2: Groundstate configurations and effective magnetic moments for isolated divalent $3d$ transition metal ions. Taken from [31].

A.2 TOPAS Academic v6 input file

jEdit - AKF041_NaCdMn2F7_1st-regrind.inp

```
1
2  '--------------------------------------------------------------
3  'Input File for simple Rietveld Refinement
4  'Use save/set current button then run with F6 in topas
5  'Replace $ and # symbols with text/numbers as needed
6  '--------------------------------------------------------------
7
8  r_wp  14.7646178 r_exp  24.3272442 r_p  9.92047016 r_wp_dash  30.7006524
   r_p_dash  29.1809424 r_exp_dash  50.5845987 weighted_Durbin_Watson  0.812752565
   gof  0.606916991
9
10 '--------------------------------------------------------------
11 'General information about refinement here
12 'Remove comments as required
13 '--------------------------------------------------------------
14
15 iters 100000
16 chi2_convergence_criteria 0.001
17 do_errors
18
19 '--------------------------------------------------------------
20 'Information on datafile etc here
21 'Check that default weighting is appropriate for your data
22 '--------------------------------------------------------------
23 xdd AKF041_NaCdMn2F7_1st-regrind.dat fullprof_format
24   x_calculation_step = Yobs_dx_at(Xo); convolution_step 4
25   bkg @  11.7731932`_0.0370029806  9.97165908`_0.0621615518
     0.234588805`_0.0526884943  2.36395838`_0.0481605366 -0.033216296`_0.0440101486
     -0.0476667957`_0.0386302411
26
27   LP_Factor(!th2_monochromator, 0)
28   CuKa2(0.0001)
29   Variable_Divergence_Intensity
30   Zero_Error(@, 0.09001`_0.00128)
31
32 str
33   space_group Fd-3m:2
34    phase_name "NaCdMn2F7"
35     scale @  4.9648005e-006`_5.166e-008
36     TCHZ_Peak_Type(pku, 0.00284`_0.00162,pkv,   -0.00748`_0.00242,
       pkw,0.00432`_0.00126, pkz, 0.00001`_0.00078,pky, 0.10375`_0.00468,pkx,
       0.03482`_0.00241)
37     Simple_Axial_Model(axial, 6.78595`_0.33091)
38     Phase_Density_g_on_cm3( 4.29361`_0.00015)
39
40     Cubic( NaCdMn2F7_lattice  10.538615`_0.000126)
41
42    site Cd_1   x =1/2;   y =1/2;   z =1/2;                        occ Cd
      !occ_Cd_1_040148412 0.5   beq beq_Cd_1_040148412  3.40522`_0.48190
43    site Na_1   x =1/2;   y =1/2;   z =1/2;                        occ Na
      !occ_Na_1_040148412 0.5   beq beq_Na_1_040148412  0.58719`_1.36065
44    site Mn_1   x =0;   y =0;   z =0;                          occ Mn
      !occ_Mn_1_040148412 1.0   beq beq_Mn_1_040148412 0.09948`_0.05133
45    site F_1    x =3/8;   y =3/8;   z =3/8;                       occ F
      !occ_F_1_040148412 1.0     beq beq_F_1_040148412  13.49056`_0.98562
46    site F_2    x x_F_2_040148412  0.36506`_0.00055   y =1/8;   z =1/8;  occ F
      !occ_F_2_040148412 1.0     beq beq_F_2_040148412  4.16845`_0.12409
```

26/04/22 23:14 :: page 1

```
                    jEdit - AKF041_NaCdMn2F7_1st-regrind.inp
47    MVW( 3026.126, 1170.344`_0.042, 100.000`_0.000)
48
49    C_matrix_normalized
50 {
51                              1   2   3   4   5   6   7   8   9  10  11  12  13
                                14  15  16  17  18  19  20  21  22
52 bkg24115520             1:  100  79  56  43  29  16   3   4   3   3  -7  36   0
   5  10   4  -5  -2   7 -17   8   1
53 bkg24115776             2:   79 100  75  48  38  25   1   2   7   1  -5  35   4
   2   9   6  -7   1   5 -20  15  -1
54 bkg24116288             3:   56  75 100  65  47  33  -1   0   4  -3   2  15   5
  -4   4   4  -5   2   2  -8   9  -2
55 bkg24117312             4:   43  48  65 100  62  40   2   1  -2  -1   2  -4  -4
   1   6   2  -1  -1   2   3  -5   2
56 bkg24113728             5:   29  38  47  62 100  50  -1   0   5   4  -3  -2  -3
  -2   8   4  -3   1   1  -5   5  -1
57 bkg24116544             6:   16  25  33  40  50 100  -1  -1   3   2  -1  -3   0
  -10   3   4  -4   3  -1  -1   2  -1
58 m62681175_26            7:    3   1  -1   2  -1  -1 100  83  -2   1  -1   3  -3
  11   3  26 -34  37 -12   5  -7  88
59 NaCdMn2F7_lattice       8:    4   2   0   1   0  -1  83 100  -1   1  -2   5  -2
   8   3  18 -23  26  -8  -3  -1  60
60 scale23130208_          9:    3   7   4  -2   5   3  -2  -1 100  80 -73  49  -6
  -19  38   3  -4   3  -0 -12  13  -4
61 beq_Cd_1_040148412     10:    3   1  -3  -1   4   2   1   1  80 100 -98  48 -13
  -18  33   0   1  -0  -1   1  -2  -0
62 beq_Na_1_040148412     11:   -7  -5   2   2  -3  -1  -1  -2 -73 -98 100 -58  10
  16 -30  -0  -1   0   2  -2   3  -1
63 beq_Mn_1_040148412     12:   36  35  15  -4  -2  -3   3   5  49  48 -58 100   9
  -4  17   5  -6   1   4 -20  15   0
64 beq_F_1_040148412      13:    0   4   5  -4  -3   0  -3  -2  -6 -13  10   9 100
  -11 -32  -1   1  -0  -0  -1   3  -4
65 x_F_2_040148412        14:    5   2  -4   1  -2 -10  11   8 -19 -18  16  -4 -11
  100  19  -2   1  -0   1  -3   2  11
66 beq_F_2_040148412      15:   10   9   4   6   8   3   3   3  38  33 -30  17 -32
  19 100   4  -5  -1   5 -10   6   3
67 pku                    16:    4   6   4   2   4   4  26  18   3   0  -0   5  -1
  -2   4 100 -87  75 -33 -23  25  31
68 pkv                    17:   -5  -7  -5  -1  -3  -4 -34 -23  -4   1  -1  -6   1
   1  -5 -87 100 -67   1  33 -35 -41
69 pkw                    18:   -2   1   2  -1   1   3  37  26   3  -0   0   1  -0
  -0  -1  75 -67 100 -71  -8  26  44
70 pkz                    19:    7   5   2   2   1  -1 -12  -8  -0  -1   2   4  -0
   1   5 -33   1 -71 100 -26   9 -13
71 pky                    20:  -17 -20  -8   3  -5  -1   5  -3 -12   1  -2 -20  -1
  -3 -10 -23  33  -8 -26 100 -90  10
72 pkx                    21:    8  15   9  -5   5   2  -7  -1  13  -2   3  15   3
   2   6  25 -35  26   9 -90 100 -10
73 axial                  22:    1  -1  -2   2  -1  -1  88  60  -4  -0  -1   0  -4
  11   3  31 -41  44 -13  10 -10 100
74 }

                              26/04/22 23:14 :: page 2
```

Figure A.3: A typical TOPAS Academic v6 [41] input file used in our PXRD refinements ($NaCdMn_2F_7$ refinement file shown in the picture).